Magnon spectroscopy by neutrons and electrons for THz spintronic applications

Julio Cesar Alves do Nascimento

Doctor of Philosophy

University of York

School of Physics, Engineering and Technology

March 2024

Abstract

We present a comprehensive study into the inelastic spectra obtained by electrons interacting with magnetic materials. The main focus is on the charge-dependent interaction of the electron beam, in an electron microscope, via the local vector potential generated by the magnetic lattice in terms of the spin-scattering function. This methodology allows direct comparison between charge-dependent and purely spin-dependent interactions. Our results for the double differential cross-section show strong scattering vector dependence (q^{-2}) and linear dependence with the electron probe's momentum. Additionally, we explore the intensity dependence on the relative orientation between the electron probe wavevector and the local magnetic moments of the solid, using YIG as a case study due to its importance as a platform material for magnonics.

In this work, we also introduce a methodology for calculating the spin-scattering function, particularly in confined geometries such as thin films, for both collinear and non-collinear spin-structures materials. Through case studies involving bcc Fe(100), YIG(100), NiO(100) and NiO(111), we illustrate the effects of film thickness and crystal orientation on magnon modes in three different magnetic systems, ferromagnetic, ferrimagnetic and antiferromagnetic, respectively. The quasi-momentum quantisation results in granularity in the inelastic spectra in the reciprocal space path, reflecting thin film orientation. This approach captures softer modes arising from the partial interaction of magnetic moments near the surface in thin film geometry, concurrently with the bulk modes. Furthermore, we explore the influence of magneto-crystalline anisotropy, demonstrating its effect by increasing the overall hardness of magnon modes. Specifically, introducing surface anisotropy leads to a shift of surface-related magnon density of states (DOS) peaks to higher energies, that could result in surface-confined modes. Finally, we performed calculations for the phase and group velocity of the magnons in these structures, further elucidating their behaviour in confined geometries.

Dedicated to my family

Contents

List of Tables

List of Figures

Acknowledgements

Formal acknowledgements

I would like to thank my supervisors, Prof. Vlado Lazarov, Dr. Phil Hasnip and Dr. Aires Ferreira, for their support and guidance during the time I have spent working on this project. The insight, guidance and time you have offered has been invaluable. I would like to also thank the many members of the academic and administrative body of the University of York who have been of great help during my Ph.D.

Informal acknowledgements

Personal growth is seldom achieved in isolation, and in the past years, mine has been a collective effort, owned mostly by the patience of my supervisors and the opportunity offered to me by Prof. Vlado Lazarov. My colleagues have also been invaluable in my progress both by sharing their knowledge with me, and occasionally some light conversations over a pint. For this, I would like to thank, Dr Genadi Naydenov, Dr Adam Kerrigan, Dr Robert Lawrence, Mr Ahmad Altumali and Dr Connor Murrill. Outside of the department, I consider myself very fortunate to have a family that supports and cares for me and is on board with enduring the distance. I have not taken for granted all the sacrifices you have made to get me here. Finally, I'd like to thank my partner and best friend Calisa, the only reason why I kept my sanity during these years, sometimes at the cost of her own sanity. If you can find one person you really like, you're lucky. And if that person can also stand you, you're really lucky. If you find someone you can talk to while you eat apples on a bright fall morning, is almost too greedy, that's how lucky I feel for having you in my life.

Declaration

I declare that the work presented in this thesis is based on research carried out in the Department of Physics, University of York, England. No part of this thesis has been submitted elsewhere for any other degree or qualification and it is all my own work unless the contrary is stated in the text. All sources are acknowledged as References.

Publications

1. Julio A. do Nascimento, Adam Kerrigan, S. A. Cavill, Phil J. Hasnip, Demie Kepaptsoglou, Quentin M. Ramasse, Vlado K. Lazarov, Confined magnon dispersion in ferromagnetic and antiferromagnetic thin films in a second quantization approach: the case of Fe and NiO. arXiv:2312.07715 [cond-mat.mtrl-sci] (2024) (Available at https://arxiv.org/abs/2312.07715)

2. Julio A. do Nascimento, Phil J. Hasnip, S. A. Cavill, Fabrizio Cossu, Demie Kepaptsoglou, Quentin M. Ramasse, Adam Kerrigan, Vlado K. Lazarov, Theory of momentum-resolved magnon electron energy loss spectra: The case of Yttrium Iron Garnet arXiv:2401.12302 [cond-mat.mtrl-sci] (2024) (Available at https://arxiv.org/abs/2401.12302)

Chapter 1

Introduction

1.1 Motivation

The relentless growth of data has become a defining characteristic of the digital era. Demand for efficient and scalable data processing and storage solutions continue to escalate, driven by emerging technologies such as the Internet of Things, artificial intelligence, and big data analytics.

The total amount of data created, captured, copied, and consumed globally is forecast to increase rapidly, reaching 64.2 zettabytes in 2020 a growth higher than previously expected caused by the increased demand due to the COVID-19 pandemic, as more people worked and learned from home and used home entertainment options more often. The projection for the next years up to 2025 is for the global data creation to grow to more than 180 zettabytes [1]. In line with the strong growth of the data volume, the installed base of storage capacity of 6.7 zettabytes in 2020 [2] is forecast to increase, growing at a compound annual growth rate of 19.2 per cent over the forecast period from 2020 to 2025.

Beyond the data requirements, the energy consumption of the storage and processing of this data has also seen substantial growth over the last few years. The International Energy Agency (IEA) published a report on achieving net zero emissions by 2050 [3], highlighting the significant growth in energy consumption related to the storage and processing of data. The global data centre electricity consumption ranged from 240 to 340 terawatt-hours (TWh) in 2022, equivalent to approximately 1-1.3% of the final global electricity demand. This figure does not include energy used for cryptocurrency mining, which con-

sumed an estimated 110 TWh in 2022, amounting to around 0.4% of annual global electricity demand. Additionally, data transmission networks consumed between 260 and 360 TWh in 2022, constituting 1-1.5% of global electricity use.

Despite improvements in IT hardware efficiency, cooling systems, and a transition towards more efficient cloud and hyperscale data centres, the energy consumption of data centres has continued to increase significantly over the past few years. The IEA report indicates that annual growth rates within this sector have varied between 20% and 40%, emphasising the ongoing necessity for concerted efforts to improve energy efficiency.

To address these challenges number of solutions have been proposed. Algorithmic solutions focus on changing data processing paradigms with more efficient programming models such as MapReduce [4], Apache Hadoop [5], and Apache Spark [6]. While architectural solutions focus on changing the availability of resources in a centralised way, such is the case of cloud-based computing, which, according to Microsoft Corporation and WSP Global Inc., is 93% more energy-efficient than on-premises data centres [7].

On the other hand, one can focus on the improvement of IT hardware efficiency, by improving the current complementary metal-oxide semiconductor (CMOS) technology [8] and particularly exploring new data processing, and storage paradigms, beyond electron charge as a carrier of information. Alternative technologies include spintronics [9], magnonics [10] and topological electronics [11], whereby the electron's spin is utilised in addition or as a substitution for its charge.

Magnetic devices have been readily available for decades, mostly owing to the interplay between charge currents and magnetisation orientation in heterostructured materials, as in hard disk drives (HDD) [12, 13], magnetic sensors [14–16] or, in the more recent commercially competitive nonvolatile memory applications, in the form of magnetic random-access memory (MRAM) [17–20].

Alternatively, pure spin current devices also offer non-volatility, faster data processing, and potentially even lower power consumption [21–23]. Hence, the study of the collective dynamics of magnetic systems has attracted a great

deal of attention, due to the promise of using the electron spin to deliver an energetically efficient way to meet the data processing requirements of modern society. This has led to a body of knowledge in a field generally known as magnonics, which encompasses the production, transmission, storage and processing of information using spin waves [10, 24]. Spin waves are dynamic eigen-excitations of magnetically ordered materials, often described in terms of their quanta, i.e. 'magnons', much like photons or phonons are the quanta of light and lattice waves, respectively.

The concept of spin waves has been introduced by F. Bloch in 1932 [25], following the proposal of exchange interaction as an explanation for ferromagnetic ordering by W. Heisenberg (1928) and Ya. G. Dorfman and Ya. I. Frenkel (1928) [26]. Spin waves were introduced as a solution for the excited states of a ferromagnetic system. This approach resulted in two predictions: in a first-order approximation, the spontaneous magnetisation of an isotropic cubic ferromagnet, decreases with a $T^{3/2}$ temperature dependence and, in the absence of anisotropy, there should not be long-range order magnetisation in dimensions lower than three. The same framework was later developed in a second quantized manner by Holstein and Primakoff [27] and Dyson [28], and in parallel in a more phenomenological macroscopic approach, by Landau and Lifshitz [26], laying the foundation of spin wave theory.

Although not a complete theory to explain fully the dynamics of magnetic systems when studying phase transitions, for example [29], spin wave theory has shown to be a useful paradigm for thinking of new technological applications [9].

One of the goals is to substitute the charge current-based information encoding with all spin wave alternatives. To achieve this goal, some approaches follow a path to provide transistor-like functionality [30, 31], while others aim at replacing the entirety of the logical gate device [32, 33], instead of the individual transistors.

A hybrid spin-wave–CMOS system integrated data processing with a CMOS periphery is a more realistic approach in the short term, provided that the signal conversion between magnonic and electric parts of the device can be effi-

cient [10].

Moreover, the development and refinement of magnonic devices critically hinges on the meticulous consideration of particular geometries [34–36], with a notable emphasis on reduced dimensionality. Within this framework, a pressing need arises to broaden existing computational techniques, conventionally employed in the investigation of magnons in bulk materials, to incorporate the effects stemming from confined geometries inherent to thin films and heterostructures [37,38].

As a result, investigations of magnetism in low dimensions serve a dual purpose. First, it offers valuable insights into how the magnetic properties of a solid evolve when transitioning from a three-dimensional (3D) bulk crystal to two-, one-, or zero-dimensional structures, which often leads to the emergence of unique phenomena not observed in bulk magnets. Second, from a technological standpoint, the incorporation of magnetic materials into modern technologies necessitates their presence in these confined geometries. [39–43].

1.2 Methods to characterise magnon spectra

To systematically investigate the generation, manipulation, and identification of magnons, there is a need to improve the methodologies for both exciting and probing these phenomena.

One of the most direct ways of probing the magnon's energies, and to characterise them, is via inelastic experiments. Among the many options available, using light, via Raman experiments [44], Thz absorption [45] and resonant inelastic x-ray scattering (RIXS) [46], neutrons, via inelastic neutron scattering (INS) [47] experiments and electrons using electron energy loss spectroscopy (EELS). Each of such options has its advantages and disadvantages.

Multiple parameters will be crucial when choosing the probing experiment that will provide the most cost-effective results when studying the dynamics of magnetic materials. In THz spectroscopy, a photon with THz frequency is absorbed and a spin-wave is created or vice versa. The wavelength of the photon of THz frequencies is of the order of $10^6 \mathring{A}$ resulting in a momentum extremely

small compared to the size of the Brillouin zone (of the order of $1\mathring{A}^{-1}$), hence the momentum transfer is small, allowing only the excitation of spin waves at the Γ point. In this regard, with photon wavelengths from 0.4 to 1 μm (from the ultraviolet to the infrared), Raman spectroscopy also detects spin waves with momentum close to zero. In contrast RIXS, which uses very short wavelength photons, e.g. 1.3 nm at the energy 931 eV of the Cu L_3 peak [48], is comparable to the size of the Brillouin zone [49], with the drawback of requiring large cyclotron facilities to achieve such high energies. One inherent disadvantage of optical methods is the lack of spatial resolution due to the diffraction limit of photons (several microns), incapable of unveiling the sub-nanoscale spatial distribution [50], for example, for Raman experiments, using a 405 nm laser and an objective with a numerical aperture (NA) of 0.9 the theoretical spatial resolution achievable is 275 nm. However, it should be stressed that this is a theoretical ideal and is rarely achieved in practice due to sample-dependent scattering properties. A practical Raman spatial resolution is on the order of 1 μm [51–55].

Inelastic neutron scattering (INS) precedes the inelastic x-ray scattering (IXS) historically [56–58], in this case, neutrons rather than photons are scattered by spin-waves. Such techniques have been largely used for phonon spectroscopy in crystalline solids and to study magnetic structures via neutron diffraction, for over half a century. However, their application is limited by the scarcity and expense of INS and IXS spectrometers, which must be based on reactor, accelerator, or synchrotron sources. Another requirement for such experiments is the growth of single-crystal specimens, particularly in the case of neutrons where crystal sizes of 20–1000 mm^3 are needed, due to low interaction cross-section, also demanding a long acquisition time because of the low flux of particles. The spatial resolution of INS is larger than 1cm, precluding spatially resolved studies, hence limited only to bulk specimens. [59].

Over the past decade, meV-level Scanning Transmission Electron Microscopy-Electron Energy Loss spectroscopy (STEM-EELS) has made significant strides, achieving atomic-level contrast [60], detecting spectral signatures of individual impurity atoms [61], and conducting spatial- and angle-resolved measure-

ments on defects in crystalline materials [62]. This progress paves the way for the investigation of magnons with high spatial resolution.

The method's potential expansion into studying magnons is anticipated due to the overlapping energy range that magnetic modes share with vibrational modes in solid-state materials. Despite the weaker interaction of magnetic moments with the electron beam, compared to the Coulomb potential, by up to 3 or 4 orders of magnitude, which makes their detection challenging [63,64]. Recent advancements in hybrid-pixel detectors have led to significant improvements in dynamic range and reduced background noise, enabling the detection of signals as low as 10^{-7} of the full beam intensity [65]. Furthermore, enhancements in monochromator and spectrometer design have resulted in increased energy resolutions, particularly at lower acceleration voltages, achieving resolutions of 4.2 meV at 30 kV [66]. These technological advancements have substantially enhanced sensitivity and signal detection capabilities, thereby facilitating the exploration of magnon excitations in STEM experimental settings.

Theoretical approaches for evaluating the EEL spectra have been developed focusing on spin-polarised probes interacting via an exchange-like interaction with the magnetic solid's local spins [67], emphasising only the spin-spin interaction. However, in addition to spin-spin interaction, when evaluating EELS one also has to take into account the charge-based interactions, between the electron beam and the magnetic moments of the material. In light of this additional interaction, it is essential to understand what additional effects EELS can reveal using unpolarised e-beams. While the spin-spin interaction of electron and neutron probes are equivalent, we expect that the vector potential, originated by the magnons in the system, will affect the electron probe's canonical momentum [68]. This leads to different dependencies with respect to the scattering vector and electron probe momentum, revealing an additional signature of electron-magnon inelastic scattering.

1.3 Overview of Thesis

This thesis is organised as follows; in chapter 2 we give an introduction to magnetism, to help us to introduce the different interactions present in a magnetic system in the form of the Heisenberg Hamiltonian. In particular, we demonstrate the derivation given by Bloch [25] to show that spin waves are the natural spin-excitation modes of magnetically ordered systems. Next, we define the general bosonic transformation, with a focus on the Holstein-Primakoff transformation, followed by the Bogoliubov diagonalisation to obtain the spin-wave spectrum. We also discuss the 'Kübler trick' which allows the treatment of non-colinear spin structures.

In chapter 3, we extend this approach and provide a generalised method for calculating the effect of confinement in thin films using the Holstein-Primakoff-transformed Heisenberg Hamiltonian, for systems with known ground states. Previous computational work on confined magnons has focused on utilising atomistic spin dynamics [69], or on solving the linearised equation of motion that derives from the Heisenberg Hamiltonian *via* a so-called confined ansatz [70, 71]. Using the latter approach, a study of magnon confinement effects in low-dimensional magnetic structures was recently reported [72]. Furthermore, in this work, authors utilised the Holstein-Primakoff transformation [27] and the Bogoliubov transformation [73] to rewrite the spin scattering function in confined geometries, with calculations performed for a model 1D spin chain. We further develop this approach assuming tensorial exchange and anisotropy terms allowing the study of realistic thin films for collinear and non-collinear magnetic structures.

This approach allows the application of second quantisation to thin films with arbitrary spin order, including ferromagnets, ferrimagnets and antiferromagnets with given ground states. This opens a pathway for calculations that support the broad range of methods utilising different probes to study magnons in technologically relevant thin film systems. We demonstrate this methodology for the prototypical systems of ferromagnetic films of bcc Fe(100), Yttrium iron garnet (YIG)(100) and antiferromagnetic NiO with (100) and

(111) crystallographic orientations with varying thicknesses.

Next, in chapter 4, we explore the effects of the non-spin-polarised beam in the meV-level STEM-EELS apparatus, using YIG as a prototype material. We derive and compare the effects of the spin-based interaction and the charge-based interaction, and their momentum dependence, by calculating the inelastic scattering intensity in the form of the double differential cross-section.

Finally, in Chapter 5, we conclude with our final remarks and perspectives on the present work.

After the document, willing readers will discover appendices containing detailed information and derivations related to the results discussed in the main text. Although understanding the main text does not require reviewing the appendices, those seeking a deeper understanding will find valuable information within them.

Chapter 2

Fundamentals of Quantum Magnetism

2.1 Atomic magnetic moments

Magnetism in condensed matter cannot be properly explained by classical physics. Before the advent of quantum mechanics, the observation of macroscopic magnetic fields was attempted to be explained by the existence of elementary Amperian current loops flowing within the material. Indeed, the concept may apply to an induction coil or an electromagnet, but it is hard to justify classically this persistent flow of current in an insulator. [74]

This picture was overthrown with the proposition of an important theorem. The Bohr-Van Leuween's theorem, states that the equilibrium magnetisation is zero, i.e. no charge currents flow spontaneously under conditions of thermodynamic equilibrium. This result led to an alternative approach to persistent magnetism relying on the electron's quantized orbital motions [75] and the electron's intrinsic angular momentum, originally proposed by Goudsmit and Uhlenbeck [76], and later deduced by Dirac [77] on the basis of quantisation of the relativistic momentum [78]. We will now discuss both these quantities and how they relate to the atomic magnetic moment.

First, recall that in the spherically symmetric potential of the atomic nuclear charge, there are four atomic quantum numbers, three arising from the dimensionality of space, and one, the spin quantum number, arising from relativistic effects. We have the principal quantum number $n = 1, 2...$, forming a shell,

the orbital angular momentum $l \leq n-1$, each forming a subshell, which is commonly labelled by $s, p, d, f...$, where s labels the $l = 0$ subshell, and the subsequent letters the higher angular momenta, and the magnetic quantum number, forming an orbital, which represents the projection of the orbital angular momentum on the z-direction, $m_l = -l, ..., +l$ and the spin quantum number $m_s = \pm 1/2$.

Magnetic moments, arising from both spin and orbital angular momenta, present a challenge in their quantum mechanical treatment, particularly with multiple electrons. To navigate this complexity, we adopt the $L-S$ coupling scheme, also known as the Russell-Saunders coupling scheme. This procedure uses the expected value of the z-component of the angular momentum, given by $\langle L_z \rangle = \hbar m_l$ and the z-component of the spin angular momentum, given by $\langle S_z \rangle = \hbar m_s$, and combines the individual electrons in the system to yield a collective spin, denoted as $S = \sum_i S_i$, and similarly, orbital angular momenta combine to form a total orbital angular momentum, $L = \sum_i L_i$. The overall angular momentum of the atom is then expressed as $J = L + S$. This approach simplifies the description of the atom's states, utilizing combined quantum numbers L, m_L, S, and m_S, each obtained as the sum of corresponding values for individual electrons.

Having defined the available orbitals in an atom, we need now to understand how the electrons get arranged in these different orbitals. Relying on spectroscopic data, a set of basic rules where devised by Friedrich Hund, known as Hund's rules. These rules, fundamentally, encapsulate energy minimization in the arrangement of electrons in the central potential of the atom, and taking into account the Pauli's exclusion principle, where no two or more indistinguishable particles possessing half-integer spins (fermions) can occupy the same state, i.e., have the same set of quantum numbers, and the spin-orbit interaction, empirically predicting how the electrons will arrange themselves in higher atomic number atoms.

- First rule: Place the electrons in the open subshells, such that the total spin quantum number is maximized.

- Second rule: When electrons are added to degenerate orbitals (orbitals of the same energy), the energy is minimised by occupying different orbitals with parallel spins before pairing up, such that the orbital angular momentum is maximised.

- Third rule: The determination of the total angular momentum, J, is established by the following rules: $J = |L - S|$ when the electronic shell is less than half full and $J = |L + S|$ when the shell is more than half full. This constraint is motivated by an effort to minimise the spin-orbit energy.

This set of rules, allows us to predict the ground state angular momentum of isolated atoms.

With these definitions for the atomic angular momentum, we are ready to connect the angular momentum to the magnetic moment. To further our discussion, let's define the magnetic moment in terms of a current density $\mathbf{j}_m$, set to represent the motion of electrons in their stationary orbits within the atoms [78].

From this definition, we can write the magnetic moment resultant from the motion of these electrons,

$$\mathbf{m}_i = \frac{1}{2}\int d^3\mathbf{r}(\mathbf{r} - \mathbf{R}_i) \times \mathbf{j}_m^{(i)} \tag{2.1}$$

which represents the magnetic moment of the i'th atom. By writing the current density for an atom in position $\mathbf{R}_i$, as a function of p atomic electrons labelled by j with velocity $\mathbf{v}_j$, at position $\mathbf{r}_j$ and charge e, in the following way,

$$\mathbf{j}_m^{(i)} = -e\sum_{j=1}^{p} \mathbf{v}_j \delta(\mathbf{r} - \mathbf{R}_i - \mathbf{r}_j) \tag{2.2}$$

then substituting 2.2 in 2.1 we get,

$$\mathbf{m}_i = -\frac{e}{2}\sum_{j=1}^{p} \mathbf{r}_j \times \mathbf{v}_j = -\frac{e}{2m}\sum_{j=1}^{p} \mathbf{l}_j \tag{2.3}$$

where $\mathbf{l}_j$ is the angular momentum of the j'th electron given by $\mathbf{l}_j = \mathbf{r}_j \times (m\mathbf{v}_j)$. Noting the quantisation of angular momentum, we have that $|\mathbf{l}_j| =$

$\sqrt{l_j(l_j+1)}\hbar$, where l_j is the jth electron orbital quantum number that is quantized and restricted to integer values $l_j = 0, 1, 2, ...n-1$. This allows us to write the relationship between magnetic moment and orbital angular momentum, given by,

$$\mathbf{m}_i = \mathbf{m}_L = -\frac{\mu_B}{\hbar}\hat{\mathbf{L}} \tag{2.4}$$

where we used the relationship between the angular momentum operator $\hat{\mathbf{L}}$ and its expectation value $\langle\hat{\mathbf{L}}\rangle = l\hbar$, and defined the Bohr magneton in SI units $\mu_B = e\hbar/2m$, which represents a fundamental unit of magnetic moment, m is the electron mass and $\hbar$ is the reduced Planck constant.

So far we have only defined the magnetic moment associated with the orbital angular momentum, in reality, electrons carry an intrinsic angular momentum. Its existence can't be explained with non-relativistic quantum mechanics, it can only be predicted by the Dirac equation representation of quantum mechanics, which predicts a quantum number for the electrons with an operator that behaves in the same way as the orbital angular momentum. The algebra that represents this behaviour will be defined later in section 2.2.2.

One can show that the magnetic moment associated with the total spin $\mathbf{S}$ of the atomic electrons,

$$\mathbf{m}_S = -\frac{\mu_B}{\hbar}g_e\hat{\mathbf{S}} \tag{2.5}$$

where g_e is a constant without explanation in non-relativistic physics, it is called Landè's g-factor, which is given by,

$$g_e = 2(1 + \frac{\alpha}{2\pi} + \mathcal{O}(\alpha^2)) \approx 2.0023 \tag{2.6}$$

with $\alpha = 1/137$ which is Sommerfeld's fine structure constant. A usual approximation that will be sufficient for our purposes is to take $g_e \approx 2$.

Taking all this into account, we can write the total magnetic moment as,

$$\mathbf{m} = -\frac{\mu_B}{\hbar}(\hat{\mathbf{L}} + 2\hat{\mathbf{S}}) \tag{2.7}$$

One important point to note is that in all cases where we are dealing with angular momentum, a factor of $\hbar$ follows, for this reason, it is conventional to use atomic units to simplify the notation, where we define the angular momentum to be measured in units of $\hbar$, allowing us to rewrite Eq. (2.7),

$$\mathbf{m} = -\mu_B(\hat{\mathbf{L}} + 2\hat{\mathbf{S}}) \tag{2.8}$$

For the remainder of chapter 2 we will use the SI notation in agreement with Eq. (2.7).

Now we have defined the building blocks of magnetism, but have given no reason as to why certain materials are magnetic and others aren't. First, we need to define the quantum mechanical origin of the atomic angular momentum in atoms.

2.2 Magnetic moments in solids

So far we discussed the existence of magnetic moments in atoms without discussing their quantum mechanical origin. In this section, we will define their origin and how these characteristics are affected when the atoms are arranged in solids [74,78,79].

In the previous section, we described isolated atoms, but for material science applications, we will be interested in the characteristics of such atoms once they are grouped in a solid. In some cases, the isolated atoms' characteristics are carried to the crystalline structure of a solid, as is the case in crystals containing rare earth atoms [80]. However, in the majority of cases, the magnetic ions will be affected by the interactions with the surrounding ions in the solid, leading to distinct properties.

One of such interactions is known as the crystal field, which is the electric field derived from the neighbouring atoms in the crystal. The intensity of this interaction depends on the symmetry of the local environment. To gain a mental picture of how these interactions affect the orbitals' energies it is important to point out the spatial distribution of the electron density of the atomic orbitals.

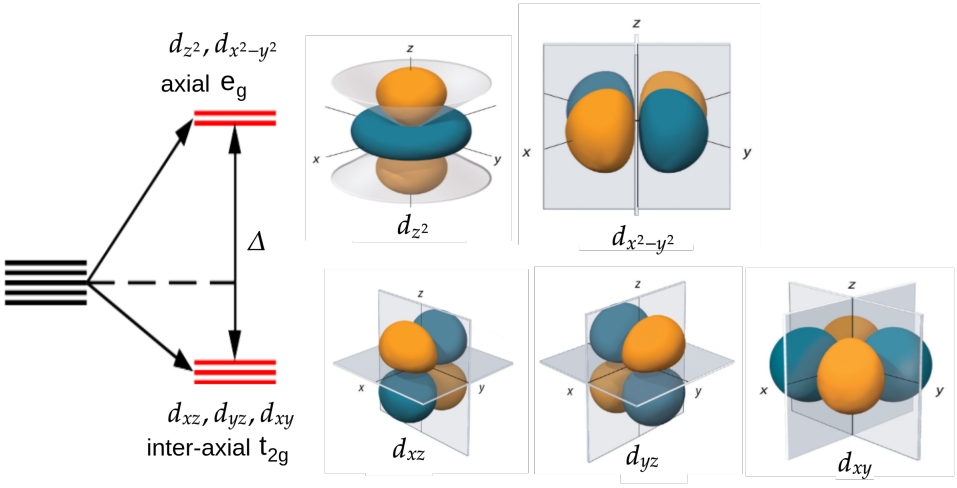

Figure 2.1: Diagramatic representation of the d-orbitals and how they group by symmetry in axial and inter-axial. The parameter Δ represents the energy difference due to the crystal field-dependent degeneracy lift for an octahedral bonding environment.

Among the possible orbitals, only the s orbitals are spherically symmetric, all others have some angular dependence. The relationship between the symmetry of the crystalline environment and orbital symmetry determines how orbital degeneracy is affected by crystal fields. Crystal fields cause a reduction in the rotational symmetry of the system, leading to the lifting of orbital degeneracy.

To exemplify this concept we point to figure 2.1, notice that, symmetry-wise the d orbitals can be separated into two types: the t_{2g} orbitals which point between the Cartesian axis and the e_g orbitals which point along the axis. This difference leads to a split in energy between the t_{2g} and the e_g orbitals.

In this altered environment, Hund's Rules don't minimise the energy of the atom anymore, giving rise to different total magnetic moments. When dealing with transition metal ions with an incomplete set of 3d electrons, the filling sequence involves populating the lowest levels (in this case, the t_{2g} levels) before moving to the higher energy e_g levels. However, the specific orbital filling order is specific to the interplay between crystal field energy and the Coulomb energy cost associated with placing two electrons in the same orbital, a phenomenon known as pairing energy, typically having a positive value. In the scenario where the crystal field energy is lower than the pairing energy (re-

ferred to as the weak-field case), electrons are added to the system in a manner where each orbital is singly occupied before any orbital becomes doubly occupied. Conversely, in the strong-field case where the crystal field energy surpasses the pairing energy, electrons preferentially occupy the lower energy orbitals before filling the energetically higher orbitals.

2.2.1 Orbital quenching

When describing the total angular momentum of 3d ions one finds discrepancies in the expected value from Hund's Laws and the experimental values [79]. This disparity arises due to the pronounced dominance of the crystal field interaction over the spin-orbit interaction in the context of 3d ions. Consequently, Hund's third rule, which was rooted in the assumption that the spin-orbit interaction holds notable significance, making it the second-largest interaction in the electron's energy following the Coulombic effects, is, in fact, erroneous in this scenario.

In reality, the system finds itself in a ground state such that $L = 0$, this way the total angular momentum $J = S$ and $g_e = 2$ meaning that the atomic magnetic moment is pure spin, this has implications in the quantum mechanical treatment of magnetic materials that will come into play later.

This effect is known as orbital quenching. This effect is largest in 3d ions where the spin-orbit interaction can be ignored compared to the crystal fields. This definition becomes less clean-cut for 4d and 5d orbitals since for heavier atoms, the spin-orbit interaction becomes comparable to the crystal fields.

2.2.2 Spin operators

For our purposes, it is important to study how we will define the notation that will represent the spins in the system. Particularly, we need to define a set of operators that the algebra represents the experimental behaviour of the angular momentum, in particular the spin.

The experimental behaviour of the electron's spin follows an algebra that is encapsulated in the spin operators $\hat{\mathbf{S}} = (\hat{S}_x, \hat{S}_y, \hat{S}_z)$. By convention we note that

the angular momentum is measured in units of $\hbar$, so the angular momentum associated with the spin can acquire values of $m_S = \pm 1/2$, which previously we associated with the z-direction projection of the spin angular momentum. The spin operators are associated mathematically as a measurement of the spin projection in a particular direction, i.e. $\hat{S}_z$ represents a measurement of the z-direction projection of the spin of the particle. We can then define a basis for our spin system, such that the $\hat{S}_z$ operator is diagonal, allowing us to write:

$$\hat{S}_z|\uparrow\rangle = \frac{\hbar}{2}|\uparrow\rangle, \qquad \hat{S}_z|\downarrow\rangle = -\frac{\hbar}{2}|\downarrow\rangle \tag{2.9}$$

or in a more general way:

$$\hat{S}_z|S, m_s\rangle = \hbar m_s|S, m_s\rangle \tag{2.10}$$

here the state is defined by $|S, m_s\rangle$, where $\hbar^2\sqrt{S(S+1)}$ is the magnitude of the angular momentum and m_s the z-direction projection.

One restriction posed by experiments for the spin's algebra comes from the Stern-Gerlach experiment that shows that successive measurements of the spin of a particle don't commute. Hence, this non-commutation needs to be reflected in the algebra of the spin operators and is mathematically represented by:

$$[\hat{S}_\alpha, \hat{S}_\beta] = i\hbar\varepsilon_{\alpha\beta\gamma}\hat{S}_\gamma \tag{2.11}$$

where α, β and γ are the Cartesian coordinates x, y, z, and $\varepsilon_{\alpha\beta\gamma}$ is the Levi-Civita antisymmetric permutation tensor. All coordinate operators commute with the $\hat{\mathbf{S}}^2$ so that,

$$[\hat{S}^2, \hat{S}_\alpha] = 0 \tag{2.12}$$

thus it is possible to measure simultaneously the magnitude of the spin angular momentum and one of its components. In our algebra, the measurement of the magnitude of the angular momentum will be defined by:

$$\hat{S}^2|S, m_s\rangle = \hbar^2\lambda|S, m_s\rangle \tag{2.13}$$

where λ is a constant to be determined. To proceed we will define two new operators $\hat{S}_+ = \hat{S}_x + i\hat{S}_y$ and $\hat{S}_- = \hat{S}_x - i\hat{S}_y$, known as raising and lowering operators for reasons that will become clear once we define their eigenvalues in the basis defined in Eq. (2.10). Their commutation relations can be defined using the relations given in Eq. (2.11) and Eq. (2.12):

$$[\hat{S}_z, \hat{S}_+] = \hbar\hat{S}_+ \tag{2.14}$$

$$[\hat{S}_z, \hat{S}_-] = -\hbar\hat{S}_- \tag{2.15}$$

$$[\hat{S}_+, \hat{S}_-] = 2\hbar\hat{S}_z \tag{2.16}$$

$$[\hat{S}^2, \hat{S}_+] = [\hat{S}^2, \hat{S}_-] = 0 \tag{2.17}$$

To define the eigenvalues of these operators we will multiply both sides of Eq. (2.14) through the right, with the basis defined in Eq. (2.10). Given this, we can write:

$$(\hat{S}_z\hat{S}_+ - \hat{S}_+\hat{S}_z)|S, m_s\rangle = \hbar\hat{S}_+|S, m_s\rangle \tag{2.18}$$

using the relation Eq. (2.10) we have:

$$\begin{aligned}
\hat{S}_z\hat{S}_+|S, m_s\rangle - \hat{S}_+\hat{S}_z|S, m_s\rangle &= \hbar\hat{S}_+|S, m_s\rangle \\
\hat{S}_z(\hat{S}_+|S, m_s\rangle) - \hbar m_s(\hat{S}_+|S, m_s\rangle) &= \hbar(\hat{S}_+|S, m_s\rangle) \\
\hat{S}_z(\hat{S}_+|S, m_s\rangle) &= (\hbar m_s + \hbar)(\hat{S}_+|S, m_s\rangle) \\
\hat{S}_z(\hat{S}_+|S, m_s\rangle) &= \hbar(m_s + 1)(\hat{S}_+|S, m_s\rangle)
\end{aligned} \tag{2.19}$$

Thus, $\hat{S}_+|S, m_s\rangle$ is an eigenstate of the S_z, with eigenvalue $\hbar(m_s + 1)$. In the same way $\hat{S}_-|S, m_s\rangle$ has eigenvalue $\hbar(m_s - 1)$. These properties name the operators "raising" and "lowering" operators, respectively. Using the definitions for $\hat{S}_+$, $\hat{S}_-$ and the commutator in Eq. (2.16) allows us to write:

$$\begin{aligned}\hat{S}^2 =& \hat{S}_x^2 + \hat{S}_y^2 + \hat{S}_z^2 \\ =& \frac{1}{2}(S_+S_- + S_-S_+) + \hat{S}_z^2 \\ =& S_-S_+ + \hat{S}_z(\hat{S}_z + \hbar)\end{aligned} \tag{2.20}$$

with this new definition for $\hat{\mathbf{S}}^2$, we can find the value for $\lambda = S(S+1)$, given that we have the eigenvalues of S_+ and S_-, which are given by [74],

$$\hat{S}^+|S, m_s\rangle = \hbar\sqrt{(S - m_s)(S + m_s + 1)}|S, m_s\rangle \tag{2.21}$$

$$\hat{S}^-|S, m_s\rangle = \hbar\sqrt{(S + m_s)(S - m_s + 1)}|S, m_s\rangle \tag{2.22}$$

giving us:

$$\hat{S}^2|S, m_s\rangle = \hbar^2 S(S+1)|S, m_s\rangle \tag{2.23}$$

These definitions are general to both the angular momenta due to spin and orbit.

2.3 Magnetic interactions

Now that we have set the generators of magnetism in solids, the atomic magnetic moments, we turn our attention to the fact that in nature solids exhibit magnetic order, meaning that these individuals' magnetic moments tend to align with each other. The different ways that this can happen will be discussed later. The reason for this tendency has to be attributed to interactions between the magnetic moments. In this section, we will describe different forms of interaction between the magnetic moments and where they come from.

2.3.1 Dipolar interaction

Historically the first presumed interaction that could cause the magnetic order in the solids that exhibit net magnetisation was the dipolar interaction, given by,

$$E = -\frac{\mu_0}{4\pi r^3}\left[\boldsymbol{\mu}_1 \cdot \boldsymbol{\mu}_2 - \frac{3}{r^2}(\boldsymbol{\mu}_1 \cdot \boldsymbol{r})(\boldsymbol{\mu}_2 \cdot \mathbf{r})\right] \tag{2.24}$$

which describes the energy of the interaction of two magnetic moments $\boldsymbol{\mu}_1$ and $\boldsymbol{\mu}_2$ separated by a distance r. Notice that the energy is minimised if the two magnetic moments point in the same direction, meaning that, for a set of magnetic moments in a solid, this interaction shows promise in explaining the net magnetisation of solids. The problem arises when one calculates the thermodynamics of a system of magnetic moments interacting purely via dipolar interaction. Such a system can only exhibit stable ferromagnetism for temperatures below $\approx 4K$ as seen in the appendix A, this is contradictory to the existence of magnetically ordered materials at room temperature.

2.3.2 Magnetocrystalline anisotropy

In the atomic theory proposed by Dirac, relativistic effects are taken into account. The introduction of such effects leads to a, previously unaccounted-for, interaction known as spin-orbit coupling. In this interaction, the orbital and spin angular moments couple giving rise to such an effect where the orbital angular momentum drags the spin. In crystals the spatial isotropy is broken, meaning that the spherically asymmetric orbitals tend to align with the high-symmetry axis of the crystal. Consequently, the spin-orbit coupling makes the system energy to also depend on the absolute orientation of the magnetic moments of the system. This phenomenon is called Magnetocrystaline anisotropy, and is a uniaxial anisotropy in the system that can be modelled in the spin Hamiltonian in the following way,

$$H_K = -K\sum_i (\hat{m} \cdot \hat{\mathbf{S}}_i)^2 \tag{2.25}$$

where $\hat{m}$ is a unit vector that identifies the preferred direction that defines the anisotropy, so-called easy-axis, K is the anisotropy parameter that is the energy difference between the magnetic moments pointing along $\hat{m}$ and perpendicular to it, and $\hat{\mathbf{S}}_i = (\hat{S}_{ix}, \hat{S}_{iy}, \hat{S}_{iz})$ is the spin operator vector referent to site i . In the case where $K > 0$ the energy is minimised when the magnetic moments are

parallel to $\hat{m}$, however if the $K < 0$ the energy is minimal when the magnetic moments are aligned in any direction perpendicular to $\hat{m}$. In this case, we say that the system has an easy-plane [74,79].

2.3.3 Exchange interaction

The exchange interaction is central to the modern theory of magnetism. This quantum mechanical phenomenon, was found to account for the alignment of magnetic moments in materials. To demonstrate its origins we will follow the derivation given in [78]. At the core of the exchange interaction is the fundamental difference between classical and quantum mechanics, which concerns the concept of indistinguishability of identical particles. This concept leads to the interpretation that, if two particles have the same quantum numbers they are indistinguishable, hence if two particles in an N-particle system with wavefunction $\psi(\mathbf{r}_1, \ldots, \mathbf{r}_j, \ldots, \mathbf{r}_r, \ldots, \mathbf{r}_N)$ are interchanged the physical result should be the same. The mathematical implication for this is that after a coordinate permutation of two particles in the N-particle system, the new state needs to differ from the original state by a prefactor λ. This way if the same two coordinates are interchanged a second time, we end up with exactly the same state function,

$$\begin{aligned}\psi(\mathbf{r}_1, \ldots, \mathbf{r}_j, \ldots, \mathbf{r}_r, \ldots, \mathbf{r}_N) =& \lambda\psi(\mathbf{r}_1, \ldots, \mathbf{r}_r, \ldots, \mathbf{r}_j, \ldots, \mathbf{r}_N) \\ =& \lambda^2\psi(\mathbf{r}_1, \ldots, \mathbf{r}_j, \ldots, \mathbf{r}_r, \ldots, \mathbf{r}_N)\end{aligned} \tag{2.26}$$

leading us to conclude that $\lambda^2 = 1$, or $\lambda = \pm 1$. For the solution which $\lambda = 1$ describes a class of particles called Bosons, while the $\lambda = -1$ Fermions. The source of our magnetic moments in our discussion are the electrons which are Fermions, hence the wave function of our system needs to be antisymmetric.

Beyond the spatial asymmetry in the wave function, since the electrons carry the intrinsic magnetic moment in the form of spin, we also need to care for the symmetry of the spin part of the wave function. Given that electrons are spin-$\frac{1}{2}$ particles, we need to write our total wave function as a product of the spatial

$|\psi\rangle$ and spin $|S, m_s\rangle$ parts

To gain insight into the origins of this interaction, let's examine a simplified model involving just two electrons with spatial coordinates $\mathbf{r}_1$ and $\mathbf{r}_2$. Because electrons must obey an overall anti-symmetric wave function, we need to consider the symmetry of both the spatial and spin parts. We can write,

$$|\psi\rangle^{\pm} = \frac{1}{\sqrt{2}}(\psi_a(\mathbf{r}_1)\psi_a(\mathbf{r}_2) \pm \psi_a(\mathbf{r}_2)\psi_a(\mathbf{r}_1)) \tag{2.27}$$

where we defined $|\psi\rangle^{+}$ as a symmetric and $|\psi\rangle^{-}$ a anti-symmetric spatial wave function for our toy model. For the spin part, we have,

$$|0,0\rangle^{-} = \frac{1}{\sqrt{2}}(|\uparrow\downarrow\rangle - |\downarrow\uparrow\rangle) \tag{2.28}$$

for the anti-symmetric singlet state of the spin part, and,

$$|1,1\rangle^{+} = |\uparrow\uparrow\rangle \tag{2.29}$$

$$|1,0\rangle^{+} = \frac{1}{\sqrt{2}}(|\uparrow\downarrow\rangle + |\downarrow\uparrow\rangle) \tag{2.30}$$

$$|1,-1\rangle^{+} = |\downarrow\downarrow\rangle \tag{2.31}$$

which is the triplet symmetric state of the spin part. Here we have simplified the notation to write $|S, m_s\rangle = |1/2, 1/2\rangle = |\uparrow\rangle$ and $|S, m_s\rangle = |1/2, -1/2\rangle = |\downarrow\rangle$.

Our main goal is to get a term in the Hamiltonian of the system that represents the increase change in the total energy due to the interaction of spins of the two particles. From our current discussion, we have four possible anti-symmetrical possibilities for the wavefunction of our system, one singlet state $|\psi_s\rangle$ and three triplet states $|\psi_t\rangle$ represented by,

$$\begin{aligned} |\psi_s\rangle &= |\psi\rangle^{+}|0,0\rangle^{-} \\ |\psi_t\rangle &= |\psi\rangle^{-}|1,m\rangle^{+} \quad , m = 0, 1, -1 \end{aligned} \tag{2.32}$$

Let's then take a general Hamiltonian H that accounts for the interaction between two particles. For the four possible anti-symmetric wave functions,

we have two distinct energies: one associated with the singlet state (E^+) and the other with the triplet state(E^-),

$$\begin{aligned} H|\psi_s\rangle &= E^+|\psi_s\rangle \\ H|\psi_t\rangle &= E^-|\psi_t\rangle \quad , m = 0, 1, -1 \end{aligned} \tag{2.33}$$

Note that if $E^+ \neq E^-$ this leads to a ground state with a clear spin ordering which means that there exists a spontaneous magnetic order. To identify the functional form of such Hamiltonian, let $\mathbf{S}_i$ be the spin operator of the i'th electron we have the expectation value for the square of each spin operator given by,

$$\mathbf{S}_i^2 = \hbar^2 S(S+1) = \hbar^2 \frac{1}{2}(\frac{1}{2}+1) = \hbar^2 \frac{3}{4} \tag{2.34}$$

for $i = 1, 2$, while for the total spin of the system, accounting for both spins, given by,

$$\mathbf{S}_{tot}^2 = (\mathbf{S}_1 + \mathbf{S}_2)^2 = \mathbf{S}_1^2 + \mathbf{S}_2^2 + 2\mathbf{S}_1 \cdot \mathbf{S}_2 = \frac{3}{2}\hbar^2 + 2\mathbf{S}_1 \cdot \mathbf{S}_2 \tag{2.35}$$

where we used the result from Eq. (2.34). Rearranging Eq. (2.35) and using the result from Eq. (2.23) for $\mathbf{S}_{tot}^2$ we have,

$$\frac{1}{\hbar^2}\mathbf{S}_1 \cdot \mathbf{S}_2 = \frac{1}{2}S(S+1) - \frac{3}{4} \tag{2.36}$$

Note that the total spin of the singlet state is $S = 0$ while for the triplet state we have $S = 1$, hence we have two possible values, such that,

$$\begin{cases} \left(\frac{1}{\hbar^2}\mathbf{S}_1 \cdot \mathbf{S}_2\right)_{singlet} &= -\frac{3}{4} \\ \left(\frac{1}{\hbar^2}\mathbf{S}_1 \cdot \mathbf{S}_2\right)_{triplet} &= \frac{1}{4} \end{cases} \tag{2.37}$$

with this in mind, we can write the following equation that agrees with the definition put forth in Eq. (2.33),

$$\hat{H} = \frac{1}{4}(E^+ + 3E^-) - (E^+ - E^-)\frac{1}{\hbar^2}\mathbf{S}_1 \cdot \mathbf{S}_2 \tag{2.38}$$

such that its application of it to the singlet and triplet states, and accounting for

Eq. (2.37) gives us,

$$\begin{aligned}\hat{H}|\psi_s\rangle =& \frac{1}{4}(E^+ + 3E^-) + (E^+ - E^-)\frac{3}{4}|\psi\rangle^+|0,0\rangle^- \quad = E^+|\psi_s\rangle \\ \hat{H}|\psi_t\rangle =& \frac{1}{4}(E^+ + 3E^-) - (E^+ - E^-)\frac{1}{4}|\psi\rangle^-|1,m\rangle^+ \quad = E^-|\psi_t\rangle, m = 0,1,-1\end{aligned} \tag{2.39}$$

this definition of $\hat{H}$ is named the molecular Heisenberg model since we limit the interaction to only a pair of spins.

$$\tilde{H} = J_0 - J_{12}\mathbf{S}_1 \cdot \mathbf{S}_2 \tag{2.40}$$

with,

$$J_{12} = \frac{1}{\hbar^2}(E_+ - E_-) \tag{2.41}$$

notice that this approach doesn't give a direct way to calculate the interaction coupling constant but suggests that the solution comes from deriving the energy difference between the singlet and triplet states in the proposed molecular arrangement, assuming that this difference exists, which can be shown to be the case by using the Heitler-London method.

From this derivation, we are able to postulate an extension in the case of the N-particle system. This extension is the known Heisenberg model, given by:

$$H = -\frac{1}{2}\sum_{ij} J_{ij}\mathbf{S}_i \cdot \mathbf{S}_j \tag{2.42}$$

with this definition for $J_{ij} > 0$ the spins will tend to align with each other, while for $J_{ij} < 0$ the spins will tend to anti-align, notice that we introduced a half-factor to avoid double counting.

In some books [78] the J_{ij} is derived from the orbitals wavefunctions overlap between neighbouring magnetic atoms via the Heitler-London method which introduces a factor of two, which is, in our case, integrated into the J_{ij} parameter.

Noticing the vectorial nature of the spin operators, $\mathbf{S}$, leads to a generalisation of the exchange parameter to a tensorial form, allowing us to write,

$$H = -\frac{1}{2}\sum_{ij} \mathbf{S}_i \cdot J_{ij} \cdot \mathbf{S}_j \tag{2.43}$$

in this notation, the exchange parameter is written as an exchange matrix such that:

$$J_{ij} = \begin{pmatrix} J_{ij}^{xx} & J_{ij}^{xy} & J_{ij}^{xz} \\ J_{ij}^{yx} & J_{ij}^{yy} & J_{ij}^{yz} \\ J_{ij}^{zx} & J_{ij}^{zy} & J_{ij}^{zz} \end{pmatrix} \tag{2.44}$$

In this form, we can discuss further forms of interactions in the magnetic solid. Beyond the magnetocrystalline anisotropy, we can also have anisotropy connected fundamentally to the exchange interaction leading to the orientation of the individual magnetic moments to be anisotropic, meaning that on top of aligning with each other the magnetic moments will align collectively with a preferred crystallografic direction. In this case, the anisotropy comes from having different exchange parameters in each direction of the system, such that, in the matrix exchange parameter, we have different values for J_{ij}^{xx},$J_{ij}^{yy}$and J_{ij}^{zz}.

The off-diagonal terms in the exchange matrix Eq. (2.44) give rise to anti-symmetric exchange, also known as Dzyaloshinskii–Moriya interaction (DMI) [81,82]. The antisymmetry comes from the requirement that symmetric terms in the off-diagonal entries of the exchange matrix have opposing signs. Fundamentally, the DMI is a result of the spin-orbit coupling interaction. It is a pair interaction in which the energy is minimised when the magnetic moments point perpendicular to each other. We can write the effect of the off-diagonal terms of the exchange matrix by a term in the Hamiltonian of the form,

$$H_{DMI} = -\frac{1}{2}\sum_{ij} \mathbf{D}_{ij} \cdot (\mathbf{S}_i \times \mathbf{S}_j) \tag{2.45}$$

The exchange interaction between spins is a general nomenclature for all interactions that are related to the overlap of different atoms' wavefunctions and Pauli's exclusion principle. The fundamental reason for this overlap can come in different forms.

The most straightforward case is when two neighbouring magnetic atoms

interact via exchange interactions. Given the name of direct exchange, this is the simplest conceptual picture for the exchange interaction. In reality, consider rare earths as an example, where the 4f electrons are strongly localised, not extending very far from the nucleus. This leads to direct exchange interaction being limited in rare earths. Even in transition metals like Fe, Co, and Ni, where the 3d orbitals extend farther from the nucleus, justifying the observed magnetic properties solely through the direct exchange is difficult. Given that these materials are metals, the contribution of conduction electrons becomes pivotal, necessitating an accurate description that considers both the localised and the band character of the electrons.

In metal, the exchange interaction can be mediated by the conduction electrons. Known as RKKY interaction named after Ruderman, Kittel, Kasuya and Yosida, the interaction occurs due to the localised magnetic moments, polarising the conduction electrons that in turn couple to another magnetic moment at a distance r away. This type of exchange tends to be long-range and oscillatory in intensity. In oxides such as MnO and NiO (and fluorides MnF_2) one sees yet another form of indirect exchange, known as superexchange, in this case, the exchange between the magnetic atoms is mediated by a non-magnetic ion. In the case of oxides, the presence of the oxygen atoms leads to a ground state that has a lower kinetic energy for anti-aligned neighbouring magnetic atoms.

This exemplifies that the exchange interaction can arise in different ways, although for our purposes we will limit ourselves to, using proposed values for the exchange parameters, to study the dynamics of these systems without regard for the origin of the interaction [79].

2.3.4 Zeemann Interaction

So far we have discussed internal interactions of the material with itself, interactions which lead to magnetic ordering. Beyond such interactions, one can interact with the system with external perturbations such as magnetic fields. Fundamentally, our problem is to understand the energy of the interaction between an external magnetic field and the electron's magnetic moment. We can start by stating the time-independent Schrodinger equation for an electron in a

static electromagnetic field [83],

$$\frac{1}{2m}\left[\frac{\hbar}{i}\nabla + e\mathbf{A}\right]^2 \psi + V\psi = E\psi \tag{2.46}$$

where ψ is the electron wave function, $\mathbf{A}$ is the vector potential associated with the magnetic field, V is the electric potential that the electron is subjected to by the solid, e is the electron's charge, and E the system energy.

Expanding we get,

$$-\frac{\hbar^2}{2m}\nabla^2\psi + \frac{\hbar}{i}\frac{e}{2m}\left[\nabla\cdot(\mathbf{A}\psi) + \mathbf{A}\cdot\nabla\psi\right] + \left[\frac{e^2}{2m}A^2 + V\right]\psi = E\psi, \tag{2.47}$$

the new interaction that arises from the magnetic field is the second term on the left-hand side. By choosing the Coulomb gauge, one can show that the vector potential and the gradient commute, allowing us to write,

$$-\frac{\hbar^2}{2m}\nabla^2\psi + \frac{\hbar}{i}\frac{e}{m}\left[\mathbf{A}\cdot\nabla\psi\right] + \left[\frac{e^2}{2m}A^2 + V\right]\psi = E\psi \tag{2.48}$$

Furthermore, we have the following identity,

$$\begin{aligned}\nabla\times(\mathbf{B}\times\mathbf{r}) &= \mathbf{B}\nabla\cdot\mathbf{r} - \mathbf{r}\nabla\cdot\mathbf{B}\\ &= (\nabla\cdot\mathbf{r})\mathbf{B} - (\mathbf{B}\cdot\nabla)\mathbf{r}\\ &= [3\mathbf{B} - \mathbf{B}]\\ &= 2\mathbf{B}\end{aligned} \tag{2.49}$$

then we can write,

$$\nabla\times\mathbf{A} = \frac{1}{2}\nabla\times(\mathbf{B}\times\mathbf{r}) \tag{2.50}$$

using these identities, we can write,

$$\begin{aligned}\frac{\hbar}{i}\frac{e}{2m}\mathbf{A}\cdot\nabla\psi &= \frac{\hbar}{i}\frac{e}{m}(\mathbf{B}\times\mathbf{r})\cdot\nabla\psi \\ &= \frac{e}{2m}\mathbf{B}\cdot\left[\mathbf{r}\times\left(\frac{\hbar}{i}\right)\nabla\right]\psi \\ &= \frac{e}{2m}\mathbf{B}\cdot[\mathbf{r}\times\mathbf{p}]\psi \\ &= \frac{e}{2m}(\mathbf{B}\cdot\mathbf{L})\psi \\ &= \frac{\mu_B}{\hbar}\mathbf{L}\cdot\mathbf{B}\psi\end{aligned} \tag{2.51}$$

where we used the definition $\mathbf{L} = \mathbf{r}\times\mathbf{p}$.

This provides us with an interaction that is minimised when the angular momentum, and by extension the magnetic moment of the electron and the external magnetic field, are anti-aligned. This interaction is known as Zeeman energy, given by,

$$E_z = \frac{\mu_B}{\hbar}\mathbf{L}\cdot\mathbf{B} \tag{2.52}$$

This definition allows us to extend our understanding of this interaction to the cases of angular and spin magnetic moment such that the total angular momentum interacts with the external magnetic field with the form:

$$E_z = -\frac{\mu_B}{\hbar}(\mathbf{L}+g_e\mathbf{S})\cdot\mathbf{B} \tag{2.53}$$

2.4 Classification of magnetic order

In previous sections, we have discussed the existence of magnetic order. Due to differences in the character of the interactions between the magnetic moments that make the lattice, different magnetic ground states can be observed. The magnetic moments can arrange themselves in many ways, the most common and discussed, are the ferromagnets, antiferromagnets and ferrimagnets [79], these are known as collinear. More complex arrangements include, but are not limited to, domain-walls, spin-spirals and skyrmions [84–86], known as non-collinear arrangements.

To discuss further, and gain some insight into how the interactions lead to

the ground state spin arrangement of a particular system, we can look at the exchange parameter for some guidance. Recalling that the exchange interaction is given by,

$$H = -\sum_{ij} J_{ij}\mathbf{S}_i \cdot \mathbf{S}_j \tag{2.54}$$

we can see that from this mathematical representation of the interaction, for $J_{ij} > 0$ the energy is minimised when the two spins are aligned with each other, leading to a ferromagnetic ground state, which is the case for Fe and Co. However if $J_{ij} < 0$ the energy is minimised for the two spins being anti-aligned, leading to a state known as the antiferromagnetic ground state, which is the case of NiO, where the material has no net magnetisation, since every site is compensated by an equivalent but oppositely oriented magnetic moment. These two ground states assume that all magnetic moments have the same intensity. In the case of structures known as ferrites, which have chemical formula $MOFe_2O_3$ where M is a divalent cation such as Zn^{2+}, Co^{2+}, Fe^{2+}, Ni^{2+}, Cu^{2+} or Mn^{2+} and garnets with chemical formula $R_3Fe_5O_{12}$ where R is a trivalent rare earth atom. In these systems, different sites will be subject to different crystal fields locally, these in-equivalent sites lead to cases of uncompensated antiferromagnets or ferrimagnets, where, even though the ground state is an antiferromagnet, the system exhibits a net magnetisation [79].

Notice that the ground state is mainly affected by the interaction between the different magnetic moments, so far we only discussed the diagonal part of the exchange interaction. The antisymmetric exchange was first eluded to play a role in the systems ground states in the observation of what was first dubbed, weak ferromagnetism, which turned out to be an antiferromagnetic structure, with a small amount of canting due to DM interaction. The intensity of this canting derives from the interplay between the diagonal and the off-diagonal terms in the exchange matrix [87].

2.5 Heisenberg Hamiltonian

So far we defined the different interactions that define the Hamiltonian of the magnetic system, allowing us to write the total Heisenberg Hamiltonian given by,

$$H = -\sum_{jj'} \mathbf{S}_j \cdot J_{jj'} \cdot \mathbf{S}'_j + \frac{\mu_B}{\hbar} g_e \sum_j \mathbf{B} \cdot \mathbf{S}_j - K \sum_j (\hat{m} \cdot \mathbf{S}_j)^2 \tag{2.55}$$

The different terms have been discussed in previous sections, the first is the exchange interaction, where we include the antisymmetric (DMI) interactions and the exchange anisotropy by writing the exchange constant as a tensor. The use of a tensorial exchange parameter allows the interaction to be modelled in a more general way, where the diagonal terms can be recognised as representing the usual constant exchange interaction, while the off-diagonal terms represent the DM interaction. Therefore, the tensor terms must follow $(J_{jj'})_{\alpha\beta} = -(J_{jj'})_{\beta\alpha}$ for $\alpha \neq \beta$. In other words, the exchange anisotropy manifests itself as an asymmetry in the diagonal terms of the tensorial exchange tensor. The second term is the Zeeman interaction where we renormalised the external magnetic field to incorporate the constants such that $\frac{\mu_B}{\hbar} g_e \mathbf{B} \to \mathbf{B}$. Finally, the last term represents the magneto-crystalline anisotropy.

So far we have given heuristic arguments as to why we expect the proposed spin order in magnetic materials, let's now give a more fundamental analysis of the Heisenberg Hamiltonian.

2.5.1 Ground State

First, let's look a the possible ferromagnetic ground state. In this case we are assuming $J_{ij} > 0$ for all i, j sites in the lattice. Let's consider a system with magnetic moments only interacting via isotropic symmetric exchange interaction. With these simplifications in place, we can simplify the Hamiltonian in Eq. (2.55) to be,

$$H = -\frac{1}{2}\sum_{ij} J_{ij}\mathbf{S}_i \cdot \mathbf{S}_j \tag{2.56}$$

In this discussion, we will assume $\hbar = 1$. We now define our basis; a natural candidate is to write a direct sum of states of the kind $|S, m_s\rangle$ for each magnetic site, where,

$$\begin{aligned}\mathbf{S}_i^2|S, m_s\rangle_i &= S(S+1)|S, m_s\rangle_i \\ \mathbf{S}_i^z|S, m_s\rangle_i &= m_s|S, m_s\rangle_i\end{aligned} \tag{2.57}$$

Assuming a ferromagnetic ground state, $m_s = S$ for all sites, representing the situation where the z-projection of the magnetic moments in every site, assumes its maximum value. Our basis is the direct sum for states of all sites,

$$|\psi\rangle = |S, m_s\rangle_1 \oplus |S, m_s\rangle_2 \oplus \cdots \oplus |S, m_s\rangle_N \tag{2.58}$$

then the ground state gets denoted,

$$|0\rangle = |S, S\rangle_1 \oplus |S, S\rangle_2 \oplus \cdots \oplus |S, S\rangle_N \tag{2.59}$$

To confirm our assumption for the ground state being the ferromagnetic state, we need to show that this state produces the lowest energy for the Hamiltonian in Eq. (2.56). To apply the Hamiltonian in the state given by Eq. (2.59) it is convenient to rewrite the spin operators in the form of the ladder operators, defined by $S_i^{\pm} = S_i^x \pm iS_i^y$, which when operated in the spin states will give,

$$S_i^{\pm}\,|S_i, m_s\rangle = \left[S_i(S_i+1) - m_s\,(m_s \pm 1)\right]^{1/2}|S_i; m_s \pm 1\rangle \tag{2.60}$$

these operators act on states by raising or lowering the z-projection of the local spins. Particularly important to our discussion, are the properties of these ladder operators, that can be written as,

$$\begin{aligned}S_i^{+}\,|S_i, m_s\rangle &= 0 \\ S_i^{-}\,|S_i, -m_s\rangle &= 0\end{aligned} \tag{2.61}$$

which means that attempting to increase the z-projection of the spin angular

momentum past the maximum value, or reduce it below the minimum, leads to a zero eigenvalue.

The Hamiltonian in Eq. (2.56) can be rewritten as,

$$H = -\frac{1}{2}\sum_{i,j} J_{ij}\left[\frac{1}{2}\left(S_i^+ S_j^- + S_i^- S_j^+\right) + S_i^z S_j^z\right] \tag{2.62}$$

Now we know how to operate all terms of Eq. (2.62) in our presumed ground state in Eq. (2.59), by using Eqs. (2.57), (2.60) and (2.61). In the process of evaluating $H|0\rangle$, we will evaluate terms involving the raising ladder operators. From Eq. (2.61), we notice that upon acting on the states that already are at a maximum z-projection angular momentum we get a zero eigenvalue, and since operators labelled in different sites commute, we have,

$$\begin{aligned} S_i^+ S_j^- \left[|S;S\rangle_1 \oplus |S;S\rangle_2 \oplus \ldots \oplus |S;S\rangle_N\right] = 0 \\ S_i^- S_j^+ \left[|S;S\rangle_1 \oplus |S;S\rangle_2 \oplus \ldots \oplus |S;S\rangle_N\right] = 0 \end{aligned} \tag{2.63}$$

Our Hamiltonian is then reduced to,

$$H|0\rangle = -\frac{1}{2}\sum_{i,j} J_{ij} S_i^z S_j^z |0\rangle = -\frac{S^2}{2}\sum_{i,j} J_{ij}|0\rangle = E_0|0\rangle \tag{2.64}$$

resulting in a total energy of,

$$E_0 = -\frac{S^2}{2}\sum_{i,j} J_{ij} \tag{2.65}$$

To show that the eigenvalue E_0 is the ground state, we operate on the general solution in Eq. (2.58),

$$\hat{H}\,|\psi\rangle = E_0^{'}\,|\psi\rangle \tag{2.66}$$

In this case, we will have terms such that,

$$\begin{aligned} &S_i^+ S_j^- \left[|S,m_s\rangle_1 |S,m_s\rangle_2 \ldots |S,m_s\rangle_N\right] \propto \\ &\left[|S,m_s\rangle_1 \ldots |S,m_s+1\rangle_i \ldots |S,m_s-1\rangle_j \ldots |S,m_s\rangle_N\right] \end{aligned} \tag{2.67}$$

By the orthogonality of the basis, we can show that,

$$\begin{aligned} \langle\psi| S_i^+ S_j^- |\psi\rangle = 0 \\ \langle\psi| S_i^- S_j^+ |\psi\rangle = 0 \end{aligned} \tag{2.68}$$

hence, in Eq. (2.62) only the terms that involve S^z are non-zero. We can then write Eq. (2.66) as,

$$-\frac{1}{2}\sum_{i,j} J_{ij} S_i^z S_j^z |\psi\rangle = E_0^{'} |\psi\rangle = -\frac{1}{2}\sum_{i,j} J_{ij} m_s^{(i)} m_s^{(j)} |\psi\rangle \tag{2.69}$$

giving us a total energy that is dependent on a sum of the magnetic moments of all sites, in this case, each site will have a particular magnetic moment z-projection, labelled here by $m_s^{(i)}$. Now noting that, by our construction, $m_z^{(i)} \leq S$, so we have that,

$$E_0^{'} \geq E_0 \tag{2.70}$$

leading to the conclusion that the state Eq. (2.59) is the ground state of the Hamiltonian Eq. (2.56) for $J_{ij} > 0 \; \forall \; i, j$.

It can be shown similarly, although in a more involved procedure, that in the case where $J_{ij} < 0$ the ground state is antiferromagnetic, such that, each site z-direction projection of the local magnetic moments points in the opposite direction to its neighbours [88].

2.5.2 Excited States

So far we only discussed the aspects of the possible ground states represented by the Hamiltonian in Eq. (2.56). Now let's discuss what are the possible excited states for the system, here we will take a similar approach as the original one given by Felix Bloch in [25]. Taking that the ground state exhibits magnetic order, a naive approach to this problem would be to assume that the first excited state would result in a spin flip or lowering of the z-projection of the angular momentum in a particular site,

$$|i\rangle = |S, S\rangle_1 \ldots |S, S-1\rangle_i \ldots |S, S\rangle_N \tag{2.71}$$

where we are defining the state $|i\rangle$ as a state where z-projection of the angular momentum is reduced/fliped, in the i'th site. We can easily show that this solution isn't an eigenvector of the Hamiltonian in Eq. (2.56), because the term $S_i^+ S_j^-$ will increase back the spin on-site i and decrease one in site j, leading to a different eigenstate, i.e. instead you obtain,

$$\begin{aligned} S_i^+ S_j^- \, |j\rangle &= 0 \\ S_i^- S_j^+ \, |j\rangle &= 2S \, |i\rangle \end{aligned} \tag{2.72}$$

note that, in the definition of the basis therefore the Hamiltonian shifts the site where the spin is reduced from the site i to the site j, hence, the assumption that the first excited state is a reduction/flip of the spin in a particular site is not a stable excited state.

To proceed, let's attempt a general state as a solution, composed of a linear combination of a single spin flip in every site, given by,

$$|\psi\rangle = \sum_k f_k \, |k\rangle \tag{2.73}$$

To simplify the notation, let's assume a 1D chain of magnetic moments, and instead of the sum over all the pairs of sites, we sum over all sites, and for each site, sum over its nearest neighbours only. Assuming that all magnetic moments interact with the same intensity with their respective first neighbours, this further simplifies Eq. (2.62) to,

$$\begin{aligned} H = -\tfrac{1}{2} \textstyle\sum_k J[\tfrac{1}{2} \left(S_k^+ S_{k+1}^- + S_k^- S_{k+1}^+\right) + S_k^z S_{k+1}^z \\ + \tfrac{1}{2} \left(S_k^+ S_{k-1}^- + S_k^- S_{k-1}^+\right) + S_k^z S_{k-1}^z] \end{aligned} \tag{2.74}$$

Now if we apply H as given in Eq. (2.74) to the state in Eq. (2.73), as done in Appendix C we can show that the coefficients of the linear combination are given by,

$$f_i(x_i) \propto e^{iqx_i} \tag{2.75}$$

So, the first excited state of this system is, accounting for normalisation, given by,

$$|q\rangle = \frac{1}{\sqrt{N}} \sum_i e^{i\boldsymbol{R}_i \cdot \boldsymbol{q}} |i\rangle \tag{2.76}$$

where $\boldsymbol{R}_i$ are the position vector of the i'th magnetic moment and N is the number of magnetic moments in the system. A more general solution can be achieved by rewriting the excited state in terms of the ground state,

$$|q\rangle = \frac{1}{\sqrt{2SN}} \sum_1 e^{i\boldsymbol{R}_i \cdot \boldsymbol{q}} S_i^- |0\rangle \tag{2.77}$$

This state allows us to evaluate the dispersion relation for the excited state, which is also done in Appendix C which is given by,

$$E(q) = JS[1 - \cos(qa)] \tag{2.78}$$

To understand the physical meaning of the excited state, it is instructive to verify the total angular momentum of this state. To achieve this, a few definitions are useful. First, we can define our ladder operators in Fourier space,

$$S^\alpha(\mathbf{q}) = \sum_i e^{i\boldsymbol{R}_i \cdot \boldsymbol{q}} S_i^\alpha \qquad (\alpha = x, y, z, +, -) \tag{2.79}$$

Using this definition and the commutation relation in Eqs. (2.14), (2.15) and (2.16) we can also show,

$$[S^+(\mathbf{k}_1), S^-(\mathbf{k}_2)] = 2\hbar S^z(\mathbf{k}_1 + \mathbf{k}_2) \tag{2.80}$$

$$[S^z(\mathbf{k}_1), S^\pm(\mathbf{k}_2)] = \pm\hbar S^\pm(\mathbf{k}_1 + \mathbf{k}_2) \tag{2.81}$$

Using these definitions we can evaluate,

$$\langle q| S_i^z |q\rangle = \hbar S - \frac{\hbar}{N} \tag{2.82}$$

Notice that this result shows that the change in magnetic moment in a single site in the magnetic lattice is $\hbar$ divided by the number of sites. In this excited state, the total change in magnetisation is $\hbar$, but this change is shared among

all sites.

Instead of our naive idea of one magnetic moment flipping somewhere in the chain, we are faced with a change that is dispersed through the chain and has an associated wave. In a semiclassical approach, these waves appear as a set of magnetic moments precessing with a certain phase between them, which was coined as a spin wave.

An important point to note is that, if one attempts to create a second excited state by the same logic one will realise that the two-wave state is not an eigenstate of the Hamiltonian. This complication arises from the interaction that starts to be present in the case where multiple magnons are excited in the system. Hence, to understand the excitations in the system with multiple magnons is necessary a different formalism. Historically this was achieved using second quantisation, and the first, and most convenient, approach was proposed by Holtein and Primakoff. In the next section, we will describe a general formulation that allows us to provide a general formulation for the second quantisation of spin systems.

2.6 Bosonic transformation

Previously we were interested in the eigenstates of the magnetic system. This approach allowed us to show that the first excited state is an oscillation in the magnetic lattice, that has a total magnetic moment change of $\hbar$.

This approach is less advantageous when dealing with the many-body space of excitations, which is the case when we will intend to deal with multiple magnon excitations.

To generalise the problem we will redefine the problem using second quantisation, also known as an occupation number representation. This formalism is useful for describing quantum many-body systems.

To illustrate this methodology we will take a detour, and study the quantum harmonic oscillator in second quantisation.

2.6.1 The quantum harmonic oscillator

The quantum harmonic oscillator is perhaps the most important model in physics. In quantum mechanics, the harmonic oscillator is the basis to get insights into the inner workings of the methods applied. We will introduce the concept of bosonic transformation using the harmonic oscillator, as it is a commonly familiar problem. Our goal is to connect the insights gained with the harmonic oscillator with the similar problem of oscillating magnetic moments as is the case for magnons. Here we will assume the toy model of a 1D harmonic oscillator that can be imagined as a mass m on a spring with force constant k. This system is represented by the Hamiltonian,

$$\hat{H} = \frac{\hat{p}_x^2}{2m} + \frac{1}{2}k\hat{x}^2 \tag{2.83}$$

where $\hat{p}_x$ is the linear momentum operator and $\hat{x}$ the spacial displacement operator. If one applies this to the Schrodinger equation, and uses the operator form of the momentum operator, we get,

$$\left(-\frac{\hbar}{2m}\frac{d^2}{dx^2} + \frac{1}{2}kx^2\right)\psi_E(x) = E\psi_E(x) \tag{2.84}$$

the solution to the eigenspectrum problem is well known, and given by the following eigenstates and eigenenergies,

$$\psi_n(x) = \frac{1}{\sqrt{2^n n!}}\left(\frac{m\omega}{\pi\hbar}\right)^{1/4} H_n(\zeta)e^{-\zeta^2/2} \tag{2.85}$$

$$E_n = \left(n + \frac{1}{2}\right)\hbar\omega, \qquad n = 0, 1, 2, 3... \tag{2.86}$$

where $\omega \equiv \sqrt{k/m}$, $\zeta \equiv x\sqrt{m\omega/\hbar}$ and $H_n(z)$ are the Hermite polynomials of order n in z.

This solution was given in the position space, this could be solved just as well for the momentum space. In both solutions, the nature of the systems remains the same. One can ask why we don't just deal with the energy eigenstates, independent of the particular wave function of the system. In this case,

the system will be defined by which energy state it is in. This point of view can be achieved by defining a basis for these possible energy states of the system of the form,

$$\hat{H}\left|n\right\rangle = E_n\left|n\right\rangle \tag{2.87}$$

here the system is defined by which energy state it is in. This procedure is the essence of the so-called second quantisation, because defining the system in terms of the states it can be in, allows us to describe many-particle systems, by the number of particles that are in any particular state.

We now rewrite the Hamiltonian in terms of the known eigenenergies of the system,

$$\hat{H}\left|n\right\rangle = \left(n + \frac{1}{2}\right)\hbar\omega\left|n\right\rangle \tag{2.88}$$

hence, we need to rewrite the Hamiltonian such that it is dependent on some particular operator $\hat{A}$. Equating Eqs. (2.83) and (2.88) we have,

$$\hat{A} = \frac{\omega m}{2\hbar}\left(\hat{x}^2 + \frac{\hat{p}_x^2}{\omega^2 m^2} - \frac{\hbar}{\omega m}\right) \tag{2.89}$$

Notice that this operator depends on quadratic terms, allowing us to factorise it in a pair of complex operators that are conjugate to each other,

$$\hat{A} = a^\dagger a \tag{2.90}$$

where,

$$\begin{aligned} \hat{a}^\dagger &= \sqrt{\frac{\omega m}{2\hbar}}\left(\hat{x} - \frac{i}{m\omega}\hat{p}_x\right) \\ \hat{a} &= \sqrt{\frac{\omega m}{2\hbar}}\left(\hat{x} + \frac{i}{m\omega}\hat{p}_x\right) \end{aligned} \tag{2.91}$$

having the functional form of these operators and the eigenstates from Eq. (2.85), we can show that,

$$\hat{a}\,|n\rangle = \sqrt{n}\,|n-1\rangle\,, \qquad \hat{a}^\dagger\,|n\rangle = \sqrt{n+1}\,|n+1\rangle \tag{2.92}$$

and finally, we can define,

$$\hat{H} = \left(a^\dagger a + \frac{1}{2}\right)\hbar\omega, \tag{2.93}$$

This form appears in many fields of physics, in every situation where something is oscillating this form is a fair model of the system. This picture represents the number of quanta of energy stored in the harmonic oscillator. In general when the operators $a^\dagger$ and a are thought to create a particle that usually, with an exception for the harmonic oscillator, is given a name. In the case of lattice vibrations, the particles are called phonons, in the case of the oscillation of magnetic moments it's called magnons. In this narrative, the operator $a^\dagger a$ is seen as an occupation number operator, which counts the number of particles occupying a certain state,

$$a^\dagger a\,|n\rangle = n\,|n\rangle \tag{2.94}$$

usually indicated by $\hat{n}$. The absence of particles in the vacuum state $|n=0\rangle$ though does not necessarily imply a state of zero energy. As it mostly happens, it is characterised by a specific energy. For the harmonic oscillator (4), this vacuum energy corresponds to $E_0 = \hbar\omega/2$. And anytime a particle is added to the system, its energy increases by $\Delta E = \hbar\omega$ which is a quantum of energy.

To gain a more general picture that will be useful for extended systems, we can create a state with multiple harmonic oscillators,

$$|n_1, n_2, ..., n_N\rangle = \prod_{i=1}^{N} \frac{\left(\hat{a}_i^\dagger\right)^{n_i}}{\sqrt{n_i!}}\,|0\rangle \tag{2.95}$$

This generic multiple harmonic oscillator state is the direct product of multiple single harmonic oscillator states. The total energy in this case is the sum of the total number of quanta in each harmonic oscillator.

2.6.2 General bosonic transformation for magnetic systems

Having discussed the second quantisation of the harmonic oscillator, we now turn our attention to the magnetic systems. In this case, we wish to second quantize the Hamiltonian which is formed of spin operators, so our goal is to rewrite the spin operators in terms of the creation and annihilation of quanta of energy (magnons) in the magnetic lattice of the system, which we will be calling bosonic transformation.

There are multiple ways to achieve this goal. In this section, we will follow a general form of the bosonic transformation [89]. To tie the usual literature approach we will derive from this general approach both the Holstein-Primakoff and the Dyson-Mandaleev transformations, the former being the most widely used one, and the one we will focus on in this thesis. We will discuss the situations in which each gives a more insightful description of the system, keeping in mind that both are correct and achieve the same results when applied in their common ground of approximation.

Historically the Holstein-primakoff transformation was the first description of magnetic materials under the second quantisation formalism. Owing that the Hamiltonian for a magnetic system can be written in terms of the S^+,S^- and S^z operators, Holstein and Primakoff had the task of devising a way to relate these operators with the creation and annihilation operators defined in the second quantisation formalism.

The main obstacle to accomplishing this goal arises from the fact that for a given particle total spin S, we have an associated S^z that depends on S, giving us either $S^z = \pm S, \pm(S-1), \ldots, 0$ or $S^z = \pm S, \pm(S-1), \ldots, \pm 1/2$, depending if S is integer of half-integer. In their seminal paper, Holstein and Primakoff introduced a different way of counting the states that matched the second quantisation spirit. They introduced a separate counting integer unrelated to either value as an auxiliary parameter, such that,

$$S^z = S - n, \qquad \text{where} \quad n = 0, 1, 2, \ldots, 2S \tag{2.96}$$

Notice that, this way, we changed the way we define our basis, going from

$|S; S^z\rangle$ to $|n\rangle$, leaving the S implicit for compactness. Now instead of counting from $-S$ to S in integer values, we count from 0 to $2S$. The number n can be thought of as a "spin deviation" operator, given by,

$$n_i = S - S_i^z \tag{2.97}$$

taking that the maximum magnetic moment of each site is given by S, what this operator does is represent the difference between the z-component of the spin of the i'th atom and its maximum value, such that, if a site is at its maximum value the resulting deviation is zero.

This is the main clever step of the Holstein-Primakoff transformation, by introducing this operator the authors set the parallel between the number operator, in the second quantisation formalism, and the S^z operator. Taking this into account one can write,

$$a_i^\dagger a_i = S - S_i^z \tag{2.98}$$

$$S_i^z = S - a_i^\dagger a_i \tag{2.99}$$

We also need to rewrite the raising and lowering operators S^+,S^- in terms of the creation and annihilation operators. To note the unknown dependence of these operators, for this derivation, we will note them as a function of the creation and annihilation operators, which we will henceforth note as, $S^+\left(a^\dagger, a\right)$, $S^-\left(a^\dagger, a\right)$. In this step, we can follow the particular path given in the Holstein-Primakoff paper, but make a more rigorous discussion.

A few important points need to be noted, first of all, the bosonic operators follow the canonical bosonic commutation relation,

$$\left[a_i^\dagger, a_j\right] = \delta_{ij} \tag{2.100}$$

hence they are a pair of non-commuting operators, i.e. they follow the theorems given in [90], and in the basis of the auxiliary parameter n, we have the following requirement for the raising and lowering operators,

$$S^{+}\left(a^{\dagger},a\right)|2S\rangle=0 \tag{2.101}$$

$$S^{-}\left(a^{\dagger},a\right)|0\rangle=0 \tag{2.102}$$

as well as the usual commutation relations for the spin operators,

$$\left[S_{i}^{\pm},S_{j}^{z}\right]=\mp S_{i}^{\pm}\delta_{ij} \tag{2.103}$$

$$\left[S_{i}^{+},S_{j}^{-}\right]=2S_{i}^{z}\delta_{ij} \tag{2.104}$$

so the functional form for $S^{+}\left(a^{\dagger},a\right)$,$S^{-}\left(a^{\dagger},a\right)$ and $S^{z}\left(a^{\dagger},a\right)$ will obey the relations given on Eqs. (2.101),(2.102),(2.103) and (2.104).

$$\begin{aligned}
\left[S^{+},S^{z}\right] &= S^{+}S^{z}-S^{z}S^{+}=-S^{+}\\
&= S^{+}\left[S-a^{\dagger}a\right]-\left[S-a_{i}^{\dagger}a_{i}\right]S^{+}=-S^{+}\\
&= S^{+}S-S^{+}a^{\dagger}a-SS^{+}+a^{\dagger}aS^{+}=-S^{+}\\
&= a^{\dagger}aS^{+}-S^{+}a^{\dagger}a=-S^{+}\\
&= \left[a^{\dagger}a,S^{+}\right]=-S^{+}\\
&= \left[S^{+},a^{\dagger}a\right]=S^{+}\\
&= \left[S^{+},a^{\dagger}\right]a+a^{\dagger}\left[S^{+},a\right]=S^{+}\\
&= \left[a^{\dagger},S^{+}\right]a+a^{\dagger}\left[a,S^{+}\right]=-S^{+}\\
&= -\frac{\partial S^{+}}{\partial a}a+a^{\dagger}\frac{\partial S^{+}}{\partial a^{\dagger}}=-S^{+}\\
&= a^{\dagger}\frac{\partial S^{+}}{\partial a^{\dagger}}-\frac{\partial S^{+}}{\partial a}a=-S^{+}
\end{aligned} \tag{2.105}$$

where we used the commutator identity $[A,BC]=[A,B]C+B[A,C]$ and the following general relations [90], given in appendix F as theorem 6,

$$[a,f]=\frac{\partial f}{\partial a^{\dagger}} \tag{2.106}$$

$$[a^{\dagger},f]=-\frac{\partial f}{\partial a} \tag{2.107}$$

here $f \equiv f\left(a^{\dagger}, a\right)$.

Having defined the spin operators as functions of the creation and annihilation operators, define a general function for S^{-} as a polynomial expansion of $a^{\dagger}$ and a as,

$$S^{-} = \sum_{m,n=0}^{\infty} \overline{S}^{-}_{m,n} a^{\dagger m} a^{n} \tag{2.108}$$

where we have defined $\overline{S}^{-}_{m,n}$ as a c-number. Substituting Eq. (2.108) in the result from Eq. (2.105) and taking that,

$$\frac{\partial S^{-}}{\partial a^{\dagger}} = \sum_{m,n=0}^{\infty} m \overline{S}^{-}_{m,n} a^{\dagger m-1} a^{n} \tag{2.109}$$

we get the following equality from Eq. (2.105),

$$a^{\dagger} \sum_{m,n=0}^{\infty} m \overline{S}^{-}_{m,n} a^{\dagger m-1} a^{n} - \sum_{m,n=0}^{\infty} n \overline{S}^{-}_{m,n} a^{\dagger m} a^{n-1} a = \sum_{m,n=0}^{\infty} \overline{S}^{-}_{m,n} a^{\dagger m} a^{n} \tag{2.110}$$

which gives us the relationship,

$$m \overline{S}^{-}_{m,n} - n \overline{S}^{-}_{m,n} = \overline{S}^{-}_{m,n} \tag{2.111}$$

that dividing all terms in Eq. (2.111) by $\overline{S}^{-}_{m,n}$ we get the relationship,

$$m = n + 1 \tag{2.112}$$

therefore, using this index relation on our definition for S^{-} in Eq. (2.108), we can then show,

$$\begin{aligned} S^{-} &= \sum_{n=0}^{\infty} \overline{S}^{-}_{m,n} a^{\dagger m} a^{n} \\ &= \sum_{n=0}^{\infty} \overline{S}^{-}_{n+1,n} a^{\dagger n+1} a^{n} \\ &= a^{\dagger} \sum_{n=0}^{\infty} \overline{S}^{-}_{n+1,n} a^{\dagger n} a^{n} \\ &= a^{\dagger} \Phi^{-} \end{aligned} \tag{2.113}$$

here we defined $\Phi^- = \sum_{n=0}^{\infty} \overline{S}^-_{n+1,n} a^{\dagger n} a^n$. For our purpose, Φ^- only needs to be regarded as some function of the creation and annihilation operators. Following similar steps, we can show a corresponding relation for the raising operator, given by, $S^+ = \Phi^+ a$.

Now we need to argue some procedure to justify a functional form for Φ^+ and Φ^-.

From the definitions $S^+ = \Phi^+ a$ and $S^- = a^\dagger \Phi^-$, we have that,

$$\begin{aligned} S^+ S^- &= \Phi^+ a a^\dagger \Phi^- \\ S^- S^+ &= a^\dagger \Phi^- \Phi^+ a \end{aligned} \tag{2.114}$$

To proceed forward, note that,

$$\mathbf{S}^2 = S^- S^+ + S^z \left(S^z + 1\right) \tag{2.115}$$

and since the eigenvalues of $\mathbf{S}^2$ to be given by $S(S+1)$, and substituting Eqs. (2.114) and (2.99), into Eq. (2.115) we have,

$$S(S+1) = a^\dagger \Phi^- \Phi^+ a + \left(S - a^\dagger a\right)\left(S - a^\dagger a\right) + \left(S - a^\dagger a\right) \tag{2.116}$$

leading to,

$$a^\dagger \Phi^- \Phi^+ a = 2S a^\dagger a - a^\dagger a^\dagger a a \tag{2.117}$$

From this, we can assume that (regardless of the assumption on the part of the ground state),

$$\Phi^- \Phi^+ = 2S - a^\dagger a \tag{2.118}$$

Thus, we have some freedom as far as the functional form of both Φ^+ and Φ^-, we need to fulfil Eq. (2.118).

We can show that the Holstein-Primakoff transformation is just one of the many possibilities that fulfil Eq. (2.118). In this particular case the choice,

$$\Phi^+ = \Phi^- = \sqrt{2S - a^\dagger a} \tag{2.119}$$

while the Dyson-Malèev transformation comes from the choice,

$$\begin{aligned}\Phi^{+} &= \sqrt{2S}\left(1-\frac{a^{\dagger}a}{2S}\right)\\ \Phi^{-} &= \sqrt{2S}\end{aligned} \tag{2.120}$$

With this in mind, we can then define the Holstein-Primakoff transformation by,

$$\begin{cases} S_i^{+} &= (2S)^{1/2}\phi(\hat{n})a_i, \\ S_i^{-} &= (2S)^{1/2}a_i^{\dagger}\phi(\hat{n}), \\ S_i^{z} &= S - a_i^{\dagger}a_i \end{cases} \tag{2.121}$$

assuming the ground state to be defined such that $S_i^z = S - a_i^{\dagger}a_i$, and we have defined,

$$\phi(\hat{n}) = \left(1-\frac{a_i^{\dagger}a_i}{2S}\right)^{1/2} \tag{2.122}$$

The main complication with this approach is the appearance of operators under a square root. Because of this side effect of the transformation, the explicit way of working with it requires a series expansion of Eq. (2.122), usually taken to be,

$$\phi(\hat{n}) = 1 - \frac{\hat{n}_i}{4S} - \frac{\hat{n}_i^2}{32S^2} - \frac{\hat{n}_i^3}{128S^3} - \dots \tag{2.123}$$

With this, we need some physical reasoning to justify our choice of truncation. In the original paper, the authors proceeded with the same assumption applied by Bloch when he derived the $T^{3/2}$ dependence of the magnetisation at low temperatures. The assumption is to define a system in quasi-saturation, i.e. at low temperatures the system will deviate very little from its saturation state. In practice, this leads to a justification to truncate our expansion in Eq. (2.123) in the first term. Furthermore, for situations where $S >> 1$ the higher

order terms in Eq. (2.123) will be considerably less intense.

2.7 Inelastic scattering Theory

As previously discussed, one of our interests is to study the scattering of neutrons and electrons by magnons. In this section, we will describe the general theoretical methodology, that predicts the inelastic scattering of particles by many-body systems.

Scattering neutrons, high-energy electrons, and photons by many-body systems represent critical approaches for gaining insights into both the spatial and dynamical structures, including the excitation spectrum, of the system under study. Elastic scattering reveals the spatial structure, while the analysis of inelastically scattered particles tracks the system's excitations.

The theory of inelastic scattering has been developed in a general way by Van Hove [91] and has been specialised in many different books and review papers for different radiative probes, both for spectral analysis [92–95] and imaging [96], for which the interaction Hamiltonian between the probe and the system is known.

Here we will be interested in the momentum-resolved spectral analysis of the magnons. To this end, we will define the double differential cross-section.

2.7.1 Double-differential cross-section

During a scattering experiment, a particle beam is directed onto a sample. The double-differential cross-section is the relative intensity of the inelastically scattered particles to the total incoming particles.

Suppose we set up a particle counter and measure the number of particles scattered in a given direction $\hat{l} = \mathbf{r}/r$ as a function of their energy E_1. The distance of the counter from the target is assumed to be large compared to the dimension of the counter and the target, so the small angle $d\Omega$ defined by the counter is well defined, as shown in figure 2.2.

The double-differential cross-section is defined by the equation,

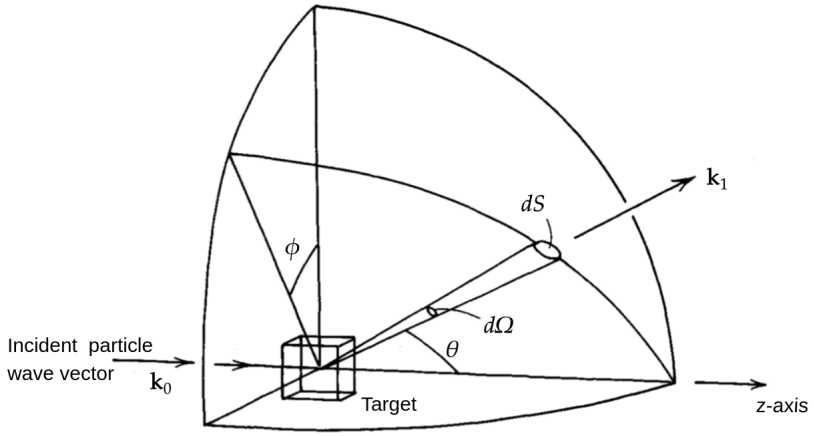

Figure 2.2: Diagram representing the scattering process for an incident particle with momentum $\hbar\mathbf{k}_0$ being scattered to a final momentum $\hbar\mathbf{k}_1$.

$$\frac{d^2\sigma}{d\Omega dE_1} = \frac{1}{N}\frac{\begin{array}{l}(\text{number of particles scattered per sec into a solid angle } d\Omega \\ \text{in the direction } \hat{\mathbf{l}} \text{ with energies between } E_1 \text{and } E_1 + dE_1)\end{array}}{\begin{array}{l}(\text{number of incoming particles per sec and per area} \\ \text{along the z-direction with momentum } \hbar\mathbf{k}_0 \text{ and energy } E_0)\end{array}} \tag{2.124}$$

where N is the number of scatterers in the target, or summarised as,

$$d^2\sigma = \frac{1}{N}\frac{j_1(\mathbf{r}, \mathbf{k}_1, E_1)\cdot\hat{\mathbf{l}}r^2 d\Omega dE_1}{(j_0)_z} \tag{2.125}$$

Here, $j_1(\mathbf{r}, \mathbf{k}_1, E_1)$ is the current density of scattered particles at a distance $|\mathbf{r}|$ from the target, with momentum $\hbar\mathbf{k}_1$ and energy E_1. In the denominator, we have the impinging particle current density $(j_0)_z$. Note that the dimensions of the numerator are $[\text{time}]^{-1}$ while the flux in the denominator has dimensions $[\text{area}]^{-1}[\text{time}]^{-1}$, thus, the cross-section is an effective area of interaction between the probe and the target, for a given energy.

The numerator of Eq. (2.125) can be thought as the number of particles that are scattered into a group of states in a volume in phase space of volume $d\mathbf{k}_1$ around $\mathbf{k}_1$,

$$N_0 \sum_{n_0,n_1} P_{n_0} w(n_0, \mathbf{k}_0 \rightarrow n_1, \mathbf{k}_1) D(\mathbf{k}_1) d\mathbf{k}_1 \tag{2.126}$$

Here $D(\mathbf{k}_1)$ is the density of plane-wave particles in k-space, which will be defined by the box normalisation in a periodic volume V, given by,

$$D(\mathbf{k}_1) = \frac{V}{(2\pi)^3} \tag{2.127}$$

and

$$D(\mathbf{k}_1) d\mathbf{k}_1 = \frac{V}{(2\pi)^3} k_1^2 d\Omega dk_1 \tag{2.128}$$

where N_0 is the number of particles in state $|\mathbf{k}_0\rangle$. The states n_0 and n_1, characterise the different states the system can be in before and after the scattering event. The quantity $w(n_0, \mathbf{k}_0 \rightarrow n_1, \mathbf{k}_1)$ is the transition rate for the situation where the particle beam gets scattered from the initial state $|\mathbf{k}_0\rangle$ to a final state $|\mathbf{k}_1\rangle$ while the system undergoes a transition from state $|n_0\rangle$ to state $|n_1\rangle$, and P_{n_0} is the probability of finding the system in state $|n_0\rangle$ before scattering.

Assuming a weak interaction during the scattering, the transition rate can be calculated in the first Born-approximation,

$$w(n_0, \mathbf{k}_0 \rightarrow n_1, \mathbf{k}_1) = \frac{2\pi}{\hbar} |\langle n_0, \mathbf{k}_0 | H_{inter} | n_1, \mathbf{k}_1 \rangle|^2 \delta(E_{n_0} + E_0 - E_{n_1} - E_1) \tag{2.129}$$

Here, H_{inter} represents the interaction Hamiltonian governing the interaction between the particle beam and the system. The delta function ensures energy conservation, taking into account that the beam undergoes an energy change from E_0 to E_1, while the system an energy transition from an initial state with energy E_{n_0} to a final state with energy E_{n_1}.

Hence, the problem gets summarised to a specification of the interaction Hamiltonian.

Chapter 3

Spin scattering function for magnetic thin films

3.1 Magnon Dynamics

Having defined the basic bosonic transformation in the form of the Holstein-Primakoff, we now turn our attention to discussing the usage of the method to evaluate the spin wave spectra. In particular, we will take steps to define this procedure having a thin film in mind.

We start by using the Heisenberg Hamiltonian as previously defined, with tensorial exchange parameter J_{ij}, an external magnetic field B and a magneto-crystalline anisotropy K,

$$H = -\sum_{jj'} \mathbf{S}_j \cdot J_{jj'} \cdot \mathbf{S}'_j + 2\mu_B B \sum_j \hat{\mathbf{b}} \cdot \mathbf{S}_j - K \sum_j (\hat{\mathbf{m}} \cdot \mathbf{S}_j)^2 \tag{3.1}$$

where we are modelling an insulating spin-lattice, with magnetic moments at lattice points labelled by indexes j and j' which are represented mathematically by the spin operator vectors, $\mathbf{S}_j$ and $\mathbf{S}'_j$, and we define the orientation of the magneto-crystalline anisotropy and the external magnetic field, with the unit vectors $\hat{\mathbf{m}}$ and $\hat{\mathbf{b}}$, respectively. To make the spatial orientation of the spins in the lattice explicit, we will employ the 'Küblers trick' [97,98], where we will define the spin operator in the local reference frame ($\bar{\mathbf{S}}_j$), connected to the laboratory reference frame ($\mathbf{S}_{j'}$), by the unitary matrix $\mathcal{R}_j$ which is defined such that in the local reference frame, the spin always points in the z-direction, given by,

$$\mathcal{R}_j = \begin{pmatrix} \cos\theta_j \cos\phi_j & \cos\theta_j \sin\phi_j & -\sin\theta_j \\ -\sin\phi_j & \cos\phi_j & 0 \\ \sin\theta_j \cos\phi_j & \sin\theta_j \sin\phi_j & \cos\theta_j \end{pmatrix} \tag{3.2}$$

such that, $\bar{\mathbf{S}}_j = \mathcal{R}_j \cdot \mathbf{S}_j$. where θ_j and ϕ_j are the polar and azimuthal angles, respectively, of the spins in the laboratory reference frame.

Similarly for the magneto-crystalline, and Zeeman terms, we need to define the unit vectors that define the orientation of the anisotropy and the magnetic field. Here we denote, $\mathbf{m}$ as a unit vector specifying the orientation of the magneto-crystalline anisotropy axis. This vector can be expressed in spherical coordinates as follows,

$$\hat{\mathbf{m}} = (\sin\eta_m \cos\delta_m, \sin\eta_m \sin\delta_m, \cos\eta_m) \tag{3.3}$$

while the magnetic field orientation is given by the unit vector $\hat{\mathbf{b}}$ which similarly is given by

$$\hat{\mathbf{b}} = (\sin\eta_b \cos\delta_b, \sin\eta_b \sin\delta_b, \cos\eta_b) \tag{3.4}$$

where η represents the polar angle and δ is the azimuthal angle, the different subscript label the magneto-crystalline interaction with m and the Zeeman interaction with b. Applying these definitions allows us the freedom to define the orientation of the magneto-crystalline and external field orientation. We can rewrite the terms in Eq. (3.1) using the 'Küblers trick' defined by the transformation in Eq. (3.2). As an example, the exchange terms can be rewritten as follows,

$$\begin{aligned} H_{ex} &= -\frac{1}{2}\sum_{jj'} \mathbf{S}_j \cdot J_{jj'} \cdot \mathbf{S}_{j'} \\ &= -\frac{1}{2}\sum_{jj'}\sum_{\alpha,\beta,\gamma,\delta} \left(\mathcal{R}_j^{-1}\right)_{\alpha\gamma} \overline{\mathbf{S}}_{j\gamma} (J_{jj'})_{\alpha\beta} \left(\mathcal{R}_{j'}^{-1}\right)_{\beta\delta} \overline{\mathbf{S}}_{j'\delta} \\ &= -\frac{1}{2}\sum_{jj'}\sum_{\alpha,\beta,\gamma,\delta} \overline{\mathbf{S}}_{j\gamma} (\mathcal{R}_j)_{\gamma\alpha} (J_{jj'})_{\alpha\beta} \left(\mathcal{R}_{j'}^{-1}\right)_{\beta\delta} \overline{\mathbf{S}}_{j'\delta} \\ &= -\frac{1}{2}\sum_{jj'} \overline{\mathbf{S}}_j \cdot F_J(j,j') \cdot \overline{\mathbf{S}}_{j'} \end{aligned} \tag{3.5}$$

where we have defined,

$$F_J(j,j') = (\mathcal{R}_j \cdot J_{jj'} \cdot \mathcal{R}_{j'}^{-1}) \tag{3.6}$$

we have used Latin letters to note the lattice sites, and Greek letters for cartesian orientations x, y and z. Notice that this enables us to define a different orientation for each site of a chosen lattice, allowing studies of ferromagnetic, ferrimagnetic and antiferromagnetic materials as well as different non-colinear spin textures.

This same transformation, applied to the magneto-crystalline term gives,

$$\begin{aligned} H_{_K} =& - K \sum_i (\hat{\mathbf{m}} \cdot \mathbf{S}_j)^2 \\ =& - K \sum_j \left(\hat{\mathbf{m}} \cdot \mathcal{R}_{\mathbf{j}}^{-\mathbf{1}} \overline{\mathbf{S}}_j\right)^2 \\ =& - K \sum_j (A_{jx}\overline{S}_{jx} + A_{jy}\overline{S}_{jy} + A_{jz}\overline{S}_{jz})^2 \end{aligned} \tag{3.7}$$

similarly, the Zeeman term is given by,

$$\begin{aligned} H_{_B} =& 2\mu_B \mathbf{B} \sum_j \hat{\mathbf{b}} \cdot \mathbf{S}_j \\ =& 2\mu_B \mathbf{B} \sum_j (\hat{\mathbf{b}} \cdot \mathcal{R}_{\mathbf{j}}^{-\mathbf{1}} \overline{\mathbf{S}}_j) \\ =& 2\mu_B \mathbf{B} \sum_j (A_{jx}\overline{S}_{jx} + A_{jy}\overline{S}_{jy} + A_{jz}\overline{S}_{jz}) \end{aligned} \tag{3.8}$$

where we defined,

$$\begin{cases} A_{jx} = & \sin\eta\cos\theta_j\cos(\delta - \phi_j) - \cos\eta\sin\theta_j \\ A_{jy} = & \sin\eta\sin(\delta - \phi_j) \\ A_{jz} = & \sin\eta\sin\theta_j\cos(\delta - \phi_j) + \cos\eta\cos\theta_j \end{cases} \tag{3.9}$$

where η and δ can be either the polar and azimuthal angles for the magneto-crystalline or magnetic field.

Now we move to the second quantisation picture, by using the Holstein-Primakoff transformation,

$$\begin{cases} S_j^x &= \frac{\sqrt{2S_j}}{2}\left(\phi(\hat{n}_j)a_j + a_j^\dagger\phi(\hat{n}_j)\right), \\ S_j^y &= \frac{\sqrt{2S_j}}{2i}\left(\phi(\hat{n}_j)a_j - a_j^\dagger\phi(\hat{n}_j)\right), \\ S_j^z &= S_j - \hat{n}_j \end{cases} \tag{3.10}$$

let's perform our transformation only in the exchange terms to exemplify the procedure. Let's substitute Eq. (3.10) in the exchange term given in Eq. (3.1) with the result from Eq. (3.5) in mind, leading to,

$$\begin{aligned} H = -\tfrac{1}{2}\textstyle\sum_{jj'} \quad & \sqrt{2S_j}\tfrac{a_j^\dagger\phi_j + \phi_j a_j}{2} \quad \Big[F_J(j,j')_{xx}\sqrt{2S_{j'}}\tfrac{a_{j'}^\dagger\phi_{j'} + \phi_{j'}a_{j'}}{2} \\ & & + F_J(j,j')_{xy}\sqrt{2S_{j'}}\tfrac{a_{j'}^\dagger\phi_{j'} - \phi_{j'}a_{j'}}{2i} \\ & & + F_J(j,j')_{xz}\left(S_{j'} - a_{j'}^\dagger a_{j'}\right)\Big] \\ + \quad & \sqrt{2S_j}\tfrac{a_j^\dagger\phi_j - \phi_j a_j}{2i} \quad \Big[F_J(j,j')_{yx}\sqrt{2S_{j'}}\tfrac{a_{j'}^\dagger\phi_{j'} + \phi_{j'}a_{j'}}{2} \\ & & + F_J(j,j')_{yy}\sqrt{2S_{j'}}\tfrac{a_{j'}^\dagger\phi_{j'} - \phi_{j'}a_{j'}}{2i} \\ & & + F_J(j,j')_{yz}\left(S_{j'} - a_{j'}^\dagger a_{j'}\right)\Big] \\ + \quad & \left(S_j - a_j^\dagger a_j\right) \quad \Big[F_J(j,j')_{zx}\sqrt{2S_{j'}}\tfrac{a_{j'}^\dagger\phi_{j'} + \phi_{j'}a_{j'}}{2} \\ & & + F_J(j,j')_{zy}\sqrt{2S_{j'}}\tfrac{a_{j'}^\dagger\phi_{j'} - \phi_{j'}a_{j'}}{2i} \\ & & + F_J(j,j')_{zz}\left(S_{j'} - a_{j'}^\dagger a_{j'}\right)\Big] \end{aligned} \tag{3.11}$$

Now the procedure of expanding $\phi(\hat{n})$ given by,

$$\phi(\hat{n_j}) = 1 - \frac{\hat{n}_j}{4S_j} - \frac{\hat{n}_j^2}{32S_j^2} - \frac{\hat{n}_j^3}{128S_j^3} - \dots \tag{3.12}$$

leads to a Hamiltonian that has an infinite number of terms:

$$H = \sum_{n=0}^{\infty} H_n \tag{3.13}$$

where H_n represents a term that involves n operators, e.g., $H_4 \propto a_i^\dagger a_j a_k^\dagger a_l$. In this summation scheme, H_0 is given by,

$$H_0 = -\frac{1}{2}\sum_{jj'} S_j S_{j'} F_J(j,j')_{zz} \tag{3.14}$$

represents the ground state, H_1 is given by,

$$H_1 = -\frac{1}{2}\sum_{jj'}\left[S_{j'}\frac{\sqrt{2S_j}}{2}\left[F_1^* a_j^\dagger + F_1 a_j\right] + S_j\frac{\sqrt{2S_{j'}}}{2}\left[F_2 a_{j'}^\dagger + F_2^* a_{j'}\right]\right] \tag{3.15}$$

where we defined $F_1 = F_J(j,j')_{xz} + iF_J(j,j')_{yz}$ and $F_2 = F_J(j,j')_{zx} - iF_J(j,j')_{zy}$, and equates to zero given the restrictions of asymmetry in the DM interaction. Finally, H_2 is the term that carries the spin-wave approximation, given by,

$$\begin{aligned} H_2 = \; & -\tfrac{1}{2}\textstyle\sum_{jj'}\Big\{-S_j F_J(j,j')_{zz} a_{j'}^\dagger a_{j'} - S_{j'} F_J(j,j')_{zz} a_j^\dagger a_j + \\ & + \tfrac{\sqrt{S_j S_{j'}}}{2}\left[G_1(j,j') a_j^\dagger a_{j'}^\dagger + G_2^*(j,j') a_j^\dagger a_{j'} + G_2(j,j') a_j a_{j'}^\dagger + G_1^*(j,j') a_j a_{j'}\right]\Big\} \end{aligned} \tag{3.16}$$

where we have defined the following short-hand notation, $G_1 = F_J(i,j)_{xx} - iF_J(i,j)_{xy} - iF_J(i,j)_{yx} - F_J(i,j)_{yy}$ and $G_2 = F_J(i,j)_{xx} + iF_J(i,j)_{xy} - iF_J(i,j)_{yx} + F_J(i,j)_{yy}$, for the terms of the projection matrix. Every subsequent term gives rise to multi-magnon interactions.

For simplicity, we truncate this series using the linear spin wave approximation, where only the $n = 2$ term is used,i.e. considering only terms that are quadratic in the operators such that $H_2 \propto a_j^\dagger a_{j'}$. This approximation is justified for temperatures well below the magnetic ordering temperature since it leads to removing interactions between magnons, and in cases where $S >> 1$, and it allows us to neglect higher-order terms in Eq. (3.12) [78].

Notice that so far we have the Hamiltonian in real space. To acquire the spin-wave spectrum would require the diagonalisation of a $N \times N$ matrix, with N being the number of sites, which can be of the order of Avogadro's number, making this approach unfeasible to be used to characterise any realistic system, in this form.

Next, we take the Fourier transform of the bosonic operators to exploit the

periodicity of the system and greatly simplify our problem. In the bulk case, the Fourier transform is applied in all three dimensions of the system. This approach is found in the literature. In contrast, in the case we are interested in, of thin films, only two dimensions are Fourier transformed,

$$\begin{aligned} a_{q_\parallel}^{(r)} &= \frac{1}{\sqrt{N_\parallel}} \sum_j^{(r)} e^{-i\mathbf{q}_\parallel \cdot \mathbf{R}_j} a_j \\ a_{q_\parallel}^{(r)\dagger} &= \frac{1}{\sqrt{N_\parallel}} \sum_j^{(r)} e^{i\mathbf{q}_\parallel \cdot \mathbf{R}_j} a_j^\dagger \\ a_i &= \frac{1}{\sqrt{N_\parallel}} \sum_{q_\parallel} e^{i\mathbf{q}_\parallel \cdot \mathbf{R}_j} a_{q_\parallel}^{(r)} \\ a_i^\dagger &= \frac{1}{\sqrt{N_\parallel}} \sum_{q_\parallel} e^{-i\mathbf{q}_\parallel \cdot \mathbf{R}_j} a_{q_\parallel}^{(r)\dagger} \end{aligned} \tag{3.17}$$

The wave vector $\mathbf{q}_\parallel$ is only defined in directions within the plane of the film, and the normalisation constant $N_\parallel$ is the number of magnetic moments in the system, where r labels the sites within the unit cell and $\mathbf{R}_j$ is the position vector of the j'th site. Just for comparison, in the bulk case, we only need to change in Eq. (3.17) such that $\mathbf{q}_\parallel \to \mathbf{q}$ and $N_\parallel \to N$.

Substituting Eq. (3.17) within Eq. (3.16) and using the following definition for the Kronecker delta,

$$\sum_i e^{i(\mathbf{q}-\mathbf{q}')\cdot\mathbf{R}_j} = N\delta_{\mathbf{q}\mathbf{q}'} \tag{3.18}$$

for $\mathbf{q}$, $\mathbf{q}'$ any two wavevectors, $\mathbf{R}_j$ a position vector for a site j in a system with N sites. The resulting Hamiltonian matrix is given by:

$$\begin{aligned} H_2 = \tfrac{1}{2}\sum_{q_\parallel}\sum_{rs}\sum_u z_u \Big\{ & \Big\{ S_r F_J(r,s)_{zz} a_{q_\parallel}^{(s)\dagger} a_{q_\parallel}^{(s)} + S_s F_J(r,s)_{zz} a_{q_\parallel}^{(r)\dagger} a_{q_\parallel}^{(r)} \\ -\tfrac{\sqrt{S_r S_s}}{2} & \Big[G_1(r,s)\Gamma_{rs}^{*(u)}(\mathbf{q}_\parallel) a_{q_\parallel}^{(r)\dagger} a_{-q_\parallel}^{(s)\dagger} + G_1^*(r,s)\Gamma_{rs}^{(u)}(\mathbf{q}_\parallel) a_{-q_\parallel}^{(r)} a_{q_\parallel}^{(s)} \\ + & G_2(r,s)\Gamma_{rs}^{(u)}(\mathbf{q}_\parallel) a_{q_\parallel}^{(r)\dagger} a_{q_\parallel}^{(s)} + G_2^*(r,s)\Gamma_{rs}^{*(u)}(\mathbf{q}_\parallel) a_{q_\parallel}^{(r)\dagger} a_{q_\parallel}^{(s)} \Big] \Big\} \Big\} \end{aligned} \tag{3.19}$$

Equation (3.19) is then symmetrised, so that the terms contribute equally to

all four quadrants of the resulting matrix [98]. This is achieved by duplicating every term, taking the Hermitian conjugate of the duplicate terms and dividing the overall result by two. The fact that the Hamiltonian is Hermitian allows us to take these steps without any change in the result. This is the so-called 'spread it around' trick, giving us,

$$
\begin{aligned}
H_2 = \tfrac{1}{4}\sum_{q_\parallel}\sum_{rs}\sum_{u} z_u \Big\{ & \Big\{ S_r F_J(r,s)_{zz} a^{(s)\dagger}_{q_\parallel} a^{(s)}_{q_\parallel} + S_s F_J(r,s)_{zz} a^{(r)\dagger}_{q_\parallel} a^{(r)}_{q_\parallel} \\
-\tfrac{\sqrt{S_r S_s}}{2} & \Big[G_1(r,s)\Gamma^{*(u)}_{rs}(\mathbf{q}_\parallel) a^{(r)\dagger}_{q_\parallel} a^{(s)\dagger}_{-q_\parallel} + G^*_1(r,s)\Gamma^{(u)}_{rs}(\mathbf{q}_\parallel) a^{(r)}_{-q_\parallel} a^{(s)}_{q_\parallel} \\
+ & G_2(r,s)\Gamma^{(u)}_{rs}(\mathbf{q}_\parallel) a^{(r)\dagger}_{q_\parallel} a^{(s)}_{q_\parallel} + G^*_2(r,s)\Gamma^{*(u)}_{rs}(\mathbf{q}_\parallel) a^{(r)\dagger}_{q} a^{(s)}_{q_\parallel} \Big] \Big\} \\
+ & \Big\{ S_r F_J(r,s)_{zz} a^{(s)}_{-q_\parallel} a^{(s)\dagger}_{-q_\parallel} + S_s F_J(r,s)_{zz} a^{(r)}_{-q_\parallel} a^{(r)\dagger}_{-q_\parallel} \\
-\tfrac{\sqrt{S_r S_s}}{2} & \Big[G^*_1(r,s)\Gamma^{*(u)}_{rs}(\mathbf{q}_\parallel) a^{(r)}_{-q_\parallel} a^{(s)}_{q_\parallel} + G_1(r,s)\Gamma^{(u)}_{rs}(\mathbf{q}_\parallel) a^{(r)\dagger}_{q_\parallel} a^{(s)\dagger}_{-q_\parallel} \\
+ & G^*_2(r,s)\Gamma^{(u)}_{rs}(\mathbf{q}_\parallel) a^{(r)}_{-q_\parallel} a^{(s)\dagger}_{-q_\parallel} + G_2(r,s)\Gamma^{*(u)}_{rs}(\mathbf{q}_\parallel) a^{(r)}_{-q_\parallel} a^{(s)\dagger}_{-q_\parallel} \Big] \Big\} \Big\}
\end{aligned}
\tag{3.20}
$$

where $\Gamma^{(u)}_{rs} = (1/z_u)\sum_{\mathbf{d}_u} e^{-i\mathbf{q}_\parallel\cdot\mathbf{d}_u}$ and $\mathbf{d}_u$ represents one of the z_u different distance vectors denoting the u'th nearest-neighbours, e.g. first, second, etc.. The labels r and s are used to distinguish between various magnetic moments within the unit cell. The magneto-crystalline term can also be rewritten using similar steps. Since every term in Eq. (3.20) has a pair of creation and annihilation operators, we can write it as a multiplication of a matrix with the numerical values of the system-dependent parameters $F_J(r,s)$ and $\Gamma^{(u)}_{rs}(\mathbf{q}_\parallel)$, with two vectors composed of the creation and annihilation operators.

Following the same procedure we did for the exchange term, we perform the second quantisation, keeping only the quadratic terms on the creation and annihilation operators, and Fourier transform to get for the magneto-crystalline anisotropy,

$$
\begin{aligned}
H_{K} = -\frac{K}{2}\sum_{q_{\parallel}}\sum_{r} S_r \left[A_{rx}^2 + A_{ry}^2 - 2A_{rz}^2\right]\left(a_{q_{\parallel}}^{(r)\dagger}a_{\vec{q}_{\parallel}}^{(r)} + a_{-q_{\parallel}}^{(r)}a_{-q_{\parallel}}^{(r)\dagger}\right) \\
+ S_r[A_{rx} + iA_{ry}]^2 a_{q_{\parallel}}^{(r)\dagger}a_{-q_{\parallel}}^{(r)\dagger} \\
+ S_r[A_{rx} - iA_{ry}]^2 a_{-q_{\parallel}}^{(r)}a_{q_{\parallel}}^{(r)}
\end{aligned}
\tag{3.21}
$$

while for the Zeeman term, we get,

$$
H_{B} = -2\mu_B \mathbf{B}\sum_{q_{\parallel}}\sum_{r} S_r A_{rz}\left(a_{q_{\parallel}}^{(r)\dagger}a_{q_{\parallel}}^{(r)} + a_{-q_{\parallel}}^{(r)}a_{-q_{\parallel}}^{(r)\dagger}\right) \tag{3.22}
$$

We can then write Eq. (3.20) in a compact form as follows:

$$
H_2 = \sum_{q_{\parallel}} v_{q_{\parallel}}^{\dagger}\cdot\mathbf{L}(\mathbf{q}_{\parallel})\cdot v_{q_{\parallel}} \tag{3.23}
$$

where we defined:

$$
v_{q_{\parallel}}^{\dagger} = (a_{q_{\parallel}}^{(1)\dagger},...,a_{q_{\parallel}}^{(M)\dagger}|a_{-q_{\parallel}}^{(1)},...,a_{-q_{\parallel}}^{(M)}) \tag{3.24}
$$

which has the commutation relation:

$$
\begin{aligned}
\left[v_{q_{\parallel}}, v_{q'_{\parallel}}^{\dagger}\right] &= \mathcal{N}\delta_{q_{\parallel},q'_{\parallel}} \\
[v_{q_{\parallel}}, v_{q'_{\parallel}}] = \left[v_{q_{\parallel}}^{\dagger}, v_{q'_{\parallel}}^{\dagger}\right] &= 0
\end{aligned}
\tag{3.25}
$$

where:

$$
\mathcal{N} = \begin{pmatrix} I & 0 \\ 0 & -I \end{pmatrix} \tag{3.26}
$$

with I being the identity matrix with rank half the length of $v_{q_{\parallel}}^{\dagger}$.

To diagonalise the Hamiltonian we will use the Bogoliubov transformation. Taking into account the commutation relations in Eq. (3.25) we obtain the equation of motion for v_q,

$$
i\frac{dv_{q_{\parallel}}}{dt} = -[H_2, v_{q_{\parallel}}] = \mathcal{L}(q_{\parallel})\cdot v_{q_{\parallel}} \tag{3.27}
$$

where $\mathcal{L}(q_{\parallel}) = L(q_{\parallel})\cdot N$ where we used $\hbar = 1$.

Assuming that the unit cell has M magnetic moments, the matrix $\mathcal{L}(\mathbf{q}_\parallel)$ will be 2M-dimensional, such that $\varepsilon_n(\mathbf{q}_\parallel) = \omega_n(\mathbf{q}_\parallel)/2 \geq 0$ for $n = 1, \cdots, M$ and $\varepsilon_n(\mathbf{q}_\parallel) = -\omega_n(\mathbf{q}_\parallel)/2 \leq 0$ for $n = M+1, \cdots, 2M$, with $\hbar = 1$ i.e. the eigenvalues of $\mathcal{L}$ are related to the eigenenergies of the magnon modes that are allowed in the system for each q. There will be M positive and M negative eigenvalues due to particle-hole symmetry.

We diagonalize $L(\mathbf{q}_\parallel)$ with the unitary transformation $L'(\mathbf{q}_\parallel) = UL(\mathbf{q}_\parallel)U^\dagger$, where $U^\dagger$ is a matrix which columns are the eigenvectors of $\mathcal{L}(\mathbf{q}_\parallel)$, this allow us to write:

$$H_2 = \sum_{q_\parallel} \vec{v}^\dagger_{q_\parallel} U^\dagger U \mathbf{L}(\mathbf{q}_\parallel) U^\dagger U \vec{v}_{q_\parallel} = \sum_{q_\parallel} w^\dagger_{q_\parallel} L'(\mathbf{q}_\parallel) w_{q_\parallel} \tag{3.28}$$

having defined $w^\dagger = \vec{v}^\dagger U^\dagger$ given by:

$$w^\dagger = (\alpha^{(1)\dagger}_{q_\parallel}, ..., \alpha^{(M)\dagger}_{q_\parallel} | \alpha^{(1)}_{-q_\parallel}, ..., \alpha^{(M)}_{-q_\parallel}) \tag{3.29}$$

Comparing with Eq. (3.24) we can define:

$$\alpha^{(r)\dagger}_{q_\parallel} = \sum_{n=1}^{N} \left(U^\dagger_{r,n} a^{(n)}_{q_\parallel} + U^\dagger_{r,n+N} a^{(n)\dagger}_{-q_\parallel} \right) \tag{3.30}$$

$$\alpha^{(r)\dagger}_{-q_\parallel} = \sum_{n=1}^{N} \left(U^\dagger_{r+N,n} a^{(n)}_{q_\parallel} + U^\dagger_{r+N,n+N} a^{(n)\dagger}_{-q_\parallel} \right) \tag{3.31}$$

while in real space we have:

$$a_j = \sum_{n=1}^{N} \left(U^\dagger_{j,n} \alpha_n + U^\dagger_{j,n+N} \alpha^\dagger_n \right) \tag{3.32}$$

$$a^\dagger_j = \sum_{n=1}^{N} \left(U^\dagger_{j+N,n} \alpha_n + U^\dagger_{j+N,n+N} \alpha^\dagger_n \right) \tag{3.33}$$

Expanding H_2 in the new diagonal basis with the eigenfrequencies obtained from the diagonalisation of $\mathcal{L}(\mathbf{q}_\parallel)$, H_2 can be written as,

$$H_2 = \sum_{n=1}^{M} \sum_{q_\parallel} \omega_n(q_\parallel) \left[\alpha^{(n)\dagger}_{q_\parallel} \alpha^{(n)}_{q_\parallel} + \frac{1}{2} \right] \tag{3.34}$$

This approach allows the calculation of observables such as the spin scattering function, magnetisation, etc., for both bulk or thin films, by projecting the second quantized spin operators onto the diagonalised basis of the Hamiltonian α_n and $\alpha_n^\dagger$, using Eqs. (3.32) and (3.33).

3.2 Spin Scattering function

The spin scattering function is a proxy for neutron scattering measurements also sometimes called the dynamic structure factor. It is given by the space and time Fourier transform of the time-dependent spin-spin correlation function:

$$\mathcal{S}_{\alpha\beta}(\mathbf{q},\omega) = \frac{1}{2\pi N}\sum_{j,j'}\int dt e^{-i\omega t} e^{-i\mathbf{q}\cdot(\mathbf{r}_j-\mathbf{r}_{j'})}\langle S_j^\alpha(0) S_{j'}^\beta(t)\rangle_T \tag{3.35}$$

Here we are noting N as the total number of spins in the lattice. Once more, we employ Latin letters to designate lattice sites, while Greek letters are utilised for denoting Cartesian directions. This way the spin operator s_j^α represents the α component of a spin located at position $\mathbf{r}_j$. The $\langle\cdot\rangle_T$ denotes the quantum and thermal average at temperature T.

In this section, we will connect the spin scattering function and the eigenvalues and eigenvectors of $\mathcal{L}$, which will give us the frequencies and their spectral weights for the magnons in the system, respectively.

Considering both the Holstein-Primakoff transformation in Eq. (3.10) under the linear spin-wave approximation, and the 'Küblers trick', we can summarise the bosonic transformation for the spin operators in real space, by expressing it as:

$$S_j^\alpha(t) = \sqrt{\frac{S}{2}}\left\{V_{j\alpha}^- a_j(t) + V_{j\alpha}^+ a_j^\dagger(t)\right\} \tag{3.36}$$

noting that $a_j(t) = e^{-i\omega_n t}a_j$, and with:

$$V_{j\alpha}^\pm = (\mathcal{R}_j)_{x\alpha} \pm i(\mathcal{R}_j)_{y\alpha} \tag{3.37}$$

Substituting Eqs. (3.36), (3.32) and (3.33), in the scattering function in Eq. (3.35) and noting that $\langle\alpha_n^\dagger\alpha_{n'}^\dagger\rangle_T = \langle\alpha_n\alpha_{n'}\rangle_T = 0$ and $\langle\alpha_n^\dagger\alpha_{n'}\rangle_T = n_B(\omega_n)\delta_{nn'}$,

where n_B is the Bose-Einstein distribution. We perform the Fourier transform in the scattering function and focus only on the positive energies of the spectrum, we get,

$$\mathcal{S}_{\alpha\beta}(\mathbf{q},\omega) = \frac{1}{2N_{\parallel}} \sum_{n=1}^{M} \sum_{r,s} \frac{\sqrt{S_r S_s}}{2} e^{-i\mathbf{q}_{\perp}\cdot(\mathbf{r}_r - \mathbf{r}_s)} \left(W_r^{(n)}\right)_{\alpha} \left(W_s^{(n)}\right)_{\beta} [1+n_B]\delta(\omega-\omega_n) \tag{3.38}$$

where we have defined $\mathbf{q}_{\perp}$ which comes from the decomposition of the magnons' wavevector $\mathbf{q} = (\mathbf{q}_{\perp}, q_{\parallel})$, in the directions perpendicular and the parallel direction with respect to the film orientation, and,

$$\left(W_r^{(n)}\right)_{\alpha} = \left(V_{r,\alpha}^{-} U_{r,n}^{\dagger} + V_{r,\alpha}^{+} U_{r+N,n}^{\dagger}\right) \tag{3.39}$$

$$\left(W_s^{(n)}\right)_{\beta} = \left(V_{s,\beta}^{-} U_{s,n+N}^{\dagger} + V_{s,\beta}^{+} U_{s+N,n+N}^{\dagger}\right) \tag{3.40}$$

To account for finite instrument resolution we replace the $\delta(\omega-\omega_n)$ by a Gaussian broadening given by:

$$\delta(\omega-\omega_n) = \frac{1}{\sqrt{2\pi\Delta^2}} e^{-\frac{(\omega-\omega_n)^2}{2\Delta^2}} \tag{3.41}$$

It is important to emphasise that with this method we can evaluate thin films and heterostructures, and also use the parameters such as J_{ij} and anisotropies K for each different layer and between different layers, as required by the physics of the system.

For colinear spins, the calculation of $\mathcal{S}_{\alpha\beta}$, where α and β are the Cartesian directions x, y and z, aligned with the z-axis, for cubic unit cells, we have, $\mathcal{S}_{xx}(q,\omega) = \mathcal{S}_{yy}(q,\omega) \neq 0$ while $\mathcal{S}_{\alpha\beta}(q,\omega) = \mathcal{S}_{zz}(q,\omega) = 0$ for $\alpha \neq \beta$.

The spin scattering function gives a relative measurement of the amount the magnetic moment changes in a particular direction, *i.e.*, if all magnetic moments in the system are pointing in the z-direction and start to precess, only the magnetic moment projections in the x and y-directions change, which leads to a non-zero value for the $\mathcal{S}_{xx}(q,\omega)$ and $\mathcal{S}_{yy}(q,\omega)$ and zero value for $\mathcal{S}_{zz}(q,\omega)$, assuming the spin-wave approximation.

3.3 Magnon density of states

To compute the magnon density of states (DOS), we employ a methodology akin to that utilised in the derivation linking the velocity correlation function to the vibrational density of states for phonons [99,100]. Analogously, we extend this approach to the spin-spin correlation function. Employing the Holstein-Primakoff transformation, and the change of basis given in Eqs. (3.36), (3.32) and (3.33) in the time-dependent form $\alpha_n(t) = \alpha_n e^{-i\omega_n t}$ were ω_n are the eigenfrequencies of the magnons in the system, we can derive a formula for the density of states given by:

$$\rho(\omega) \propto \sum_{n=1}^{M} \sum_{q} \sum_{r,s} e^{-i\mathbf{q}_\perp \cdot (\mathbf{r}_r - \mathbf{r}_s)} \left(W_r^{(n)}\right)_\alpha \left(W_s^{(n)}\right)_\alpha \delta(\omega - \omega_n(q)) \tag{3.42}$$

where we used Einstein's summation convention for the Cartesian orientations labelled by α and the constants in front were omitted. This approach ensures uniformity in the DOS, irrespective of the number of magnetic moments within the unit cell representing the system. Each magnetic moment in the unit cell contributes to a distinct mode in the magnon dispersion, with no guarantee of degeneracy. By deriving the DOS through the spin-spin correlation function, distinct weights are assigned to each mode, with a preference for those associated with the primitive cell. This weighting scheme ensures a consistent solution, rendering the final DOS independent of the chosen unit cell for calculation purposes.

Following these definitions, we will provide examples to show the physics that is captured by the method outlined above. We will go over three different cases of thin films, ferromagnetic bcc Fe (100), antiferromagnetic NiO for two different thin film orientations (100) and NiO(111) and YIG as a ferrimagnetic example. We will evaluate numerically the spin scattering function using Eq. (3.38), and the magnon DOS using Eq. (3.42) by calculating the contribution to the spin scattering function of all modes in a grid in reciprocal space, as well as the individual modes contributions.

3.4 bcc Fe

We start with the prototype ferromagnetic material *bcc* Fe, a well-known and broadly studied system [101–104].

The calculations performed in this section have used the J_{ij} parameters proposed in [101], where 25 nearest neighbours are taken into account, and the magnetic moment of $2.26\mu_b$ was used as given in [105].

The calculation of the spin Hamiltonian depends on the number of magnetic moments in the unit cell. For each magnetic moment in the unit cell, there will be a resulting mode in the calculated magnon dispersion. In the case of bcc Fe, the primitive unit cell has only one atom in the unit cell, on the other hand, the conventional cell is comprised of two atoms in the unit cell. Independent of the choice of unit cell the active modes in the spin-scattering function will result in the magnon dispersion of the primitive unit cell.

In Fig. 3.1 we can see that, as described before, we have 2M modes, with M the number of magnetic moments in the unit cell, with M positive eigenvalues and M negative eigenvalues. The conventional cell has two magnetic moments and presents four modes. The spin-scattering function selects the active modes at each momentum, effectively unfolding the unit cell back to the primitive unit cell. This can be seen in the Figs. 3.1(b) and 3.1(d), where, irrespective of the choice of the unit cell, provided that the path is taken in the respective Brillouin zones.

Having that in mind, we can compare a thin film dispersion with its periodic counterpart. In Fig. 3.2 we show the $\mathcal{S}_{xx}$ for 300K, for a thin film of bcc Fe in (001) orientation. In other words, the sample is assumed to be infinite in the (x, y) plane, and confined to a limited number of monolayers in the z direction. As bcc Fe is a cubic system, $\mathcal{S}_{xx}$ is the same as $\mathcal{S}_{yy}$. The spin scattering functions are evaluated for a thin film of 20 monolayers. In addition, we show the bulk magnon dispersion, calculated using our formulation but for an infinite model in 3D, using a periodic version of the 20 monolayers unit cell. The effect of confinement is clearly observed by the granularity in the spin scattering function plot arising from quasi-momentum quantisation resulting

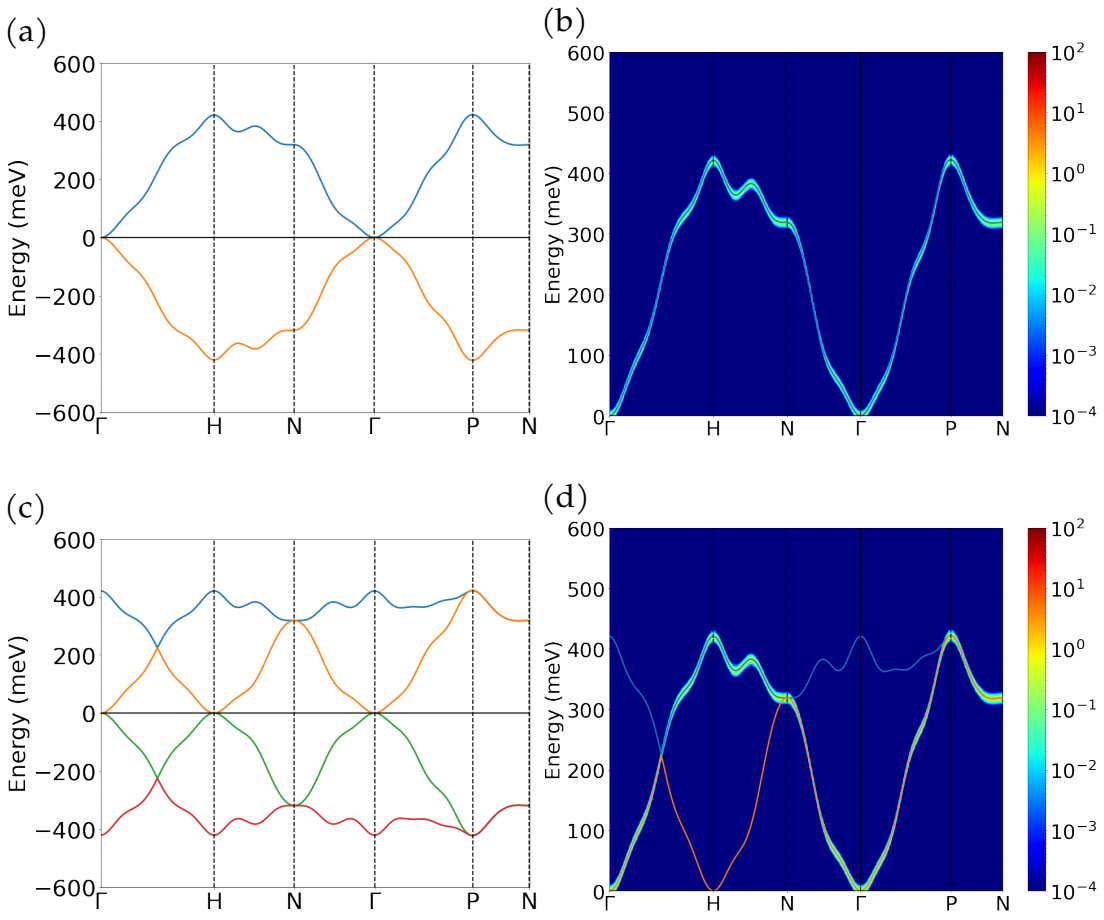

Figure 3.1: Magnon modes for bcc Fe, for the primitive and conventional unit cells, and their respective spin-scattering function calculations. (a) Magnon modes for primitive cell, (b) its respective spin scattering function, (c) Magnon modes for conventional cell, (d) its respective spin scattering function.

from the finite nature of this direction, as shown along the path traversing the finite z-direction ($\Gamma - P - N$). We observe that, since the trajectory deviates from the k_z direction, which is the direction of confinement in our thin film geometry, the quantisation does not yield symmetrical shapes for the granular features. Instead, the resulting features exhibit distinct shapes attributable to the trajectories in reciprocal space that are non-parallel to the finite direction. We overlay the respective eigenmodes and notice that in the thin film version, the eigenmodes in the path between $P - N$ are independent of the momentum, the dependence comes from the phase factor in the spin-scattering function calculation that selects the active mode.

In Fig. 3.3, as we increase the number of monolayers, these granular fea-

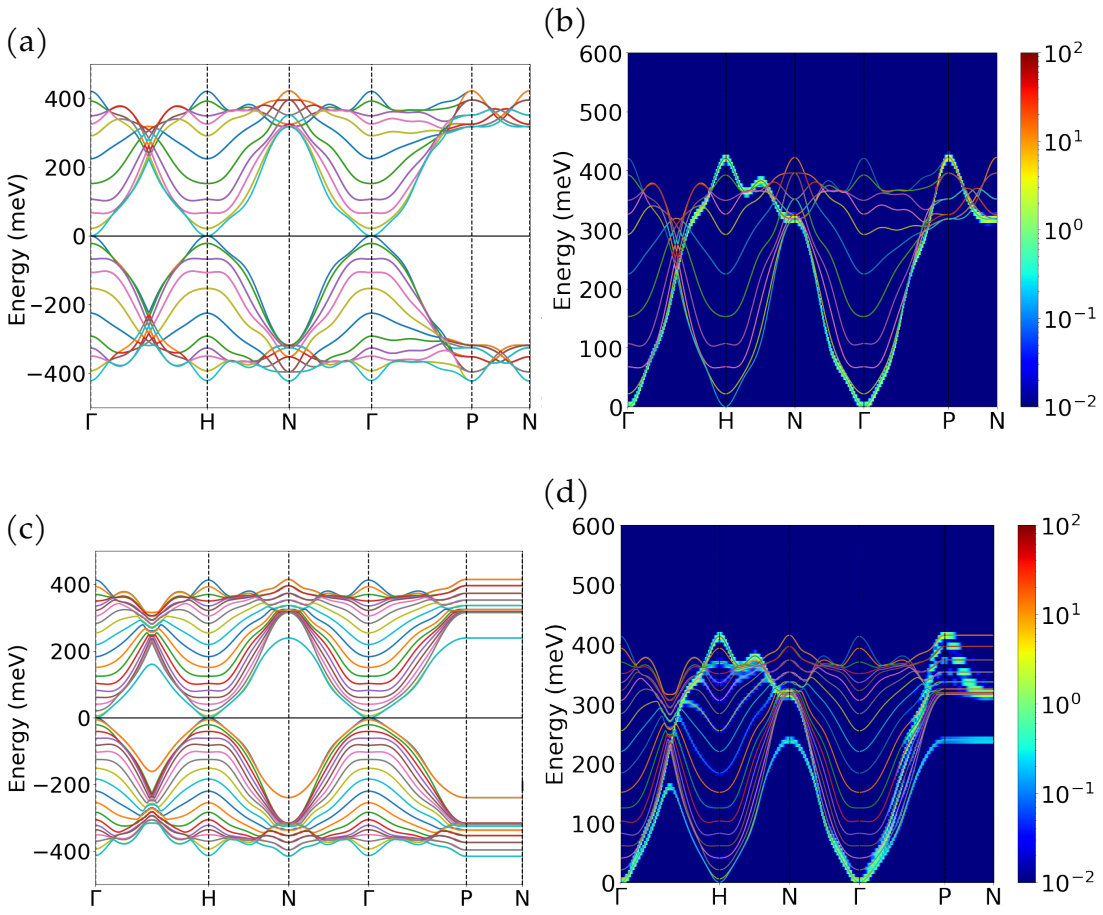

Figure 3.2: Eigenmodes for (a) periodic boundary, (b) 20 monolayers thin-film of Fe. We also present the Spin-scattering function overlayed with the respective eigenmodes, for 20 monolayers of Fe. (c) periodic boundary, (b) thin-film.

tures become increasingly densely packed, ultimately converging towards a continuous line in the limit of a bulk solid. The thin film calculations therefore tend towards the bulk when the system size increases, as expected in the limit of a large number of monolayers. We note that the calculated bulk spin scattering function using our approach agrees well with previous calculations of the magnon dispersion diagram and accompanying experiments for bulk *bcc* Fe [101, 103]. In particular, our results appear to capture the onset of the Kohn anomalies in the path between $\Gamma - H$ and between $H - N$, albeit less prominently than in references [101, 103], which can be explained due to the fact that we have employed parameters representing next nearest neighbours up to a distance of 5 times the lattice constant a, whereas prior research had considered parameters extending up to $7a$ as discussed in [101, 103].

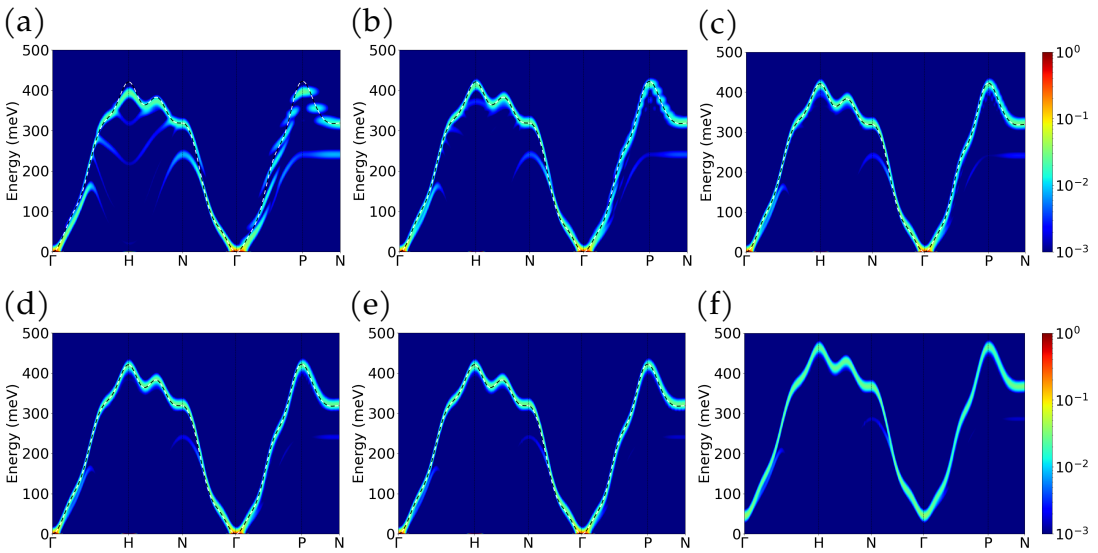

Figure 3.3: Spin scattering function of bcc Fe thin films with (a)10, (b)20, (c)30, (d)40, (e)50 monolayers (f) 50 monolayers with an added 20 meV of anisotropy in the crystallographic direction of confinement (100), with 25 nearest neighbours and a temperature of 300K was used for all calculations. For comparison, the bulk dispersion is shown as a black/white line. A broadening of Δ=6.5meV was used.

The treatment of the Heisenberg Hamiltonian as presented in the methods captures the fact that the top and bottom layers (*i.e.*, the surfaces) have fewer neighbours than bulk-like layers, resulting in a reduction of interactions, which leads to the appearance of softer modes that are less intense and decrease in intensity as the system increases in size, see Fig. 3.3. Furthermore, in Fig. 3.3(f) we show that the addition of $K = 20$ meV of magneto-crystaline anisotropy in the direction of the magnetic moments in the 50 monolayers case, results in a rigid shift in energy for all the modes to higher energies, the same but with a lesser intense effect happens for an applied magnetic field.

The existence of the additional softer surface-related modes can be clearly seen in the magnon DOS calculated using Eq. (3.42), as shown in Fig. 3.4, for a thin film of 10 monolayers. As highlighted by a blue arrow we can see the appearance of a peak around 180 meV, which is not present in the bulk DOS.

This surface-related peak in the DOS is dependent on the surface properties. This is illustrated in Fig. 3.5, where on the top and bottom surfaces of the 10 monolayer Fe film we added an artificial surface-only anisotropy (K_{surf}). As K_{surf} increases, the confined DOS peak shifts to higher energies, and eventually becomes localised at energies above the bulk dispersion.

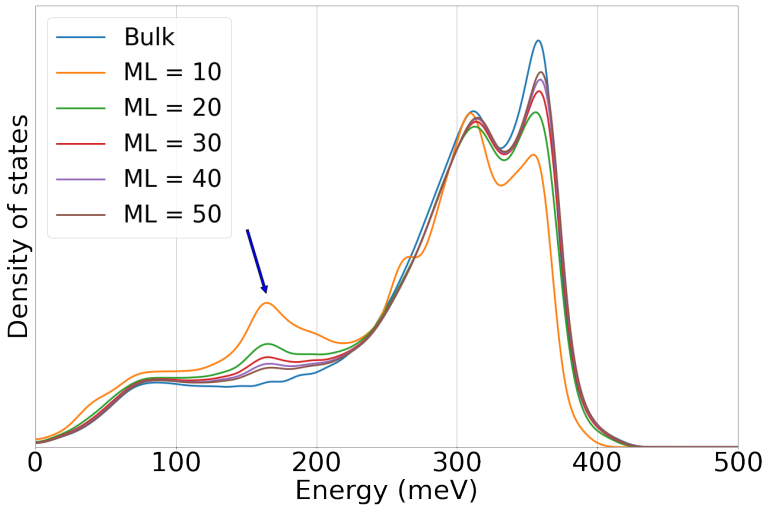

Figure 3.4: Density of states of Fe bcc comparing Bulk with varying sizes of thin films with 25 nearest neighbours and a temperature of 300K. Broadening used was Δ=6.5meV.

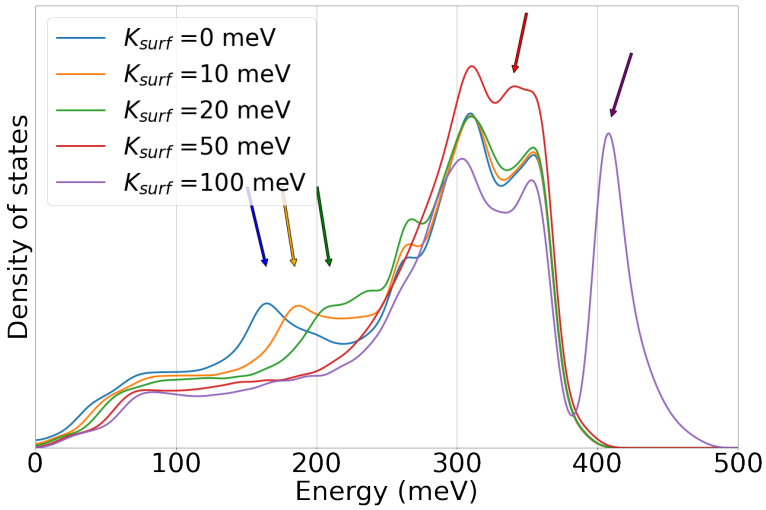

Figure 3.5: Density of states of bcc Fe thin film with size 10 monolayers, for varying intensities of K_{surf} with 25 nearest neighbours and a temperature of 300K. Broadening used was Δ=6.5meV.

3.5 NiO(100) and NiO(111)

Next, we consider NiO to demonstrate the applicability of our method to antiferromagnetic thin films. The flexible ability to set the magnetic moments modulus and directions inside the unit cell allows us to study, both colinear and non-colinear systems and their interfaces.

We used parameters from inelastic neutron scattering experiments that sug-

gest that the first-neighbour ferromagnetic exchange interaction parameters are $J_{1,p} = 1.39$ meV and $J_{1,ap} = 1.35$ meV, where $J_{1,p}$ is the interaction between parallel first neighbours and $J_{1,ap}$ is the interaction between anti-parallel first neighbours [106, 107]. Similarly, the second-neighbour antiferromagnetic exchange interaction was determined to be $J_2 = -19.01$ meV. The small difference between $J_{1,p}$ and $J_{1,ap}$ was attributed to lattice distortion, as previously pointed out [106, 107]. The magnetic moment of Ni^{2+} used is $1.4\mu_B$ [108].

Figure 3.6 shows the spin scattering function calculated for NiO(100) with 5, 10, 15, 20 and 30 monolayers, alongside the bulk NiO case, again represented by the black/white line.

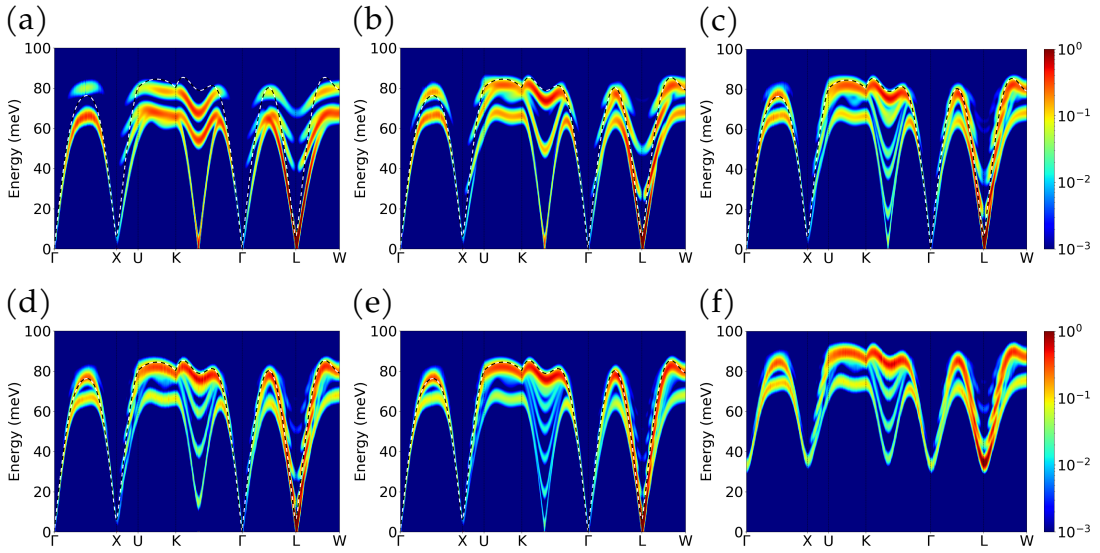

Figure 3.6: Spin scattering function of NiO (100) thin films with (a) 5, (b) 10, (c) 15, (d) 20, (e) 30 monolayers. (f) 20 Monolayers with an added 5 meV of anisotropy in the direction of the Néel vector which is set to be in the crystallographic direction of confinement, and a temperature of 300K.A broadening of Δ=0.5meV was used.

As expected and similar to bbc Fe, we confirm the tendency to match the bulk case in our calculations as the number of monolayers is increased. A softer energy mode related to the reduced interaction of the magnetic moments at the surfaces also appears for the thin film cases.

In Fig. 3.6(f) we show that adding $K = 5$ meV of magnetocrystalline anisotropy in the direction of the magnetic moments in the 20 monolayers case results in a shift in energy for all the modes to higher energies. In contrast to the bcc Fe case, this change is not rigid: the lower energies of the modes are more affected

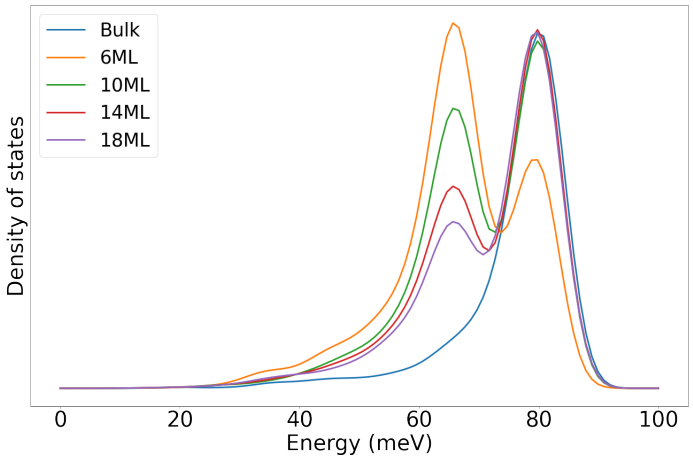

Figure 3.7: Density of states of NiO (100) comparing Bulk with varying sizes of thin films with a temperature of 300K.

than the higher ones.

As with Fe, the magnon DOS of NiO(100) was calculated and is shown in Fig. 3.7. The calculation confirms the appearance of the confined modes and their relation to the bulk case. The general tendency is again of a very pronounced confinement-related peak that continuously decreases with the increase of the thin film's size and eventually merges with the bulk-like peaks. We note that in the presented range of DOS calculations, only in ultra-thin films, below 10 ML, are the confined modes comparable to or larger than their bulk-like counterparts.

The effect of crystallographic direction on confinement is illustrated by a set of complementary calculations carried out on NiO(111) thin films. Figure 3.8 shows the spin scattering function of NiO(111) for 10, 20, 30, 40 and 50 monolayers, alongside the bulk spin scattering function. We also have included the effect of anisotropy in the case of a film of 30 ML with an added anisotropy of 10 meV in the same direction as the Néel vector.

We also note that the granularity in the spin-scattering function due to quasi-momentum quantisation, appears in different regions compared to the NiO(100) case, for the chosen path in the Brillouin zone reflecting the crystallographic direction of the confinement. The softer partial interaction mode also appears at lower energies than in NiO(100), with a flatter dispersion. This effect becomes even more apparent when we add an anisotropy in the direction of the Néel

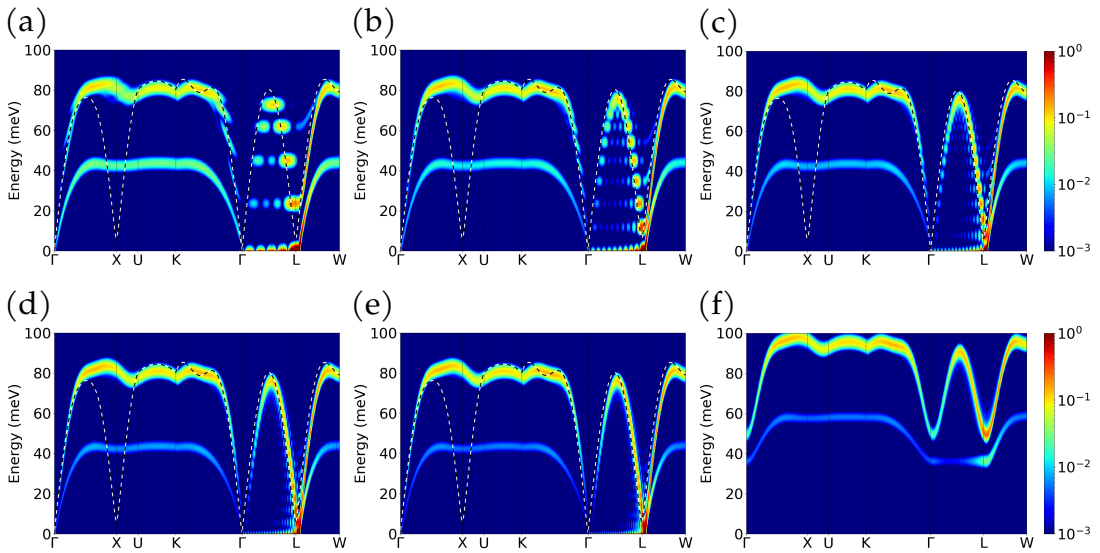

Figure 3.8: Spin scattering function of NiO (111) thin films with (a)10, (b)20, (c)30, (d)40, (e)50 monolayers (f) 50 monolayers with an added 10 meV of anisotropy in the direction of the Néel vector, and a temperature of 300K. Broadening used was Δ=0.5meV.

vector. A K=10 meV anisotropy leads to the hardening of all modes and a separation between the bulk mode and a confined mode at lower energies, and we observe a flat dispersion across the $\Gamma - L$ path corresponding to the out-of-plane direction, which can therefore be interpreted as a surface-confined mode.

We note also the stark difference between (100) and (111) oriented films in the $\Gamma - X$ direction. While we see a strong dip in the dispersion in the bulk and the (100) films, in the (111) films this dip is not present, showing that the direction of confinement can drastically change some of the features of the inelastic response.

Finally, a comparison of the calculated DOS for NiO(111) for different film thicknesses is given in Fig. 3.9. We once more observe the same tendency as in the NiO(100) films, where the magnon DOS peaks due to the surface-related modes are reduced in intensity and merge into the main bulk-like response for (111) films above 10 ML. The main difference with Ni(100) appears in the energy position (42 meV *vs.* 65 meV) of the surface-related peak which is due to the direction of confinement.

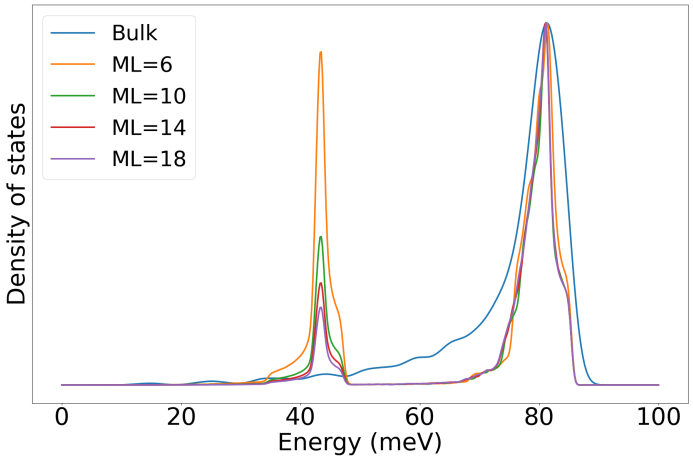

Figure 3.9: Density of states of NiO (111) comparing Bulk with varying sizes of thin films with a temperature of 300K.

3.5.1 Magnons velocity in NiO thin films

As discussed previously, there are many challenges towards the realisation of competitive spin-wave-based computing paradigms. Among them, the magnon velocity makes prohibitive interconnection by magnon propagation, since it is much slower than electrical signals in metallic conductors, adding considerable overhead due to signal delay. Typical delays are about 1 ns/μm (μs/mm), which can lead to latency that supersedes the typical clock cycle of a high-performance CMOS logic processor of about 300ps ($\sim$3 GHz clock frequency) [24].

To this goal, different materials have been studied to overcome this barrier, antiferromagnets and ferrimagnets attract a great deal of attention due to their THz dynamics, arising from their strong exchange interaction. Among them, YIG films drew substantial focus [109, 110] due to their low damping, high magnon lifetime and group velocity, which has been reported to be 42 km/s [111–118]. Recently high magnon velocities have been reported for NiO(111) nm films, realised by time-domain measurement on nanometre-sized samples, ranging between 100 km/s and 640 km/s [119], significantly higher than previously reported speeds in bulk NiO of 40 km/s [107], which were estimated indirectly on millimetre-size films of NiO, through magnon dispersion with inelastic-neutron scattering.

The original argument for this super-luminal velocity (relative to the magnons), given by the authors is the presence of small non-zero Gilbert damping in these samples, corroborated by bulk calculations of the group velocity by inserting a spin-wave ansatz in the Landau-Lifshitz-Gilbert equation, which suggests an exponential increase of the magnon velocity for long wavelengths with the reduction of the Gilbert damping, provided it is not taken to be zero.

This hypothesis was further studied [120] by evaluating the NiO magnon dispersion employing atomistic spin dynamics (ASD), for varying Gilbert damping constants. They concluded that the magnon velocity is nearly independent of the Gilbert damping in NiO, reporting a decrease in the magnon velocity with increasing damping, contradicting the previously proposed super-luminal increase with its reduction, and having a maximum velocity when the damping is set to zero. Given that the presence of damping allows dissipation of energy it is a classically expected result.

Our present approach doesn't allow the presence of damping. The previously discussed studies have primarily examined the effect of damping on the magnon velocity in bulk systems. In contrast, our investigation focuses on understanding how spatial confinement affects magnon dispersion and, consequently, their velocities.

In the reported setup [119], the magnon velocity is measured by comparing the signal delay between the optically driven generation of a spin current in a ferromagnetic layer (FM), and the subsequently detected signal in a normal metal layer (NM) via inverse spin-hall effect, which are separated by an antiferromagnetic (AFM) buffer layer of NiO(111). To account for the added latency due to the generation and detection of the magnon signal, the delay measured in the FM/AFM/NM device is reduced by the delay measured in an equivalent, bufferless, FM/NM device, distinguishing the time spent in the propagation through the NiO(111) buffer.

To model this device, in our calculations, we define a NiO unit cell with the [111] direction aligned along the z-axis of the unit cell, which we define as the finite direction of the film. This leads to the $\Gamma - L$ direction to be the one quantized by the confinement, as seen in Fig. 3.10, where we also show the structure

used, comparing the conventional (100) cell and the one we used to simulate the (111) slab. In the (111) direction the planes are stacked antiferromagnetically on a face-centered cubic lattice. The exchange parameters used are the same as the ones employed before in section 3.5.

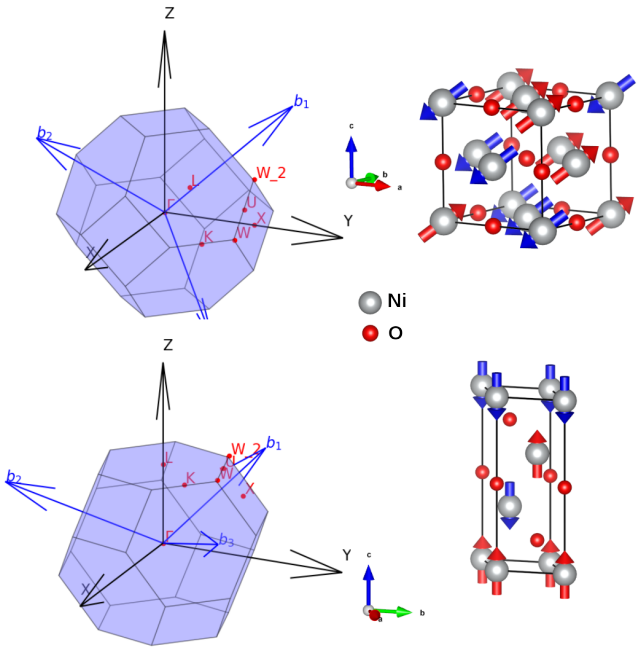

Figure 3.10: First Brillouin zone of NiO in the primitive lattice showing the L direction in the 111 direction.

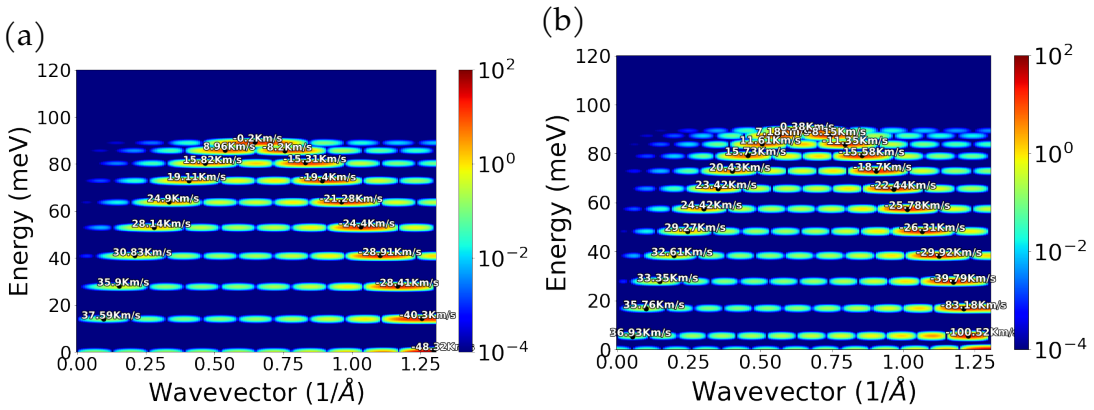

Figure 3.11: Spin Scattering function following the magnon dispersion of NiO(111) thin film, for 20 monolayers and 25 monolayers in the $\Gamma - L$ direction, annotated we show the correspondent group velocity.

By calculating the spin-spin scattering function for this direction we can see a clear quantisation in quasi-momenta and energy due to the confinement

effects in Fig. 3.11, where we also note the phase velocity of each quantised peak.

Due to the quantisation in this direction, we have discrete peaks for the magnon dispersion, to calculate the group velocity normally given by the gradient of the dispersion $\mathbf{v}_g = \nabla_{\mathbf{k}}\omega$, with respect to the magnons' wavevector, we evaluate the local slopes between adjacent peaks following the dispersion curve. We also evaluate the phase velocity, given by $\mathbf{v}_p = \mathbf{k}\omega/||\mathbf{k}||^2$, which is evaluated for each individual peak in the spin-spin scattering function.

To achieve this goal we used the peak finding algorithm code [121], as illustrated in Fig. 3.11 for the 20ML and 25ML cases. One point to note is that NiO(111) for an odd number of layers, there is an uncompensated number of magnetic moments. Conversely, the magnetic moments are compensated for an even number of layers. This difference is reflected in the dispersions given in Fig. 3.11 where we can see that the compensated case, has a clear parabolic dispersion, while the uncompensated has a low energy mode that skews the parabolic shape at the Brillouin zone edge, close to 1.25 $(1/\mathring{A})$. Due to the steeper interpolated gradient, this leads to a higher group velocity. This effect is diminished as the number of monolayers increases because the ratio of up and down magnetic moments tends to unity as the number of layers is increased.

A complete picture is given in Fig. 3.12, where we present the interpolated dispersion relation, the group and phase velocities. Both the interpolated dispersion and the phase velocity show a clear tendency to converge to bulk values. As the number of monolayers is increased, longer wavelengths are available, allowing for higher phase velocities until a plateau. In addition, the group velocity shows a higher velocity for the case of an odd number of layers due to the previously discussed differences between the even and odd number of layers.

From this data, we can conclude that the reported high velocities can't be explained by the quantisation of energy and momenta in thin films. Although the effect is reported to be thickness-dependent, even the higher group velocities in uncompensated films can't account for the experimental values, since the films used in the measurements range from 15nm to 50nm which for NiO(111)

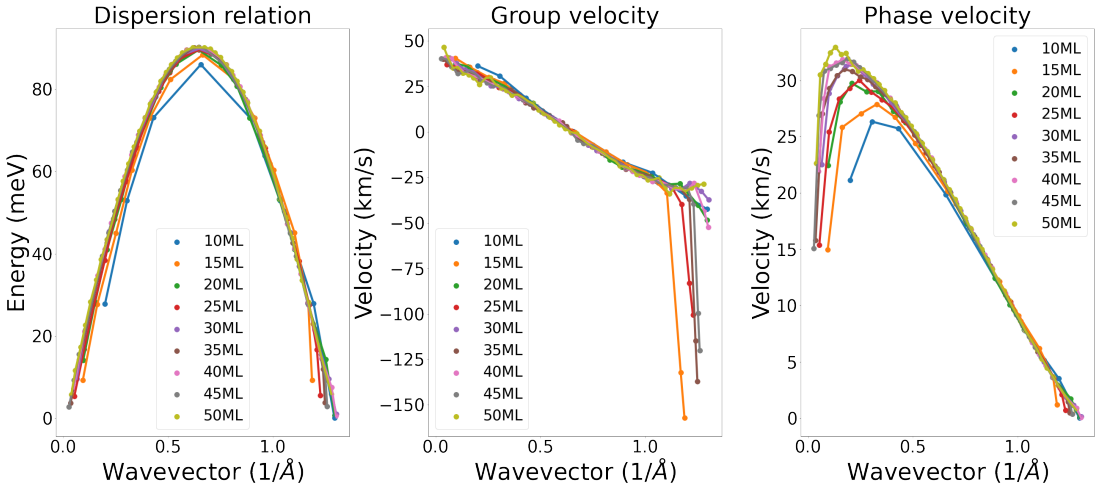

Figure 3.12: Spin Scattering function following the magnon dispersion of NiO(111) thin film, for 20 monolayers in the $\Gamma - L$ direction, annotated we show the correspondent group velocity.

correspond to approximately a range of 60-200 monolayers, a range where we expect that the uncompensated layer will be irrelevant.

The current theoretical exploration is far from exhausted, long-range interactions such as dipolar interactions can play a role in the film thickness dependence, particularly since we expect higher magnon velocities close to the Γ point, a region that is mainly affected by the dipolar interaction [39]. In addition, the calculations we performed, have not taken into account, interfacial effects or surface reconstructions, which can lead to changes in the dispersion relation of magnons, although unlikely to account for the super-luminal velocities reported.

3.6 YIG

As a last example of the method's applicability, we will study the ferrimagnetic material YIG, which has attracted a great deal of attention due to its Thz magnons capability and high free-path length [111–118].

For the calculation of the underlying magnon dispersion, we will use the exchange parameters proposed from fitting inelastic neutron scattering [47].

Note that, for the third nearest neighbours, there are two possibilities of exchange parameters J_{3a} and J_{3b} Fig. 3.13. These two exchange paths are dissim-

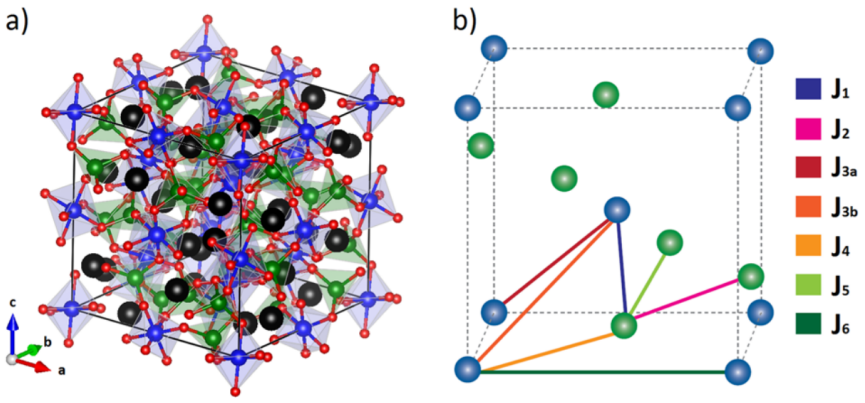

Figure 3.13: Crystal structure and magnetic exchange paths in Yttrium Iron Garnet (YIG). The conventional unit cell of YIG is represented, with the majority of tetrahedral sites marked in green and the minority of octahedral sites in blue. Yttrium is depicted as black spheres and oxygen as red spheres. The first octant of the YIG unit cell is shown, highlighting the two distinct Fe^{3+} sites: tetrahedral sites in green and octahedral sites in blue [47].

ilar and can be distinguished due to the symmetry of the crystal when rotated about the bond vector. The J_{3a} exchange path exhibits a 2-fold symmetry, while the J_{3b} exchange path obey the higher D3 symmetry point group Fig. ??.

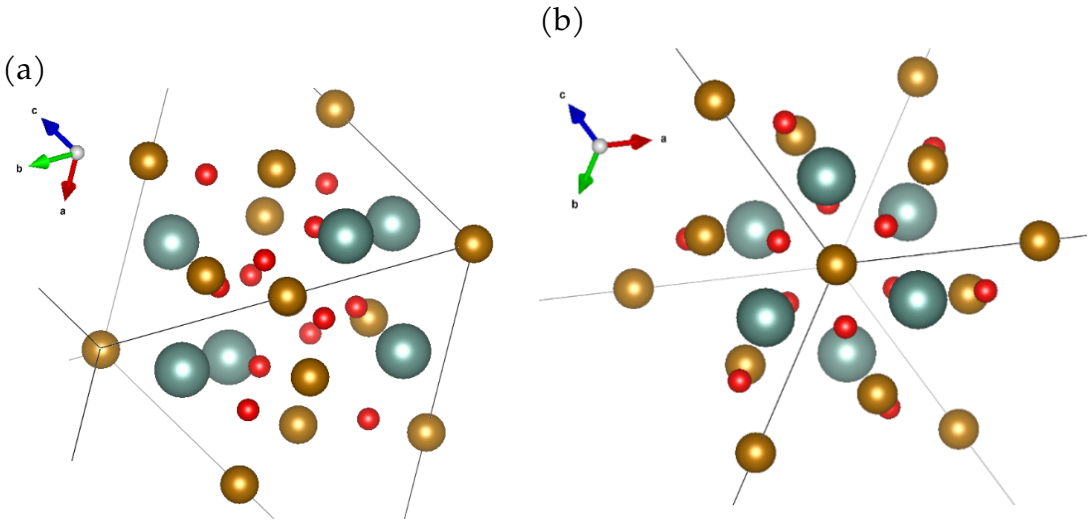

Figure 3.14: The left image depicts the projection of the crystal structure along the J_{3a} bond, while the figure to the right depicts the projection of the crystal structure along the J_{3b} bond, which shows a 2-fold bond and a D3 point group, respectively. These images were extracted from the supplementary material of [47].

In the case of YIG, the high number of magnetic moments in the unit cell, leads to a magnon dispersion heavily populated with different modes, charac-

terised by a group of lower energy modes and another group of higher energy ones. Not all modes are active in scattering experiments, this is reflected in the bulk spin-scattering function as presented in Fig. 3.15. We can see the existence of two main active modes, one that has zero energy at the Γ point, which borrowing from the language used with phonons, can be seen as an acoustic-like mode. At higher energies, we see an optical-like mode. Here, we will be calculating the spin scattering function disregarding the temperature dependence, to highlight the high energy modes, which, are much lower in intensity once the Bose-Einstein distribution is taken into account.

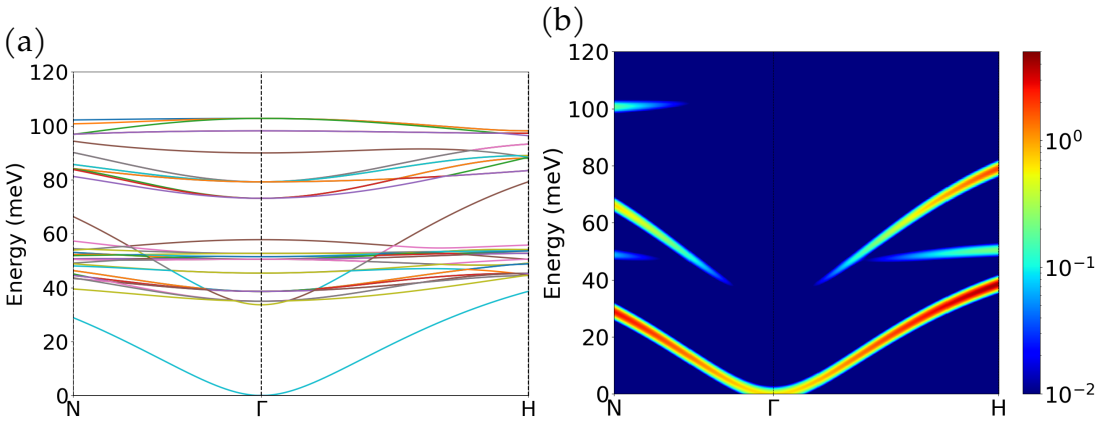

Figure 3.15: (a) Magnon dispersion of bulk YIG, (b) respective spin-scattering function.

In the thin film case for YIG, we have four different termination cases as shown in Fig. 3.16.

The first one is presented in Fig. 3.17, we can see the presence of a softer mode in both $\Gamma - H$ and $\Gamma - N$ directions, this is not present in Fig. 3.18. Depending on the termination of the top and bottom layer we have different active magnon modes. These differences are mitigated as the film thickness is increased, as in all other cases the spin-scattering function tends to the bulk solution.

These differences are more visible in the DOS plots in Fig. 3.21. In cases Figs. 3.21(a) and 3.21(c) have a pair of peaks around 25meV, which are not present in the Figs. 3.21(b) and 3.21(d). The difference between these two cases is the number of minority octahedral and majority tetrahedral sites. In cases where

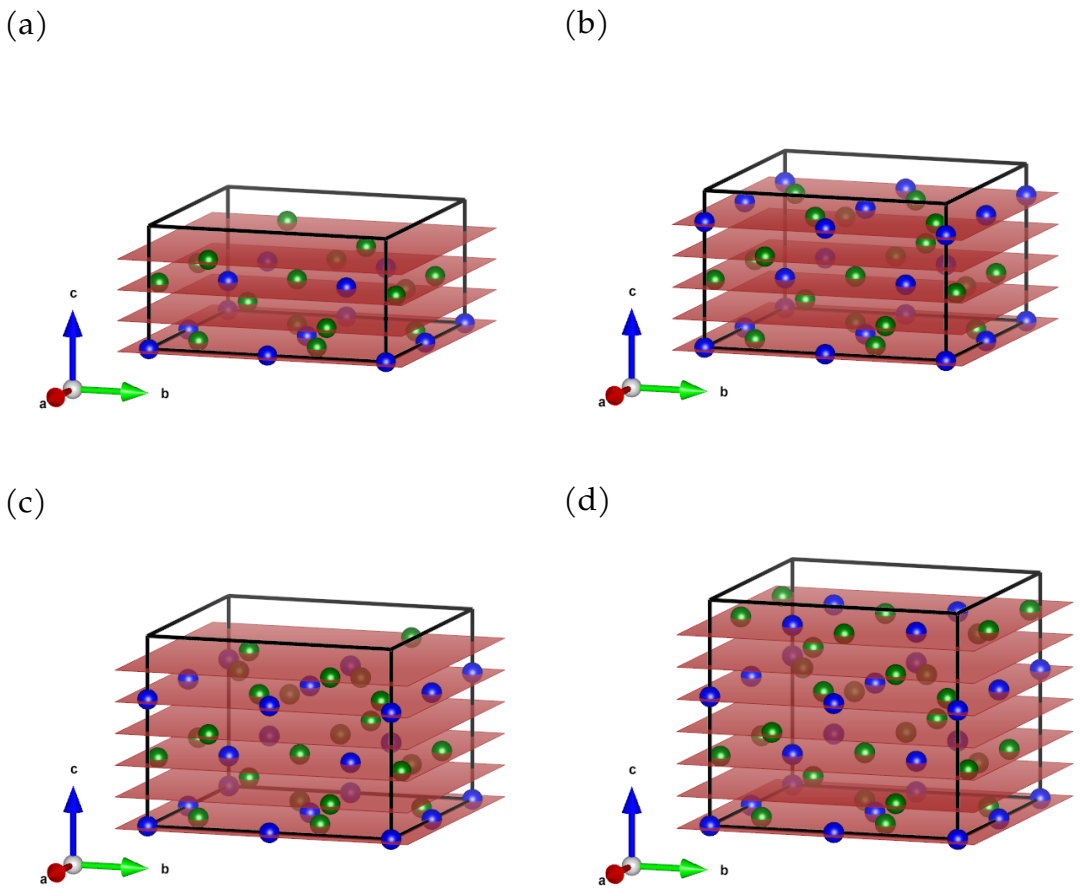

Figure 3.16: Depiction of the different termination of YIG thin films, the blue spheres represent Fe atoms with magnetic moments in majority up orientation and the green ones represent minority down magnetic moments.

the 25meV peaks appear, the ratio between the tetrahedral and octahedral sites is below the bulk ratio of $3/2$, while the cases where the peaks do not appear have the same ratio as the bulk.

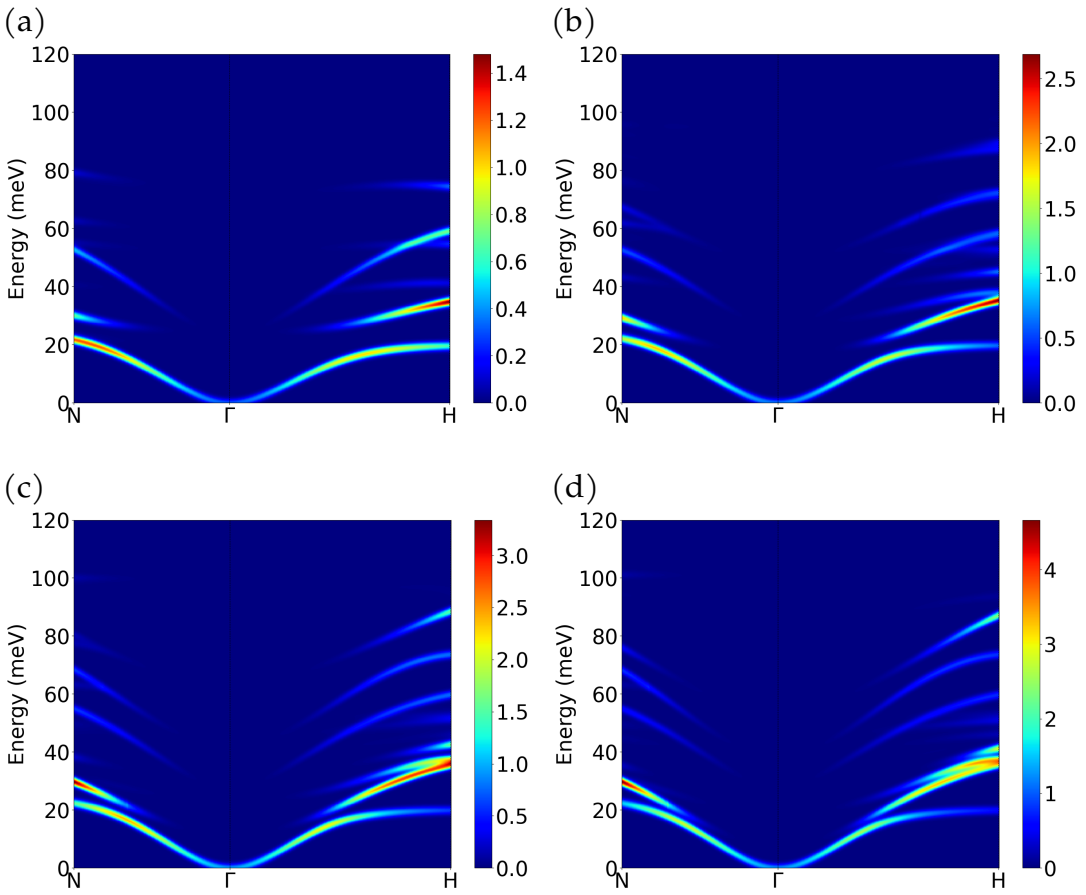

Figure 3.17: Spin scattering function for YIG thin films in the (100) direction. Each image with an increasing number of layers from (a) 4 monolayers, (b) 8 monolayers, (c) 12 monolayers, (d) 16 monolayers. These cases share the same termination, the case given in Fig. 3.16(a).

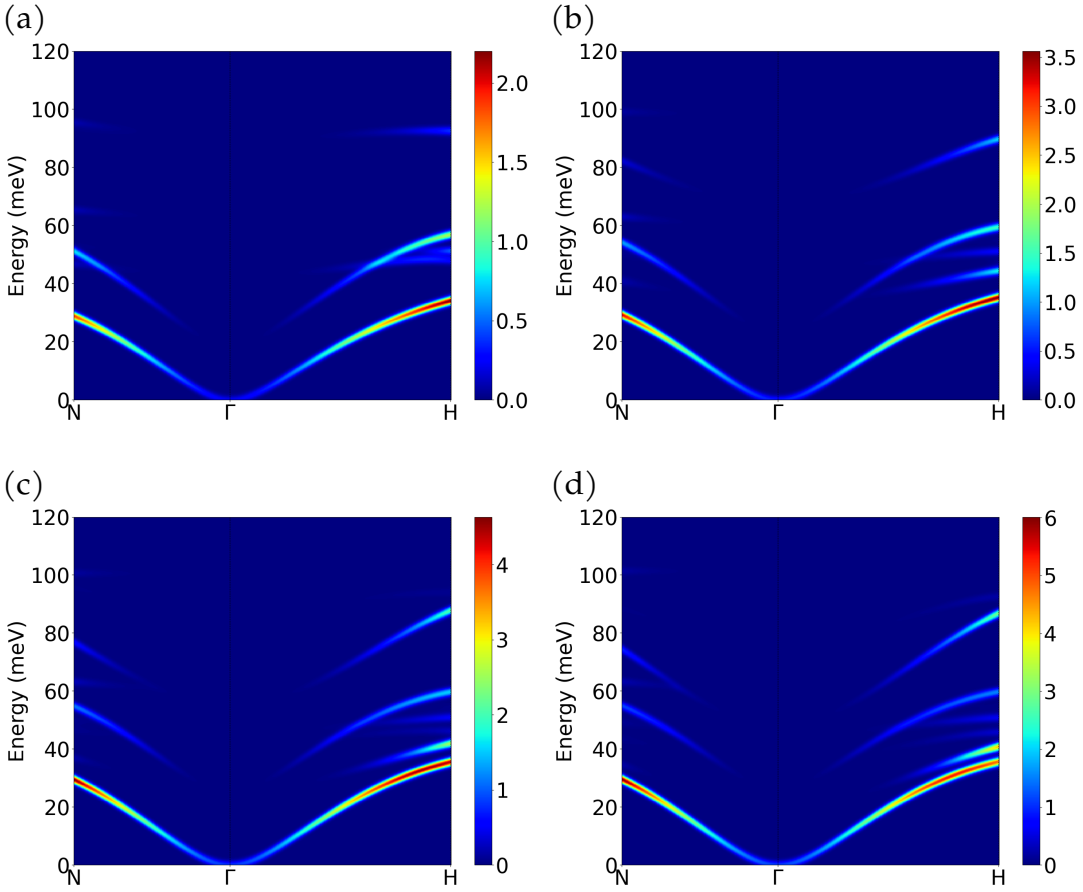

Figure 3.18: Spin scattering function for YIG thin films in the (100) direction. Each image with an increasing number of layers from (a) 5 monolayers, (b) 9 monolayers, (c) 13 monolayers, (d) 17 monolayers. These cases share the same termination, the case given in Fig. 3.16(b).

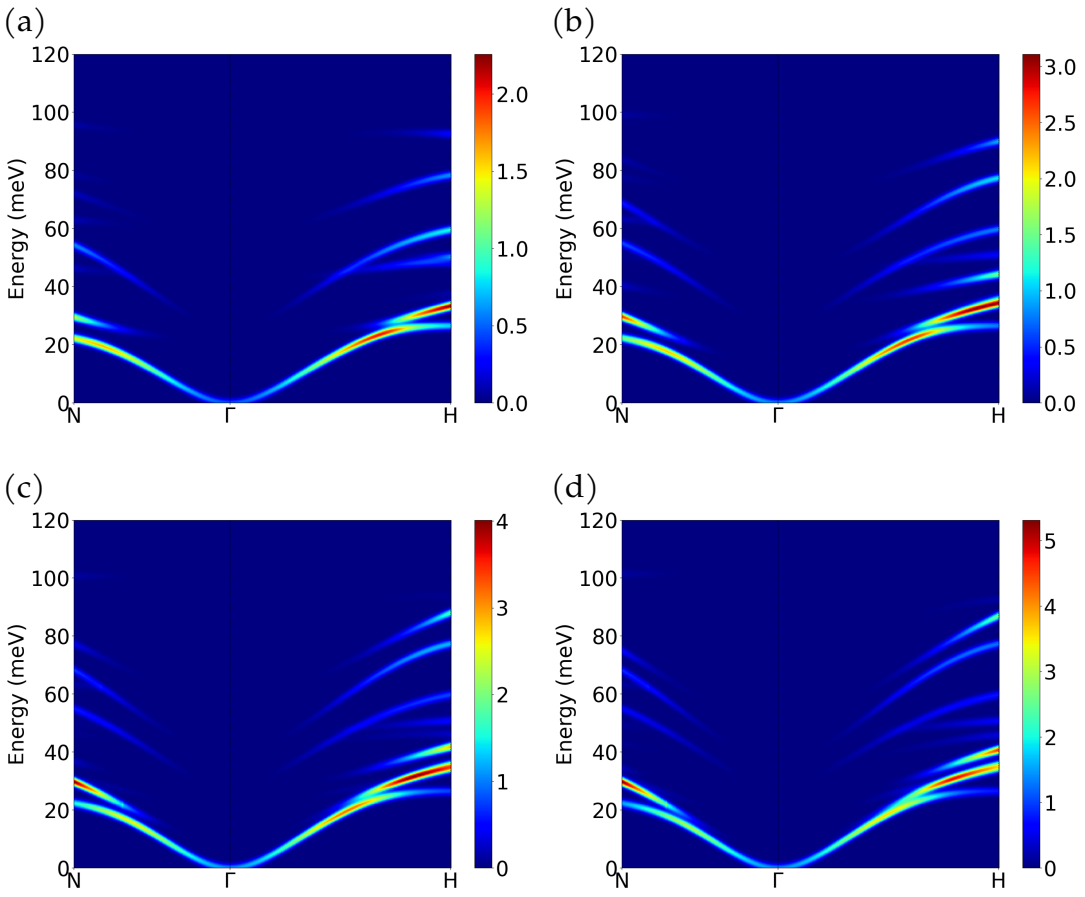

Figure 3.19: Spin scattering function for YIG thin films in the (100) direction. Each image with an increasing number of layers from (a) 6 monolayers, (b) 10 monolayers, (c) 14 monolayers, (d) 18 monolayers. These cases share the same termination, the case given in Fig. 3.16(c).

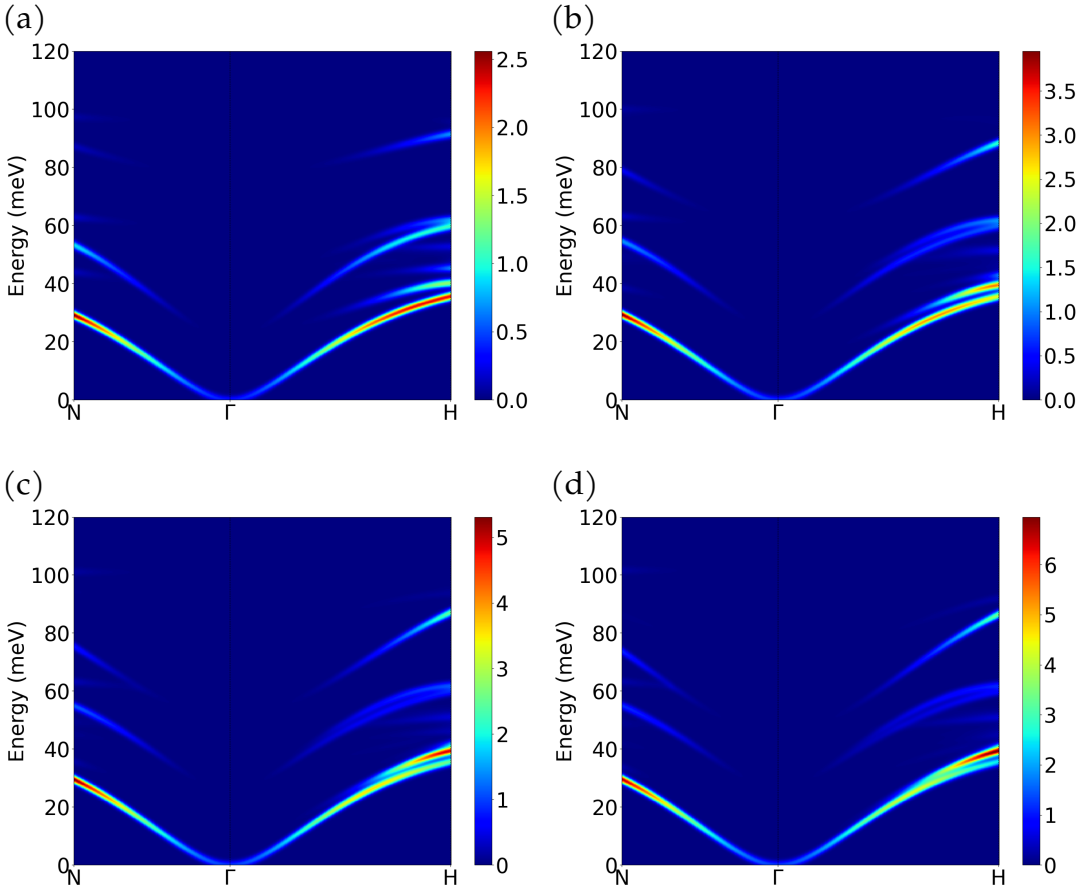

Figure 3.20: Spin scattering function for YIG thin films in the (100) direction. Each image with an increasing number of layers from (a) 7 monolayers, (b) 11 monolayers, (c) 15 monolayers, (d) 19 monolayers. These cases share the same termination, the case given in Fig. 3.16(d).

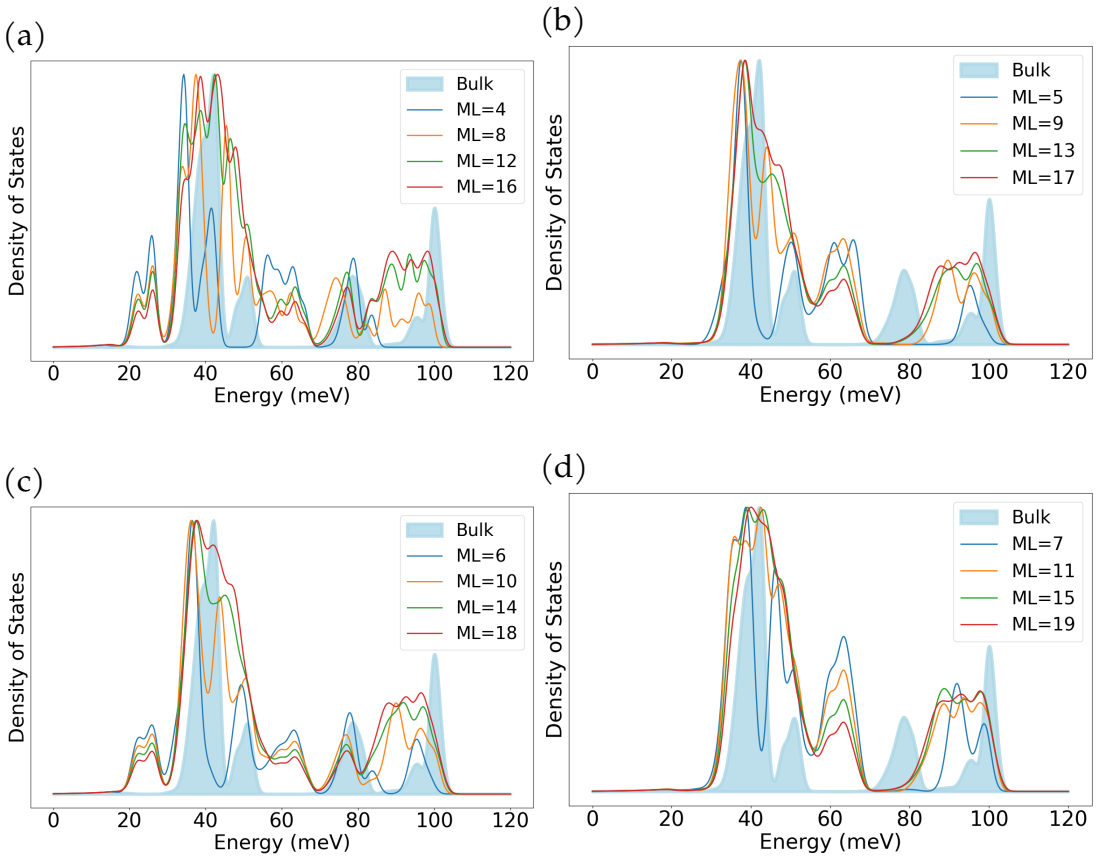

Figure 3.21: Magnon DOS for thin films of YIG, (a) films with termination as given in Fig. 3.16(a), (b) films with termination as given in Fig. 3.16(b), (c) films with termination as given in Fig. 3.16(c), (d) films with termination as given in Fig. 3.16(d), compared with the bulk DOS, given as a light blue filled curve.

Chapter 4

Electron energy loss spectroscopy of magnons

4.1 Inelastic spectroscopy

In section 2.7 we defined the double differential cross-section as the measurement of the relative intensity of scattered particles into a solid angle $d\Omega$, with a wavevector within a small range around $\mathbf{k}_1$ given by $d\mathbf{k}_1$. This general approach can be utilised to quantify the inelastic scattering of electrons by magnons, and this section aims to derive this effect in the form of EEL spectra. Given the small magnitude of the energy transfer of the magnon scattering compared to the typical energy of the electron probe in a STEM-EELS apparatus, we are justified in using the first Born approximation, which neglects multiple inelastic scattering events, hence, the use of the form given in Eq. (2.129) for the transition rate applies. Assuming N scatterers in the target material, and a monochromatic beam with wavevector $\mathbf{k}_0$ in the z-direction with a particle current density $(j_0)_z$, the relative intensity can be written as [95, 122],

$$\frac{d^2\sigma}{d\Omega d\mathbf{k}_1} = \frac{1}{N}\frac{N_0 V \sum_{n_0,n_1,\sigma_0} P_{n_0} P_{\sigma_0} \mathbf{k}_1^2 |\langle n_1,\sigma_1,\mathbf{k}_1|\hat{H}_{inter}|n_0,\sigma_0,\mathbf{k}_0\rangle|^2 \delta(E_{n_0}+E_0-E_{n_1}-E_1)}{(2\pi)^2\hbar(j_0)_z} \tag{4.1}$$

where we are denoting a scattering process, of a system that undergoes a transition from state n_0 to n_1 with energies E_{n_0} and E_{n_1}, respectively. Simultaneously the scattered particle changes its momentum from $\mathbf{k}_0$ and spin state σ_0 with energy E_0 to $\mathbf{k}_1$ with spin state σ_1 with energy E_1. The interaction between the particle and the system is modelled by the interaction Hamiltonian $\hat{H}_{inter}$, while the current density of the particle beam along the z-direction is denoted by $(j_0)_z$. Here, P_{n_0} and P_{σ_0} represent the probabilities of the material to be in state n_0 and the beam to be in the spin state σ_0, before any scattering event. Finally, N represents the number of scatterers, and N_0 is the number of particles in state k_0, and V is the volume of the unit cell.

The choice of the interaction Hamiltonian $\hat{H}_{inter}$ is the central point of the work presented in this chapter. In our case, we are focusing on the electron beam's interaction with the system's magnetic structure. Disregarding the electron charge, we note that the formalism is similar to the INS case, for which the mathematical treatment is well known [93, 94]. The INS interaction Hamiltonian is given to be the interaction between the magnetic field generated by both the intrinsic magnetic moments of the electrons and the orbital angular momentum, with the probe's spin-magnetic moment. This approach leads to a pair of terms, one exchange-like term and another term involving the spin-orbit interaction [122]. In the case of quenched orbital systems, only the former term is taken into account.

For electron-based spectroscopy, however, in addition to this spin-based interaction, the electron's charge must be considered, specifically the alteration to the electron beam's canonical momentum caused by the vector potential originating from the magnons in the magnetic solid. This interaction manifests itself exclusively when electrons are used as probes. In the following sections, the double differential cross-section for both interactions will be expressed in terms of the spin-scattering function. This provides a holistic way to calculate the EEL spectra, where both spin-based and charge-based interactions are simultaneously studied, and their similarities and differences are discussed.

4.1.1 Spin-based interaction

We start with the spin-based interaction. Here, the interaction between the probe's magnetic moment and the magnetic field produced by the magnetic lattice is considered [93]. This derivation follows the case of the inelastic neutron scattering, differing only by the module of the probe's magnetic moment. In principle, both spin and orbital angular momentum give rise to the total atomic magnetic moment. We will assume the orbital angular momentum contribution to be small compared to the spin angular momentum. This assumption is valid for cases where the crystalline field quenches the orbital contribution [79]. In addition, this allows us to set the Landè g-factor to be purely from spin,i.e. $g_e \approx 2$. The spin of the electron beam is defined in terms of the Pauli matrices ($\hat{\boldsymbol{\sigma}}$) such that, $\hat{\mathbf{S}} = \frac{1}{2}\hat{\boldsymbol{\sigma}}$, and we note here that we will be using the convention that angular momentum is measured in units of $\hbar$, in line with the definition given in Eq. (2.1). Hence, the spin-based interaction is given by,

$$\hat{H}^{SB}_{inter} = 2\mu_B \hat{\mathbf{S}} \cdot \mathbf{B} = \mu_B \hat{\boldsymbol{\sigma}} \cdot \mathbf{B} \tag{4.2}$$

where μ_B is the Bohr magneton and $\mathbf{B}$ is the sample's magnetic induction field, which we assume to be generated only by the set of local spins, ignoring the orbital contribution, giving us in terms of the spin operator $\hat{\mathbf{S}}$,

$$\hat{H}^{SB}_{inter} = 2\mu_B^2 \hat{\boldsymbol{\sigma}} \cdot \left[\sum_j \nabla_{r'} \times \left(\frac{\hat{\mathbf{S}}_j \times \mathbf{r}'}{|r'|^3} \right) \right] \tag{4.3}$$

In Eq. (4.3) we are denoting the magnetic field in position $\mathbf{r}'$, produced by the set of magnetic moments indexed by j at positions $\mathbf{r}_j$, as presented in the diagram given in Fig. 4.1 and $\nabla_{\mathbf{r}'}$ is the vector differential operator which acts in the position vector $\mathbf{r}'$.

Assuming that the scattering particle doesn't interact with the system before or after the scattering event, i.e., no multiple scattering events, in line with our prior choice to use the first Born approximation, we can write the total wave function as a product between a plane wave and the magnetic states,

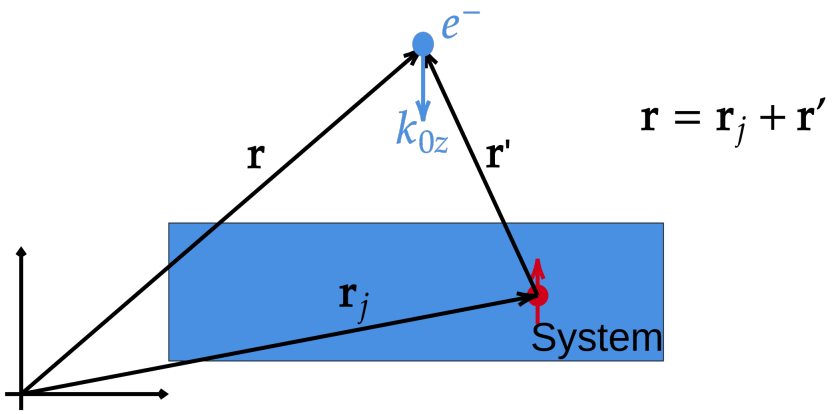

Figure 4.1: Diagram representing the scattering experiment. The notation used is shown to reflect the one used in the derivation.

$$|\mathbf{k}_i, \sigma_i, n_i\rangle \rightarrow |\mathbf{k}_i, \sigma_i\rangle\, |n_i\rangle \tag{4.4}$$

for $i = 0, 1$. Here, $|\mathbf{k}_i\rangle = \frac{1}{\sqrt{V}} e^{-i\mathbf{k}_i \cdot \mathbf{r}}$ is the state of the probing beam, while $|n_i\rangle$, represents the state of the solid, which for our purposes is only transiting between magnetic states, such that $\hat{H}_0\, |n_i\rangle = E_i\, |n_i\rangle$ with $\hat{H}_0$ being the Heisenberg Hamiltonian.

Substituting the Eq. (4.3) into the Fermi Golden Rule of Eq. (4.1) the term we need to evaluate is,

$$\begin{aligned} &\langle n_1, \sigma_1, \mathbf{k}_1 | \hat{H}^{SB}_{inter} | n_0, \sigma_0, \mathbf{k}_0 \rangle \\ &= 2\mu_B^2 \langle n_1, \sigma_1 | \tfrac{1}{V} \int d\mathbf{r} e^{i\mathbf{k}_1 \cdot \mathbf{r}} \hat{\boldsymbol{\sigma}} \cdot \left[\textstyle\sum_j \nabla_{r'} \times \left(\frac{\hat{\mathbf{S}}_j \times (\mathbf{r}')}{|\mathbf{r}'|^3} \right) \right] e^{-i\mathbf{k}_0 \cdot \mathbf{r}} | n_0, \sigma_0 \rangle \end{aligned} \tag{4.5}$$

to proceed we need the following relations,

$$\frac{\mathbf{r}'}{|\mathbf{r}'|^3} = -\nabla_{r'} \left(\frac{1}{\mathbf{r}'} \right) \tag{4.6}$$

$$\frac{1}{\mathbf{r}'} = \frac{1}{2\pi^2} \int d\mathbf{Q} \frac{1}{Q^2} e^{i\mathbf{Q} \cdot \mathbf{r}'} \tag{4.7}$$

where $\mathbf{Q}$ is a dummy wavevector that define the Fourier transform given in Eq. (4.7). With these definitions, we can write,

$$
\begin{aligned}
\nabla_r \times \left(\frac{\hat{\mathbf{S}}_j \times \mathbf{r}'}{|\mathbf{r}'|^3} \right) &= -\nabla_r \times \left[\hat{\mathbf{S}}_j \times \nabla_{r'} \left(\frac{1}{\mathbf{r}'} \right) \right] \\
&= -\nabla_r \times \left[(\hat{\mathbf{S}}_j \times \nabla_{r'}) \left(\frac{1}{\mathbf{r}'} \right) \right] \\
&= -\nabla_r \times \left[(\hat{\mathbf{S}}_j \times \nabla_{r'}) \left(\frac{1}{2\pi^2} \int d\mathbf{Q} \frac{1}{Q^2} e^{i\mathbf{Q}\cdot\mathbf{r}'} \right) \right] \\
&= -\frac{1}{2\pi^2} \int d\mathbf{Q} \frac{1}{Q^2} \nabla_{r'} \times (\hat{\mathbf{S}}_j \times \nabla_{r'}) e^{i\mathbf{Q}\cdot\mathbf{r}'} \\
&= -\frac{1}{2\pi^2} \int d\mathbf{Q} \frac{1}{Q^2} \{ (i\mathbf{Q}) \times (\hat{\mathbf{S}}_j \times (i\mathbf{Q})) \} e^{i\mathbf{Q}\cdot\mathbf{r}'} \\
&= \frac{1}{2\pi^2} \int d\mathbf{Q} \frac{1}{Q^2} \{ \mathbf{Q} \times (\hat{\mathbf{S}}_j \times \mathbf{Q}) \} e^{i\mathbf{Q}\cdot\mathbf{r}'}
\end{aligned}
\tag{4.8}
$$

plugging the result from Eq. (4.8) into Eq. (4.5) we get,

$$
\begin{aligned}
&= 2\mu_B^2 \langle n_1, \sigma_1 | \tfrac{1}{V} \textstyle\int d\mathbf{r} e^{i\mathbf{k}_1\cdot\mathbf{r}} \sigma \cdot \left[\sum_j \frac{1}{2\pi^2} \int d\mathbf{Q} \frac{1}{Q^2} [\mathbf{Q} \times (\hat{\mathbf{S}}_j \times \mathbf{Q})] e^{i\mathbf{Q}\cdot\mathbf{r}'} \right] e^{-i\mathbf{k}_0\cdot\mathbf{r}} | n_0, \sigma_0 \rangle \\
&= 2\mu_B^2 \langle n_1, \sigma_1 | \tfrac{1}{V} \textstyle\int d\mathbf{r} e^{-i\mathbf{q}\cdot\mathbf{r}} \sigma \cdot \left[\sum_j \frac{1}{2\pi^2} \int d\mathbf{Q} \frac{1}{Q^2} [\mathbf{Q} \times (\hat{\mathbf{S}}_j \times \mathbf{Q})] e^{i\mathbf{Q}\cdot\mathbf{r}'} \right] | n_0, \sigma_0 \rangle \\
&= 2\mu_B^2 \langle n_1, \sigma_1 | \tfrac{1}{V} \textstyle\int d\mathbf{r} e^{-i\mathbf{q}\cdot\mathbf{r}} \sigma \cdot \left[\sum_j \frac{1}{2\pi^2} \int d\mathbf{Q} \frac{1}{Q^2} [\mathbf{Q} \times (\hat{\mathbf{S}}_j \times \mathbf{Q})] e^{i\mathbf{Q}\cdot(\mathbf{r} - \mathbf{r}_j)} \right] | n_0, \sigma_0 \rangle \\
&= 2\mu_B^2 \langle n_1, \sigma_1 | \tfrac{1}{V} \textstyle\int d\mathbf{r} e^{-i\mathbf{q}\cdot\mathbf{r}} \sigma \cdot \left[\sum_j \frac{1}{2\pi^2} \int d\mathbf{Q} \frac{1}{Q^2} [\mathbf{Q} \times (\hat{\mathbf{S}}_j \times \mathbf{Q})] e^{i\mathbf{Q}\cdot\mathbf{r}} \right] e^{-i\mathbf{Q}\cdot\mathbf{r}_j} | n_0, \sigma_0 \rangle \\
&= 2\mu_B^2 \langle n_1, \sigma_1 | \tfrac{1}{V} \sigma \cdot \textstyle\int d\mathbf{Q} \int d\mathbf{r} e^{-i(\mathbf{q}-\mathbf{Q})\cdot\mathbf{r}} \left[\sum_j \frac{1}{2\pi^2} \frac{1}{Q^2} [\mathbf{Q} \times (\hat{\mathbf{S}}_j \times \mathbf{Q})] \right] e^{-i\mathbf{Q}\cdot\mathbf{r}_j} | n_0, \sigma_0 \rangle \\
&= 2\mu_B^2 \langle n_1, \sigma_1 | \tfrac{1}{V} \sigma \cdot \textstyle\int d\mathbf{Q} \delta(\mathbf{Q} - \mathbf{q}) \left[\sum_j \frac{(2\pi)^3}{2\pi^2} \frac{1}{Q^2} [\mathbf{Q} \times (\hat{\mathbf{S}}_j \times \mathbf{Q})] \right] e^{-i\mathbf{Q}\cdot\mathbf{r}_j} | n_0, \sigma_0 \rangle \\
&= 8\pi \tfrac{\mu_B^2}{V} \tfrac{1}{q^2} \langle n_1, \sigma_1 | \left[\textstyle\sum_j \sigma \cdot [\mathbf{q} \times (\hat{\mathbf{S}}_j \times \mathbf{q})] \right] e^{-i\mathbf{q}\cdot\mathbf{r}_j} | n_0, \sigma_0 \rangle
\end{aligned}
\tag{4.9}
$$

where we defined $\mathbf{q} = (\mathbf{k}_0 - \mathbf{k}_1)$, the scattering vector, used the relation between the different position vectors $\mathbf{r} = \mathbf{r}_j + \mathbf{r}'$ and using the relation $\frac{1}{(2\pi)^3} \int d\mathbf{r} e^{-i(\mathbf{q}-\mathbf{Q})\cdot\mathbf{r}} =$

$\delta(\mathbf{Q}-\mathbf{q})$. For Eq. 4.1 we have to evaluate,

$$|\langle n_0,k_0|H_{inter}|n_1,k_1\rangle|^2 = \left(\frac{8\pi\mu_B^2}{V}\right)^2 [\langle n_1,\sigma_1|\sum_j e^{-i\mathbf{q}\cdot\mathbf{r}_j}\sigma\cdot\left[\tilde{\mathbf{q}}\times\left(\hat{\mathbf{S}}_j\times\tilde{\mathbf{q}}\right)\right]|n_0,\sigma_0\rangle \langle n_0,\sigma_0|\sum_{j'} e^{i\mathbf{q}\cdot\mathbf{r}_{j'}}\sigma\cdot\left[\tilde{\mathbf{q}}\times\left(\hat{\mathbf{S}}_{j'}\times\tilde{\mathbf{q}}\right)\right]|n_1,\sigma_1\rangle] \tag{4.10}$$

where we defined $\tilde{\mathbf{q}}=\dfrac{\mathbf{q}}{q}$.

For a spin-unpolarised beam we have the following identity

$$\sum_\sigma p_\sigma\langle\sigma|\sigma_\alpha\sigma_\beta|\sigma\rangle=\delta_{\alpha\beta} \tag{4.11}$$

So, only terms that involve σ_x^2, σ_y^2 and σ_z^2 will be non-zero. Returning to Eq. (4.1), taking $(j_0)_z$ as $\dfrac{N_0}{V}\dfrac{\hbar\mathbf{k}_0}{m_e}$, with m_e being the mass of the electron, and $dE_1=\frac{\hbar^2k_1}{m_e}dk_1$, we have,

$$\frac{d^2\sigma}{d\Omega d\mathbf{k}_1}=\left(\frac{4\mu_B^2m_e}{\hbar^2}\right)^2\frac{k_1}{k_0}\sum_{\alpha\beta}\mathcal{E}\left(\tilde{\mathbf{q}}\right)_{\alpha\beta}\mathcal{S}_{\alpha\beta}(\mathbf{q},\omega) \tag{4.12}$$

with

$$\mathcal{E}\left(\tilde{\mathbf{q}}\right)=\begin{pmatrix}1-\tilde{q}_x\tilde{q}_x & -\tilde{q}_x\tilde{q}_y & -\tilde{q}_x\tilde{q}_z\\ -\tilde{q}_y\tilde{q}_x & 1-\tilde{q}_y\tilde{q}_y & -\tilde{q}_y\tilde{q}_z\\ -\tilde{q}_z\tilde{q}_x & -\tilde{q}_z\tilde{q}_y & 1-\tilde{q}_z\tilde{q}_z\end{pmatrix} \tag{4.13}$$

and we have written it in terms of the spin-scattering function by using the identity,

$$\delta(E_{n_0}+E_0-E_{n_1}-E_1)=\frac{1}{2\pi\hbar}\int dt e^{i(E_{n_0}-E_{n_1})t/\hbar}e^{i\omega t} \tag{4.14}$$

where ω is defined by, $\hbar\omega=E_0-E_1$. Particularly here, we will use the following form for the spin-scattering function,

$$\mathcal{S}_{\alpha\beta}(\mathbf{q},\omega)=\frac{1}{2\pi N}\sum_{j,j'}F_j^*(\mathbf{q})F_{j'}(\mathbf{q})\int dt e^{-i\omega t}e^{-i\mathbf{q}\cdot(\mathbf{r}_j-\mathbf{r}_{j'})}\langle s_j^\alpha(0)s_{j'}^\beta(t)\rangle_T \tag{4.15}$$

where the magnetic form factor $F_j(\mathbf{q})$ is included, details are given in Appendix E and $\langle S_j^\alpha(0)S_{j'}^\beta(t)\rangle_T$ can be recognised as the spin-spin correlation function.

The form of Eq. (4.12) is corroborated by the calculation for the thermal neutron scattering in the literature, as expected, differing only by the coupling constant. For the spin-based EELS, the coupling constant is given by $\left(\frac{4\mu_B^2 m_e}{\hbar^2}\right)^2 = 0.0794$ barn, considerably smaller compared to INS evaluated as approximately 0.291 barn [98], primarily due to the electron's smaller magnetic moment compared to that of neutrons.

4.1.2 Charge-based interaction

Now we move on to the charge-based interaction, where we will use the procedure given in [123] to get the interaction term.

The central point of this discussion is the mental picture that the magnetic field generated by the system, both in the ground state and in excited states, will affect the canonical momentum of the incoming electrons.

The Hamiltonian for the experiment is given by,

$$\hat{H} = \hat{H}_0 + \frac{(\hat{\mathbf{p}} + e\hat{\mathbf{A}})^2}{2m_e} - eV(\mathbf{r}) \tag{4.16}$$

It represents a magnetically ordered solid, given by $\hat{H}_0$, governed by the Heisenberg Hamiltonian. Additionally, includes a spin-unpolarised high-energy electron with momentum $\hat{\mathbf{p}}$, with charge e and mass m_e, represented by the second term. The interaction of the incoming electron with the electron and nuclear charges is characterised by the charge potential $V(\mathbf{r})$.

Next, we will evaluate the vector potential $\hat{\mathbf{A}}$ in position $\mathbf{r}'$, produced by the set of magnetic moments indexed by j at positions $\mathbf{r}_j$, as defined in Fig. 4.1 which can be written as,

$$\hat{\mathbf{A}} = -2\mu_B \sum_j \left(\hat{\mathbf{S}}_j \times \frac{\mathbf{r}'}{|\mathbf{r}'|^3}\right) \tag{4.17}$$

where we used the same relation between the magnetic moment and the spin operator as in Eq. (4.3). Substituting Eq. (4.17) into Eq. (4.16) and using the commutation relation $[\hat{\mathbf{p}}, \hat{\mathbf{A}}] = 0$, and omitting the weaker $\hat{\mathbf{A}}^2$ while noting that $\mu_B = \frac{e\hbar}{2m_e}$ in SI, we can write Eq. (4.16) as,

$$\begin{aligned}\hat{H} &= \hat{H}_0 + \frac{\hat{\mathbf{p}}^2}{2m_e} - eV(\mathbf{r}) + \frac{e}{m_e}\hat{\mathbf{p}}\cdot\hat{\mathbf{A}} \\ &= \hat{H}_0 + \frac{\hat{\mathbf{p}}^2}{2m_e} - eV(\mathbf{r}) - \frac{2\mu_B e}{m_e}\hat{\mathbf{p}}\cdot\sum_j\left(\hat{\mathbf{S}}_j\times\frac{\mathbf{r}'}{|\mathbf{r}'|^3}\right) \\ &= \hat{H}_0 + \frac{\hat{\mathbf{p}}^2}{2m_e} - eV(\mathbf{r}) - \frac{4\mu_B^2}{\hbar}\hat{\mathbf{p}}\cdot\sum_j\left(\hat{\mathbf{S}}_j\times\frac{\mathbf{r}'}{|\mathbf{r}'|^3}\right)\end{aligned} \tag{4.18}$$

hence, we have an interaction in the form,

$$\hat{H}_{inter} = -\frac{4\mu_B^2}{\hbar}\hat{\mathbf{p}}\cdot\sum_j\left(\hat{\mathbf{S}}_j\times\frac{\mathbf{r}'}{|\mathbf{r}'|^3}\right) \tag{4.19}$$

coming from the notion that this is the additional energy change to the electron beam, due to the presence of the magnetic material.

Substituting the Eq. (4.19) into Fermi's Golden Rule of Eq. (4.1) we obtain,

$$\begin{aligned}&\langle n_1,\sigma_1,\mathbf{k}_1|\,\hat{H}^{CB}_{inter}\,|n_0,\sigma_0,\mathbf{k}_0\rangle = \\ &\quad\frac{4\mu_B^2}{\hbar V}\langle n_1,\sigma_1|\int d\mathbf{r}e^{-i\mathbf{k}_1\cdot\mathbf{r}}\left[\sum_j\hat{\mathbf{p}}\cdot\left(\frac{\hat{\mathbf{S}}_j\times\mathbf{r}'}{|\mathbf{r}'|^3}\right)\right]e^{i\mathbf{k}_0\cdot\mathbf{r}}\,|n_0,\sigma_0\rangle\end{aligned} \tag{4.20}$$

using once more the definitions in Eqs. (4.6) and (4.7), and the definition for the momentum operator, $\hat{\mathbf{p}} = -i\hbar\nabla_{\mathbf{r}}$, we can perform a similar procedure as in Eq. (4.8) and get,

$$\begin{aligned}\hat{\mathbf{p}}\cdot\left(\frac{\hat{\mathbf{S}}_j\times\mathbf{r}'}{|\mathbf{r}'|^3}\right) &= -\frac{i}{2\pi^2}\hat{\mathbf{p}}\cdot\int d\mathbf{Q}\frac{1}{Q^2}\{(\hat{\mathbf{S}}_j\times\mathbf{Q})\}e^{i\mathbf{Q}\cdot\mathbf{r}'} \\ &= -\frac{\hbar}{2\pi^2}\nabla_{\mathbf{r}}\cdot\int d\mathbf{Q}\frac{1}{Q^2}\{(\hat{\mathbf{S}}_j\times\mathbf{Q})\}e^{i\mathbf{Q}\cdot\mathbf{r}'}\end{aligned} \tag{4.21}$$

plugging the result from Eq. (4.21) into Eq. (4.20), similarly to the procedure in Eq. (4.9) we get,

$$
\begin{aligned}
&= -\tfrac{4\mu_B^2}{\hbar V}\left\langle n_1,\sigma_1\right| \int d\mathbf{r} e^{i\mathbf{k}_1\cdot\mathbf{r}}\left[\textstyle\sum_j \hat{\mathbf{p}}\cdot\left(\frac{\hat{\mathbf{S}}_j\times\mathbf{r}'}{|\mathbf{r}'|^3}\right)\right] e^{-i\mathbf{k}_0\cdot\mathbf{r}}\left|n_0,\sigma_0\right\rangle \\
&= -\tfrac{4\mu_B^2}{\hbar V}\left\langle n_1,\sigma_1\right| \int d\mathbf{r} \sum_j e^{i\mathbf{k}_1\cdot\mathbf{r}}\nabla_{\mathbf{r}}\cdot\left[\tfrac{\hbar}{2\pi^2}\int d\mathbf{Q}\tfrac{1}{Q^2}(\hat{\mathbf{S}}_j\times\mathbf{Q})e^{i\mathbf{Q}\cdot\mathbf{r}'}\right] e^{-i\mathbf{k}_0\cdot\mathbf{r}}\left|n_0,\sigma_0\right\rangle \\
&= \tfrac{4\mu_B^2}{V}\left\langle n_1,\sigma_1\right| \int d\mathbf{r} \sum_j e^{i\mathbf{q}\cdot\mathbf{r}} i\mathbf{k}_0\cdot\left[\tfrac{1}{2\pi^2}\int d\mathbf{Q}\tfrac{1}{Q^2}(\hat{\mathbf{S}}_j\times\mathbf{Q})e^{i\mathbf{Q}\cdot(\mathbf{r}-\mathbf{r}_j)}\right]\left|n_0,\sigma_0\right\rangle \\
&= \tfrac{4\mu_B^2}{V} i\left\langle n_1,\sigma_1\right| \int d\mathbf{Q}\int d\mathbf{r} e^{i(\mathbf{Q}+\mathbf{q})\cdot\mathbf{r}} i\mathbf{k}_0\cdot\left[\sum_j \tfrac{1}{2\pi^2}\tfrac{1}{Q^2}(\hat{\mathbf{S}}_j\times\mathbf{Q})\right] e^{-i\mathbf{Q}\cdot\mathbf{r}_j}\left|n_0,\sigma_0\right\rangle \\
&= \tfrac{4\mu_B^2}{V} i\left\langle n_1,\sigma_1\right| \int d\mathbf{Q}\delta(\mathbf{Q}+\mathbf{q}) i\mathbf{k}_0\cdot\left[\sum_j \tfrac{(2\pi)^3}{2\pi^2}\tfrac{1}{Q^2}(\hat{\mathbf{S}}_j\times\mathbf{Q})\right] e^{-i\mathbf{Q}\cdot\mathbf{r}_j}\left|n_0,\sigma_0\right\rangle \\
&= \tfrac{16\pi\mu_B^2}{V} i\left\langle n_1,\sigma_1\right| \int d\mathbf{Q}\delta(\mathbf{Q}+\mathbf{q})\mathbf{k}_0\cdot\left[\sum_j \tfrac{1}{Q^2}(\hat{\mathbf{S}}_j\times\mathbf{Q})\right] e^{-i\mathbf{Q}\cdot\mathbf{r}_j}\left|n_0,\sigma_0\right\rangle \\
&= -\tfrac{16\pi\mu_B^2}{V} i\left\langle n_1,\sigma_1\right| \sum_j e^{i\mathbf{q}\cdot\mathbf{r}_j}\mathbf{k}_0\cdot\left[\tfrac{1}{q^2}(\hat{\mathbf{S}}_j\times\mathbf{q})\right]\left|n_0,\sigma_0\right\rangle
\end{aligned}
\tag{4.22}
$$

using the same procedure outlined in the spin-based case and assuming $\mathbf{k_0} = k_{0z}$, i.e. the incoming beam arrives aligned with the z-axis, we finally get,

$$
\frac{d^2\sigma}{d\Omega d\mathbf{k}_1} = \left(\frac{8\mu_B^2 m_e}{\hbar^2}\right)^2 k_1 k_{0z}\frac{1}{q^2}\sum_{\alpha\beta}\mathcal{E}\left(\tilde{\mathbf{q}}\right)_{\alpha\beta}\mathcal{S}_{\alpha\beta}(\mathbf{q},\omega) \tag{4.23}
$$

with,

$$
\mathcal{E}\left(\tilde{\mathbf{q}}\right) = \begin{pmatrix} \tilde{q}_y\tilde{q}_y & \tilde{q}_x\tilde{q}_y & 0 \\ \tilde{q}_y\tilde{q}_x & \tilde{q}_x\tilde{q}_x & 0 \\ 0 & 0 & 0 \end{pmatrix} \tag{4.24}
$$

with the same definitions we used for Eq. (4.15). In the case of charge-based interaction, the coupling constant is $\left(\frac{8\mu_B^2 m_e}{\hbar^2}\right)^2 = 0.3176$ barn, which has the same order of magnitude as the neutron scattering coupling constant, evaluated as approximately 0.291 barn [98].

The charge-related interaction can be recognised as taking a similar form to the spin-based interaction but with a different momentum dependence.

The calculation of the spin-scattering function $\mathcal{S}_{\alpha\beta}(\mathbf{q},\omega)$ is necessary to quantify both interactions and can be performed in a variety of ways, under the linear spin-wave approximation for bulk systems [98, 124] and thin films as described in chapter 3, or using atomistic spin dynamics [125].

To focus on the momentum dependence of the EELS spectra as described

by Eqs. (4.12) and (4.23) we will use the approach, which follows a similar procedure as in chapter 3. We only need to change equation (3.17) such that $\mathbf{q}_{\parallel} \rightarrow \mathbf{q}$ and $N_{\parallel} \rightarrow N$, next, the Holstein-Primakoff transformation is used, and the bosonic creation and annihilation operators are projected on their diagonalised counterparts using the Bogoliubov transformation. Furthermore, "Kubler's trick" [97] is used, which allows the calculation of the magnon modes with the freedom to align the local spins in an arbitrary orientation. In this approach, the spin operator in the local reference frame ($\hat{\overline{\mathbf{S}}}_j$), is connected to the laboratory reference frame ($\hat{\mathbf{S}}_j$), by the unitary matrix $\mathcal{R}_j$ which is defined such that in the local reference frame, the spin always points in the z-direction, and it is given by,

$$\mathcal{R}_j = \begin{pmatrix} \cos\theta_j \cos\phi_j & \cos\theta_j \sin\phi_j & -\sin\theta_j \\ -\sin\phi_j & \cos\phi_j & 0 \\ \sin\theta_j \cos\phi_j & \sin\theta_j \sin\phi_j & \cos\theta_j \end{pmatrix} \tag{4.25}$$

such that, $\hat{\overline{\mathbf{S}}}_j = \mathcal{R}_j \cdot \hat{\mathbf{S}}_j$, where θ_j and ϕ_j are the polar and azimuthal angles, respectively, of the spins in the laboratory reference frame [98].

4.1.3 Discussion

To demonstrate the method, we will use Ytrium Iron Garnet (YIG), a material of choice for magnon applications. For the calculation of the spin-scattering function, we will use the same parameters as in section 3.6, and for the magnetic form factor, we used the values for Fe^{+3} given in the literature [126].

The distinctions between the spin and charge interactions stem from their dependence on three factors: the scattering vector q, the variation in intensity relative to the angle between the beam's orientation and that of the local magnetic moments, and primarily, the dependence on the beam's initial momentum. The charge-based interaction is linear with the beam momentum $\mathbf{k}_0$ while the spin-based follows a $\mathbf{k}_0^{-1}$ relation, hence it will be dominant for higher acceleration voltages.

To further compare the momentum dependence of the spin-based $f_{SB}(q, k_0)$ and charge-based interactions $f_{CB}(q, k_0)$, we rewrite them in terms of the inci-

dent beam wavevector ($\mathbf{k}_0$) and scattering vector ($\mathbf{q}$), using the relation $\mathbf{q} = \mathbf{k}_1 - \mathbf{k}_0$,

$$\begin{cases} f_{SB}(q, k_0) & = \frac{q+k_0}{k_0} \\ f_{CB}(q, k_0) & = \frac{k_0}{q} + \frac{k_0^2}{q^2} \end{cases} \tag{4.26}$$

we note that these relations are valid for low-angle scattering, i.e. for small perturbations to the beam path, owing to the nature of the first Born approximation used.

The relations given in Eq. (4.26) are presented in Fig. 4.2 as contour plots, where the arrows represent the intensity gradient and the x-axis shows the wavevector correspondent to a window of acceleration voltages between 30 kV to 300 kV. Note, similar to the case of inelastic scattering of electrons by phonons [59], the charge-related magnon scattering function exhibits an overall dependence of q^{-2}, thus the magnon EELS signal should be strongest in the first Brillouin zone, in contrast when only spin-based interaction is present, case when neutron are the probe, where the data has a stronger signal at larger q. In addition, the linear dependence on the incident beam wavevector $\mathbf{k}_0$ in the charge-based interaction is in stark contrast with the inverse dependence in the inelastic scattering of electrons by phonons, pointing to the possibility of enhancing the magnon peaks with respect to the phonon peaks by increasing the acceleration voltages in the STEM-EELS experiment.

Another important observation concerns the coupling constants. In the case of charge-based interaction, the coupling constant is $\left(\frac{8\mu_B^2 m_e}{\hbar^2}\right)^2 = 0.3176$ barn, which has the same order of magnitude as the neutron scattering coupling constant, evaluated as approximately 0.291 barn [98]. On the other hand, for the spin-based interaction, the coupling constant is given by $\left(\frac{4\mu_B^2 m_e}{\hbar^2}\right)^2 = 0.0794$ barn, considerably smaller compared to INS, primarily due to the electron's smaller magnetic moment compared to that of neutrons.

In Fig. 4.3 we compare the experimentally acquired INS given in [47] with the calculated spin-based EELS using Eq. (4.12) and the calculated charge-based EELS using Eq. (4.23) the colour bar intensity is given in terms of spin-based interaction coupling constant, for an acceleration voltage of 30 kV.

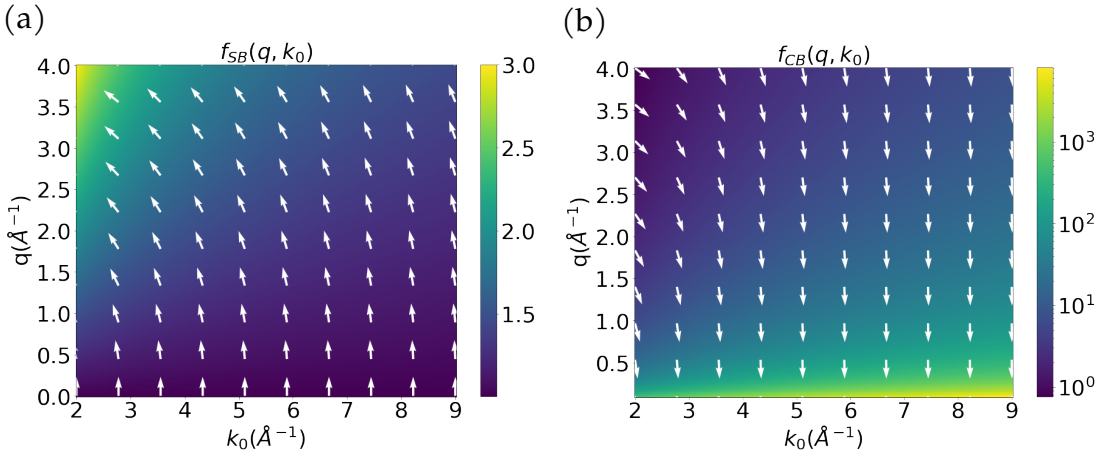

Figure 4.2: Cross-section dependence with the scattering vector q and incoming beam wavevector k_0 for (a) spin-based interaction and (b) charge-based interaction. Arrows indicate the gradient of the intensity.

Taking the definition of the spin orientation given in Eq. (4.25), we kept the orientation of the magnetic moments aligned parallel to the z-axis by setting $\theta = 0$ and $\phi = 0$, while the electron beam is kept along the z-axis. We can see the similarities between the experiment and the calculated spectra for the EELS, particularly the same modes are active, and the spin-based interaction exhibits a similar intensity profile as the INS data, as expected by the similarity in the interaction. The intensity difference between the spin-based and charge-based interaction comes mainly due to the q dependence. Under the previous discussion, both the intensities given in Figs. 4.3(b) and 4.3(c) coexist in the EELS spectra.

To discuss the intensity dependence with the relative orientation of the beam wavevector and the local magnetic moments, we will evaluate the EELS for the path $N - \Gamma - H$ keeping $\phi = 0$ and varying the value of θ for an acceleration voltage of 30 kV. For the spin-based interaction shown in Fig. 4.4 the effect of changing the relative angle between the probe wavevector and the local magnetic moments is not very pronounced, given that the final form of the double differential cross-section for this interaction is independent of the orientation of $\mathbf{k}_0$. In this case, the intensity change will be due to the interplay of $\mathcal{E}\left(\tilde{\mathbf{q}}\right)_{\alpha\beta}$ given in Eq. (4.13) and the spin scattering tensor $\mathcal{S}_{\alpha\beta}(\mathbf{q}, \omega)$.

Conversely, we see a strong dependence on the magnetic moments orienta-

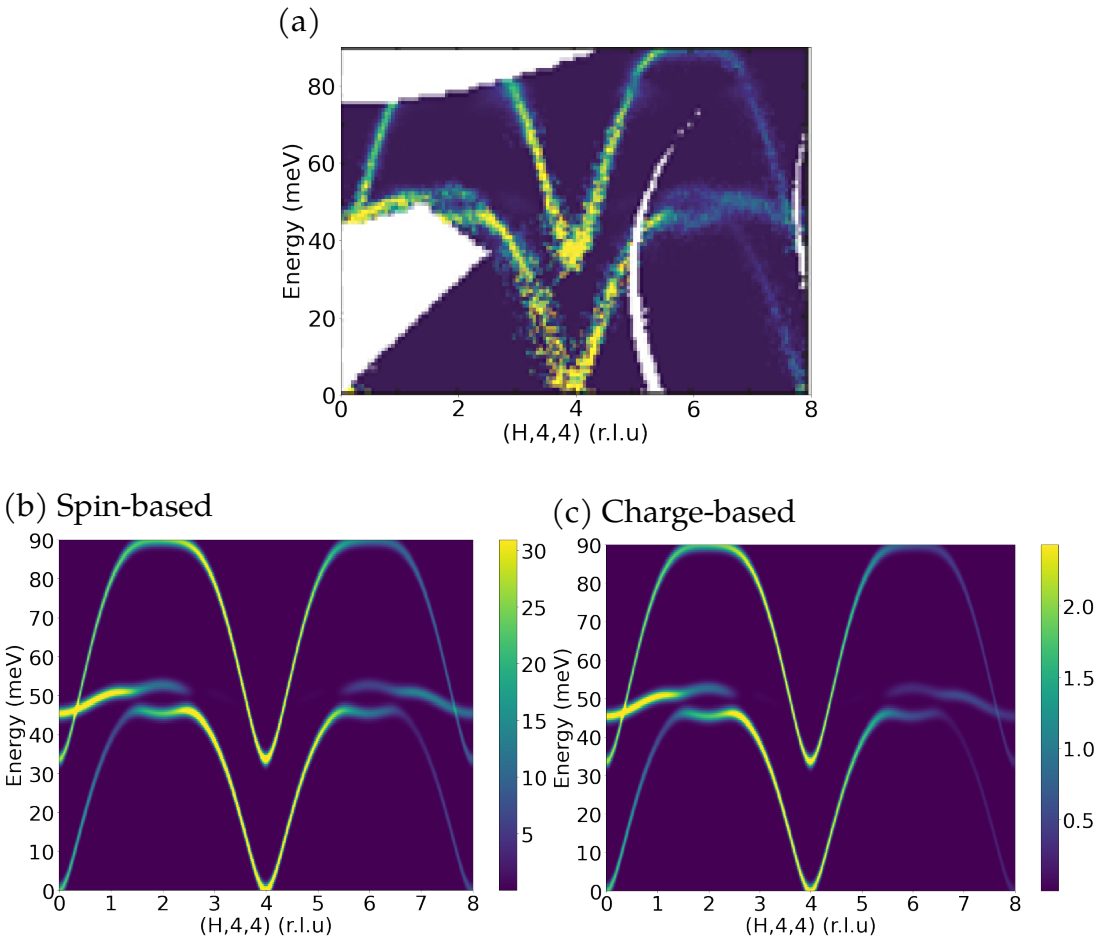

Figure 4.3: Inelastic scattering by magnons: a) Experimental inelastic neutron scattering [47], b) theoretical evaluation of inelastic neutron scattering, c) charge-related EELS. All the calculations were performed for a relative angle between the probe's wave vector and the Néel vector $\theta = 0$.

tion in the charge-based interaction as shown in Fig. 4.5. In this context, we observe a discernible dependency of the scattering intensity in the path $\Gamma - H$ with variations in the polar angle, denoted by θ, of the material's magnetic moments. This observation underscores the influence of magnetic moment alignment on the scattering process, particularly in this case, since the interaction depends on the scalar product of the incoming beam wavevector $(\mathbf{k}_0)$ with the vector product between the spin operator and the position vector. We can see that, the intensity varies with a cosine relation with the angle between the magnetic moments' orientation and the beam wavevector $\mathbf{k}_0$.

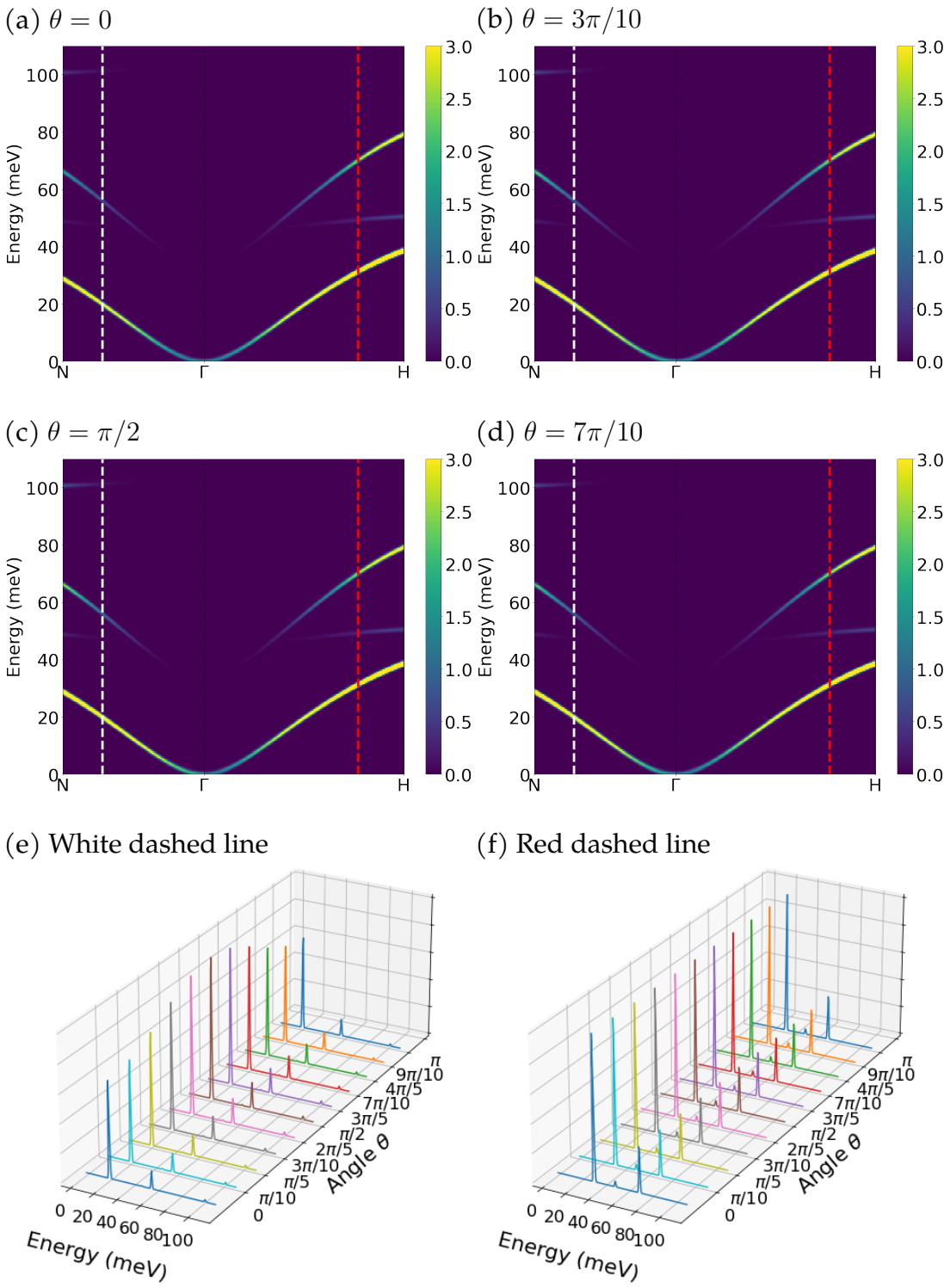

Figure 4.4: a-d) Spin-related EELS, for varying relative angles θ between the probe's wave vector and the Néel vector. e-f) Angle-dependent intensity for a particular point in momentum space, showing a weak angle dependence on the point represented by the red and white dashed lines.

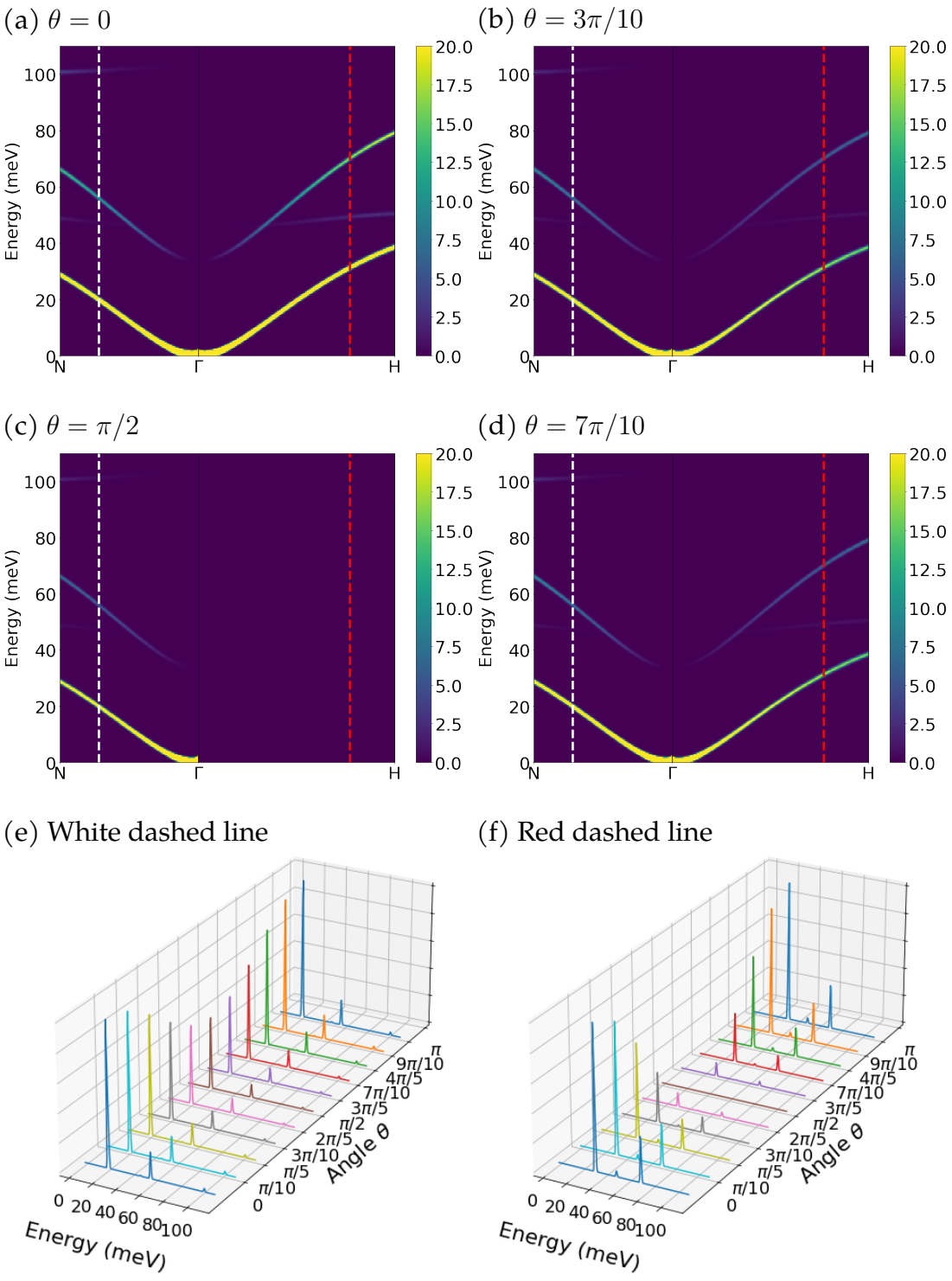

Figure 4.5: a-d) Charge-related EELS, for varying relative angles θ between the probe's wave vector and the Néel vector. e-f) Angle-dependent intensity for a particular point in momentum space, showing a strong angle dependence on the point represented by the red dashed line.

Chapter 5

Conclusions and future work

The study of magnetic systems in low dimensionalities, such as in thin films, is crucial for the development of novel magnonics-based devices as well as the fundamental understating of spin waves in real systems. This work also underpins the experimental studies of magnons with high spatial resolution, highly sought for the design of heterostructures essential for device development.

This work outlines a methodology to calculate the inelastic scattering for magnons relying on the spin scattering function, using a second quantisation approach. This allows for a Hamiltonian that includes lower dimensionalities in the systems considered, which applies to relevant thin film systems including bcc Fe(100), YIG(100), and NiO in the (100) and (111) crystallographic orientations. The calculated results reveal distinct characteristics that emphasise the significance of film thickness and crystal orientation on the magnon modes in these systems. In all cases, the emergence of softer modes related to the partial interaction of the magnetic moments close to the surfaces of the material is observed. The appearance of these softer modes related to confinement is evident in the evaluated magnon density of states, where the emergence of peaks at lower energies, which we associate with confinement is seen. By comparing the magnon density of states for the two different crystallographic orientations of NiO we observe that the confinement-related peak appears at different energies, 65 meV and 42 meV for (100) and (111) surfaces, respectively, showing the importance of the direction in which dimensionality is reduced. The finite crystal size leads to granularity in the spin scattering function across various directions in the Brillouin zone, due to the quantisation of the

quasi-momenta. This effect is comparable in the considered two different crystallographic orientations of NiO, where the granularity appears in the path in reciprocal space that is oriented in the direction of the thin film. Additionally, we demonstrate the role of magneto-crystalline anisotropy in both Fe and NiO films, which leads to an overall hardening of the magnon modes. When anisotropy is only included in surface layers, illustrated in the case of bcc Fe, the confinement-related magnon DOS peak shifts to higher energies with the increase of the surface anisotropy.

Furthermore, we propose a method to quantify the non-spin polarised magnon-related EELS, separately for the spin-based interaction and a charge-based interaction, which combined with the spin-scattering function for thin films can be a valuable tool to characterise the local magnon spectra of magnetically ordered thin films. The high spatial resolution enabled by e-beam in STEM, paired with the magnetic moment orientation sensitive nature of the charge-based interaction in the non-spin polarised EELS spectrum, allows to locally probe the Neel vector relative to the electron beam momentum. Given that the charge-based interaction exhibits a q^{-2} dependence with the scattering vector q, and a linear dependence with the e-beam momentum k_0, we predict that this effect will be more easily distinguished in the first Brillouin zone, and higher acceleration voltages. These predictions also point to a possible means to enhance the magnon EELS relative to the phonon EELS, by increasing acceleration voltages. Since phonon EELS, although following the same q^{-2} dependence with the scattering vector, follow an inverse relation k_0^{-1} with the e-beam momentum, being then suppressed for higher acceleration voltages while the magnon EELS would be increased.

In conclusion, the methodology explored here is intended to help characterise and quantify the magnon spectra for thin films in inelastic scattering experiments focusing on EELS. However, further technological advancements in detectors and monochromators will be required to overcome the weak EELS signal due to magnons, to make it a standard tool in the characterisation of magnetic structures.

5.1 Future work

The methodological basis set by the work in its current state, provides many avenues for continuation in the near future. Extending the methodology for other probes, such as photons (i.e. Raman Spectroscopy) is an interesting prospect which will complement electron probes with high energy resolution. Exploration of different materials, and pairing the established methodologies for the study of EELS of phonons with the magnon counterpart can provide invaluable information for the distinction between the two. In addition, extending the effects by exploiting the interplay of magnon-phonon-plasmon interactions, under the second quantisation methodology can prove to be an interesting pathway.

In addition, having the machinery described for the EELS allows a smooth extension to simulate the imaging of these interactions in the STEM-EELS experiment, both for elastic and inelastic interactions. In this case, the orientational nature of the interaction with the magnetic moments can affect the image in a major way. The negative side of this approach is that the magnetic effects on the image are orders of magnitude less intense than the Coulombic ones, making them invisible in the standard imaging methodology. Hence, procuring creative ways to enhance this effect by aloof imaging or specific imaging conditions can be an interesting next step. Preliminary calculations show that, in the case of charge-based interaction, the image reflects the orientation of the local magnetic moments.

Appendix A

Spin chain with dipolar interaction

To show that the dipolar interaction is not sufficient to explain the stability of magnetic solids, let's study the thermodynamics of an infinite chain of magnetic moments. For two magnetic moments at a distance R from each other has a potential energy of,

$$V(R, cos\theta_1, cos\theta_2, cos\theta_{1,2}) = \frac{\mu_0}{4\pi R^3}[\boldsymbol{\mu}\cdot\boldsymbol{\mu} - 3(\hat{R}\cdot\boldsymbol{\mu}_1)(\hat{R}\cdot\boldsymbol{\mu}_2)] \tag{A.1}$$

where $\boldsymbol{\mu}_1$ and $\boldsymbol{\mu}_2$ are the magnetic moment vectors, and $\hat{R} = \mathbf{R}/R$ is a unit vector representing the distance vector between the two magnetic moments. We note that the interaction depends on both the distance between the two magnetic moments and their relative angle.

To progress further we will use some simplifications:

- We will assume that all magnetic moments are aligned, such that $cos\theta_{1,2} = 1$
- Since all magnetic moments are aligned we can define, without loss of generality, $\theta_1 = \theta_2 = \theta$.

Then (A.1), become,

$$V(R_{i,j}) = \frac{\mu_0}{4\pi R^3}[1 - 3cos^2(\theta)]\mu_i\mu_j \tag{A.2}$$

A few notes need to be taken here, notice that the potential has two characteristics: The interaction falls with $\frac{1}{\mathbf{R}^3}$, falling relatively fast. The interaction

increases with the angle, meaning that if all magnetic moments are aligned perpendicular to the chain, the energy is higher than if they are all aligned in the direction of the chain, (the top of one is aligned with the bottom of the next).

So the minima occur with all spins aligned either with $\theta = 0$ or $\theta = \pi$. If we label each site with $(m = 1, 2...)$, the position of each site is given by, $m * a_0$ with a_0 being the distance between sites. To model the infinite sites, we have a sum to infinite twice to account for the spins along the negative axis.

So the total energy is,

$$\begin{aligned} E &= \frac{N\mu_0}{8\pi}\left\{2\sum_{m=1}^{\infty}\left[1-3cos^2 0\right]\frac{\mu^2}{(ma_0)^3}\right\} \\ &= \frac{N\mu_0}{8\pi}\left\{2\sum_{m=1}^{\infty}\frac{2\mu^2}{(ma_0)^3}\right\} \\ &= N\frac{\mu^2\mu_0}{4\pi {a_0}^3}\left\{2\sum_{m=1}^{\infty}\frac{1}{m^3}\right\} \\ &= N\frac{\mu^2\mu_0}{4\pi {a_0}^3}\{2\zeta(3)\} \\ &= N\frac{\mu^2\mu_0}{4\pi {a_0}^3}2(1.20206) \end{aligned} \tag{A.3}$$

If we take this result and evaluate the energy per site, we get,

$$\frac{E}{N} = \frac{\mu^2\mu_0}{4\pi {a_0}^3}2(1.20206) \tag{A.4}$$

Substituting the values for the Bohr magneton $\mu = 9.27 * 10^{-24} JT^{-1}$ and $\mu_0 = 1.26 * 10^{-6} NA^{-2}$ and assuming a separation of $a_0 = 2 * 10^{-10} m$ we get that the energy per site is around:

$$\frac{E}{N} = -(2S)^2 \times 2.5 \times 10^{-5} eV \approx 0.3(2S)^2 k_b \tag{A.5}$$

So the energy per site is a few fractions of a Kelvin, meaning that at very small temperatures the dipolar interaction is completely overpowered by thermal fluctuations. Even with S, which will be of the order O(1), the temperatures that would destroy ferromagnetism would be of the order of 1 to 2K.

A similar argument can be made if the magnetic moments are placed at

$\theta = \pi/2$, i.e. transverse to the chain, one can show that it is stable but also for very low temperatures, being a local minimum.

For a 3D crystal, with cubic symmetry, for example, the interactions cancel out in every direction, an even worse situation.

Appendix B

Thermal expectation value of Bosonic operators

To evaluate the thermal expected value of the bosonic operators, we will evaluate $\langle \alpha_n^\dagger \alpha_{n'}^\dagger \rangle_T = \langle \alpha_n \alpha_{n'} \rangle_T = 0$ and $\langle \alpha_n^\dagger \alpha_{n'} \rangle_T = n_B(\omega_n)\delta_{nn'}$.

We have to evaluate the following equation,

$$\sum_{n_0} \langle n_0 | \, \alpha_n^\dagger \alpha_{n'} \, | n_0 \rangle \, \frac{e^{-\beta E_{n_0}}}{Z_0} \tag{B.1}$$

So the overall expectation value is taken over the n_0 states with the partition function Z_0. Inserting a complete basis n_1, we have,

$$\sum_{n_0} \sum_{n_1} \langle n_0 | \, \alpha_n^\dagger \, | n_1 \rangle \, \langle n_1 | \, \alpha_{n'} \, | n_0 \rangle \, \frac{e^{-\beta E_{n_1}}}{Z_0} \tag{B.2}$$

Notice that the orthogonality of the $|n_0\rangle$ and $|n_1\rangle$ impose constrains in the sum. Since the creation and annihilation operators will raise or lower the energy of the harmonic oscillation at a particular site n or n', from $\langle n_1 | \, \alpha_{n'} \, | n_0 \rangle$ we need that the state $|n_0\rangle$ to be one level higher than $|n_1\rangle$ at site n', and from $\langle n_0 | \, \alpha_n^\dagger \, | n_1 \rangle$ we need that state $|n_1\rangle$ to be one step lower than $|n_1\rangle$ at site n. This condition is easily fulfilled if $n = n'$ and, redefining the basis notation to only define the energy level, by setting $|n_1\rangle = |m-1\rangle$ and $|n_0\rangle = |m\rangle$,

$$\sum_{m} \langle m | \, \alpha_n^\dagger \, | m-1 \rangle \, \langle m-1 | \, \alpha_n \, | m \rangle \, \frac{e^{-\beta E_m}}{Z_0} = \tag{B.3}$$

$$= \sum_m \langle m| \sqrt{m} |m\rangle \langle m-1| \sqrt{m} |m-1\rangle \frac{e^{-\beta E_m}}{Z_0} \tag{B.4}$$

$$= \sum_m m \frac{e^{-\beta E_m}}{Z_0} \tag{B.5}$$

Note that the energy of the harmonic oscillator is given by,

$$E_m = \hbar\omega \left(m + \frac{1}{2} \right) \tag{B.6}$$

hence we have:

$$\frac{1}{Z_0} \sum_m m e^{-\beta\hbar\omega\left(m+\frac{1}{2}\right)} = \frac{1}{Z_0} e^{-\beta\frac{\hbar\omega}{2}} \sum_m m e^{-\beta\hbar\omega m} \tag{B.7}$$

given that the partition function is given by,

$$Z_0 = \sum_m e^{-\beta\hbar\omega m} e^{-\beta\frac{\hbar\omega}{2}} = e^{-\beta\frac{\hbar\omega}{2}} \sum_m e^{-\beta\hbar\omega m} = e^{-\beta\frac{\hbar\omega}{2}} \frac{1}{1-e^{-\beta\hbar\omega}} \tag{B.8}$$

at the same time, we have to note that,

$$\sum_m m e^{mx} = \frac{d}{dx} \sum_m e^{mx} = \frac{d}{dx} \frac{1}{1-e^{mx}} = \frac{e^x}{(1-e^x)^2} \tag{B.9}$$

using Eq. (8) and Eq. (9) by setting $x = -\beta\hbar\omega$ and substituting in Eq. (7), we get,

$$\frac{1}{Z_0} e^{-\beta\frac{\hbar\omega}{2}} \sum_m m e^{-\beta\hbar\omega m} = \frac{e^{-\beta\hbar\omega}}{(1-e^{-\beta\hbar\omega})} = \frac{1}{(e^{\beta\hbar\omega}-1)} = n_B \tag{B.10}$$

hence we have that $\langle \alpha_n^\dagger \alpha_{n'} \rangle_T = n_B(\omega_n)\delta_{nn'}$. The other terms, such as $\langle \alpha_n^\dagger \alpha_{n'}^\dagger \rangle_T = \langle \alpha_n \alpha_{n'} \rangle_T = 0$, are identically zero because the step given in Eq. (B.5) cannot be fulfilled in any way, making all terms in the sum zero due to the orthogonality of the basis.

Appendix C

Excited state of Heisemberg Hamiltonian

Taking the Heisenberg Hamiltonian for a homogeneous 1D chain given in the main text of the thesis, we have,

$$H = -\frac{1}{2}\sum_{k} J[\frac{1}{2}\left(S_k^+ S_{k+1}^- + S_k^- S_{k+1}^+\right) + S_k^z S_{k+1}^z + \frac{1}{2}\left(S_k^+ S_{k-1}^- + S_k^- S_{k-1}^+\right) + S_k^z S_{k-1}^z] \tag{C.1}$$

We wish to evaluate the expected value of the system's energy with this given Hamiltonian. Assuming the general basis composed of a linear combination of a single spin flip in every site, given by,

$$|\psi\rangle = \sum_i f_i \, |i\rangle \tag{C.2}$$

We want to verify for which values of the coefficients in the linear combination in Eq. (C.2), compose a excited state of the Hamiltonian.

Let's look at the possible terms that need to be evaluated. Note that the following definitions hold:

$$S^+ \, |S, S-1\rangle = \sqrt{2S} \, |S; S\rangle \tag{C.3}$$

$$\left[S_i^+, S_j^-\right] = -2\delta_{ij} S_j^z \tag{C.4}$$

$$|i\rangle = \frac{S_i^-}{\sqrt{2S}} |0\rangle \tag{C.5}$$

First, we evaluate the terms that involve raising and lowering operators,

$$\begin{aligned} S_k^+ S_{k+1}^- \sum_i f_i |i\rangle =& S_k^+ S_{k+1}^- \sum_i f_i \frac{S_i^-}{\sqrt{2S}} |0\rangle \\ =& \frac{1}{\sqrt{2S}} S_{k+1}^- \sum_i f_i \left[\delta_{k,i} 2S_i^z + S_i^- S_k^+\right] |0\rangle \\ =& 2S \frac{1}{\sqrt{2S}} f_k S_{k+1}^- |0\rangle \\ =& 2S f_k |k+1\rangle \end{aligned} \tag{C.6}$$

$$\begin{aligned} S_k^- S_{k+1}^+ \sum_i f_i |i\rangle =& \sqrt{2S} S_k^- f_{k+1} |0\rangle \\ =& \sqrt{2S} f_{k+1} S_k^- |0\rangle \\ =& 2S f_{k+1} |k\rangle \end{aligned} \tag{C.7}$$

Here, in Eq. (C.6) we used the commutation relation in Eq. (C.4), and the definition of the basis, in terms of the lowering operator as given in Eq. (C.5). In Eq. (C.7) we used the fact that operating in any case where the site flipped i doesn't match with $k+1$ in the raising operator will lead to an attempt to raise the magnetic moments z-projection higher than the maximum, leading to zero by definition. Using the same arguments we have,

$$S_k^+ S_{k-1}^- \sum_i f_i |i\rangle = 2S f_k |k-1\rangle \tag{C.8}$$

$$\begin{aligned} S_k^- S_{k-1}^+ \sum_i f_i |i\rangle =& \sqrt{2S} S_k^- f_{k-1} |0\rangle \\ =& \sqrt{2S} f_{k-1} S_k^- |0\rangle \\ =& 2S f_{k-1} |k\rangle \end{aligned} \tag{C.9}$$

To evaluate the terms that involve $S_k^z S_{k+1}^z$, let's first discuss the case for $k = 1$, and use the result to generalise the solution,

$$
\begin{aligned}
S_1^z S_2^z \sum_i f_i \left|i\right\rangle = S_1^z S_2^z \{ & f_1 \left|S, S-1\right\rangle_1 \left|S, S\right\rangle_2 \left|S, S\right\rangle_3 \ldots \left|S, S_N\right\rangle \\
& + f_2 \left|S, S\right\rangle_1 \left|S, S-1\right\rangle_2 \left|S, S\right\rangle_3 \ldots \left|S, S_N\right\rangle \\
& + f_3 \left|S, S\right\rangle_1 \left|S, S\right\rangle_2 \left|S, S-1\right\rangle_3 \ldots \left|S, S_N\right\rangle \\
& + \cdots \}
\end{aligned}
\tag{C.10}
$$

$$
\begin{aligned}
S_1^z S_2^z \sum_i f_i \left|i\right\rangle = \{ & S(S-1) f_1 \left|S, S-1\right\rangle_1 \left|S, S\right\rangle_2 \left|S, S\right\rangle_3 \ldots \left|S, S_N\right\rangle \\
& + (S-1) S f_2 \left|S, S\right\rangle_1 \left|S, S-1\right\rangle_2 \left|S, S\right\rangle_3 \ldots \left|S, S_N\right\rangle \\
& + S^2 \left|S, S\right\rangle_1 \left|S, S\right\rangle_2 \left|S, S-1\right\rangle_3 \ldots \left|S, S_N\right\rangle \\
& + \cdots \}
\end{aligned}
\tag{C.11}
$$

Notice that we have the eigenvalue $S(S-1)$ for the sites that match the sites k and $k+1$, while all the rest of the terms contribute with S^2. This can be represented in the following way,

$$
\begin{aligned}
S_k^z S_{k+1}^z \sum_i f_i \left|i\right\rangle = & f_k (S-1) S \left|k\right\rangle + f_{k+1} (S-1) S \left|k+1\right\rangle \\
& - S^2 f_k \left|k\right\rangle - S^2 f_{k+1} \left|k+1\right\rangle + \sum_i f_i S^2 \left|i\right\rangle \\
S_k^z S_{k-1}^z \sum_i f_i \left|i\right\rangle = & - f_k S \left|k\right\rangle - f_{k+1} S \left|k+1\right\rangle + \sum_i f_i S^2 \left|i\right\rangle
\end{aligned}
\tag{C.12}
$$

Collecting all these terms, and subistituting in $H\left|\psi\right\rangle = E\left|\psi\right\rangle$ using H as given in Eq. (C.1),

$$
\begin{aligned}
H \sum_i f_i \left|i\right\rangle = -\frac{1}{2} \sum_k J [& S f_{k+1} \left|k\right\rangle + S f_k \left|k+1\right\rangle \\
& - S f_k \left|k\right\rangle - S f_{k+1} \left|k+1\right\rangle + \sum_i f_i S^2 \left|i\right\rangle \\
& + S f_{k-1} \left|k\right\rangle + S f_k \left|k-1\right\rangle \\
& - S f_k \left|k\right\rangle - S f_{k-1} \left|k-1\right\rangle + \sum_i f_i S^2 \left|i\right\rangle] \\
= & E \sum_i f_i \left|i\right\rangle
\end{aligned}
\tag{C.13}
$$

multiplying Eq. (C.13) by the left with a particular state $\langle k|$ and noting that due to orthonormality,

$$\langle k|k\rangle = 1 \tag{C.14}$$

$$\langle k|i\rangle = \delta_{i,k} \tag{C.15}$$

$$\langle k|k+1\rangle = \langle k|k-1\rangle = 0 \tag{C.16}$$

Leading to,

$$-[f_{k+1} + f_{k-1} - 2f_k] = \frac{2E}{JS} f_k + 2NS f_k \tag{C.17}$$

The term on the left-hand side is a discrete second derivative of f_i assuming a unit distance between the sites which will be later defined as a, i.e. the coefficients of the linear combination in Eq. (C.2), giving us,

$$\frac{d^2 f_k}{dx_k^2} = -\left(\frac{2E}{JS} + 2NS\right) f_k \tag{C.18}$$

one possible solution for the differential equation in Eq. (C.18) is,

$$f_i(x_i) \propto e^{iqx_i} \tag{C.19}$$

inserting this back in Eq. (C.17) we have,

$$\begin{aligned}
-[e^{iqx_i}e^{iqa} + e^{iqx_i}e^{-iqa} - 2e^{iqx_i}] &= \left(\frac{2E}{JS} + 2NS\right) e^{iqx_i} \\
-[e^{iqa} + e^{-iqa} - 2] &= \left(\frac{2E}{JS} + 2NS\right) \\
-[2\cos(qa) - 2] &= \left(\frac{2E}{JS} + 2NS\right) \\
-JS[2\cos(qa) - 2] &= \left(2E + 2JNS^2\right) \\
E &= -JNS^2 - JS[\cos(qa) - 1] \\
E &= -JNS^2 + JS[1 - \cos(qa)]
\end{aligned} \tag{C.20}$$

With these steps, we verified that the exited state of this system is, account-

ing for normalisation, given by,

$$|q\rangle = \frac{1}{\sqrt{N}} \sum_i e^{i\boldsymbol{R}_i \cdot \boldsymbol{q}} |i\rangle \tag{C.21}$$

and the ground state energy is given by, $E_0 = -JNS^2$, and the dispersion of the excited state is given by,

$$E(q) = JS[1 - \cos(qa)] \tag{C.22}$$

Appendix D

Magnon dispersion calculation

In this section let's study the dispersion relation for the magnons in different materials. Formally we will be writing the Hamiltonian of the system using (3.20), and by diagonalising it for different $\mathbf{q}_{\parallel}$ we will be able to evaluate the magnon dispersion for the magnons that are supported by the system.

First, let's study a simple system, to exemplify the use of the method. In figure D.1, consider a ferromagnetic cubic lattice, with spins S aligned along **z** and coupled by nearest-neighbour exchange parameter $J > 0$.

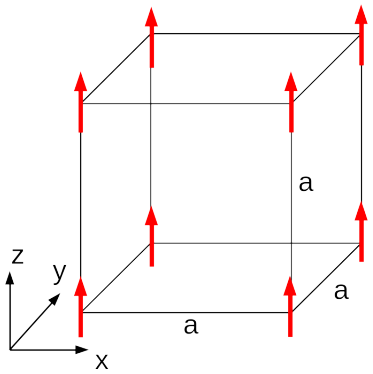

Figure D.1: The ground state of a ferromagnetic cubic lattice.

The terms from 3.20 that we need to address are $F_J(r,s)_{zz}$, $G_1(r,s)$ and $G_2(r,s)$, which for a single magnetic moment pointing in the z-direction, we have,

$$\begin{cases} F_J(1,1)_{zz} &= J, \\ G_1(1,1) &= 0, \\ G_2(1,1) &= 2J \end{cases} \tag{D.1}$$

similarly, for the magneto-crystalline anisotropy and Zeeman term, we define them to be parallel to the magnetic moments, leading to,

$$\begin{cases} A(0)_x &= 0, \\ A(0)_y &= 0, \\ A(0)_z &= 1 \end{cases} \tag{D.2}$$

also noting that for nearest-neighbour in the cubic structure, we have $z_u = 6$, leading to $\Gamma_{rs}^{(u)} = \Gamma_{11}^{(1)}$, given by,

$$\Gamma_{rs}^{(u)} = \frac{1}{z_u} \sum_{\mathbf{d}_u} e^{-i\mathbf{q}\cdot\mathbf{d}_u} \tag{D.3}$$

$$\Gamma_{11}^{(1)} = \frac{1}{6}[e^{-iaq_x} + e^{iaq_x} + e^{-iaq_y} + e^{iaq_y} + e^{-iaq_z} + e^{iaq_z}] \tag{D.4}$$

$$\Gamma_{11}^{(1)} = \frac{1}{3}[\cos(aq_x) + \cos(aq_y) + \cos(aq_z)] \tag{D.5}$$

This simplifies equation (3.20) to,

$$\begin{aligned} H_{ex} = \sum\nolimits_q 3JS \Big\{ \Big\{ 1 - \Gamma_{11}^{(1)}(q) \Big\} a_q^{(1)\dagger} a_q^{(1)} + \Big\{ 1 - \Gamma_{11}^{(1)}(q) \Big\} a_{-q}^{(1)} a_{-q}^{(1)\dagger} \Big\} \\ + KS \left\{ a_q^{(1)\dagger} a_q^{(1)} + a_{-q}^{(1)} a_{-q}^{(1)\dagger} \right\} \\ + 2\mu_B \mathbf{B} S \left\{ a_q^{(1)\dagger} a_q^{(1)} + a_{-q}^{(1)} a_{-q}^{(1)\dagger} \right\} \end{aligned} \tag{D.6}$$

It is then easy to show that L from (3.23) and $\mathcal{L}$ from (D.6),

$$L = S \begin{pmatrix} 3J \left[1 - \Gamma_{11}^{(1)}(q) \right] + K + 2\mu_B B & 0 \\ 0 & 3J \left[1 - \Gamma_{11}^{(1)}(q) \right] + K + 2\mu_B B \end{pmatrix} \tag{D.7}$$

$$\mathcal{L} = S \begin{pmatrix} 3J\left[1 - \Gamma_{11}^{(1)}(q)\right] + K + 2\mu_B B & 0 \\ 0 & -3J\left[1 - \Gamma_{11}^{(1)}(q)\right] - K - 2\mu_B B \end{pmatrix} \tag{D.8}$$

Since $\mathcal{L}$ has eigenvalues given by, $\varepsilon_n(q) = \omega_n(q)/2$, so the spin-wave frequency for a ferromagnet is,

$$\hbar\omega_n(q) = 6JS[1 - \Gamma_{11}^{(1)}(q)] + 2KS + 4\mu_B BS \tag{D.9}$$

with,

$$\Gamma_{11}^{(1)} = \frac{1}{3}[\cos(aq_x) + \cos(aq_y) + \cos(aq_z)] \tag{D.10}$$

This result allows us to gain some mental picture of the magnons. In the absence of easy-axis anisotropy, the magnetic moments can rotate freely, the only restriction is that they are all aligned relative to each other. Consequently, $\omega_n(0) = 0$ is a Goldstone mode, implying that for $q_\parallel = 0$, i.e. infinitely long wave-length magnon modes all magnetic moments fluctuate in phase from the z-axis, leading the system to change to an equivalent spin state, without any cost in energy.

Since the anisotropy K and magnetic field B changes the system such that the magnetic moments favour a particular orientation, they break the rotational invariance, leading to a gap in the energy for $q_\parallel = 0$ given by $\Delta = 2KS + 4\mu_B BS$.

Appendix E

Magnetic Form Factor

Having defined the position of the ion in a unit cell by,

$$\sum_i e^{iq\cdot\mathbf{r}_i}\mathbf{S}_i \tag{E.1}$$

here, q is the scattering vector, $\mathbf{r}_i$ the position vectors of the ions in the unit cell. We can further specify the position of the ν'th electron of the ion in the position $\mathbf{r}_i$, by a relative position vector $\mathbf{r}_\nu$ we can write,

$$\sum_{\mathbf{r}_i} e^{i\mathbf{q}\cdot\mathbf{r}_i}\mathbf{S}_i = \sum_{\mathbf{r}_i} e^{i\mathbf{q}\cdot\mathbf{r}_i} \sum_{\nu(\mathbf{r}_i)} e^{i\mathbf{q}\cdot\mathbf{r}_\nu}\mathbf{S}_\nu \tag{E.2}$$

The unpaired electron in each ion, couples together to give rise to the ground state with a total spin $\mathbf{S}_i$.

From [93], we have the definition of the form factor given by the Fourier transform of the normalised spin density associated with the ion at the i'th site, in the unit cell,

$$F(\mathbf{q}) = \int d\mathbf{r} e^{i\mathbf{q}\cdot\mathbf{r}} s_i(\mathbf{r}) \tag{E.3}$$

where, $s_i(\mathbf{r})$ it the normalised spin density, leading to $F(0) = 1$. When the mean radius of the wave function of the unpaired electrons, is much less than $|\mathbf{q}|^{-1}$, which is often the case, we can apply a dipolar approximation, and the magnetic form factor can be calculated from the radial distribution of the electrons. The integrals from which the form factors are obtained have the form,

$$\langle j_K(\mathbf{q})\rangle = \int_0^\infty d\mathbf{r} r^2 j_K(\mathbf{q})|f(\mathbf{r})|^2 \tag{E.4}$$

usually refered to as a radial integral, where $j_K(\mathbf{q})$ is a spherical Bessel function of order K. In the case of spin-only systems [93],

$$F(\mathbf{q}) = \langle j_0(\mathbf{q})\rangle \tag{E.5}$$

To simplify the calculation of the magnetic form factor we can use empirical analytical formulas which adequately approximate $\langle j_0(\mathbf{q})\rangle$, proposed by J. Brown [126], which for $\langle j_0(\mathbf{q})\rangle$ is given by,

$$\langle j_0(\mathbf{q})\rangle = Ae^{-as^2} + Be^{-bs^2} + Ce^{-cs^2} + D$$

with $s = q/4\pi$.

The values used for these paramenters for 3d transition elements and their ions are given in [126], here we have used the values for Fe^{3+},

ion	A	a	B	b	C	c	D
Fe^{3+}	0.3972	13.2442	0.6295	4.9034	-0.0314	0.3496	0.0044

Table E.1: Parameters for analitical formula of $\langle j_0(\mathbf{q})\rangle$ given by [126].

Appendix F

Some General Operator Theorems

In this appendix we will derive some useful therorems involving non-commuting operators A and B. We shall assume that the proposed functions of these operators may be expanded in a power seris such that,

$$F(B) = \sum_{n=0}^{\infty} c_n B^n \tag{F.1}$$

where the c_n are constant expansion coefficients. The coeficients are here called c-numbers which can be complex and are not operators.

Theorem 1. *If A and B are two noncommuting operators and ξ is a parameter, then, if n is an integer,*

$$e^{\xi A} B^n e^{-\xi A} = \left(e^{\xi A} B e^{-\xi A}\right)^n \tag{F.2}$$

and

$$e^{\xi A} F(B) e^{-\xi A} = F\left(e^{\xi A} B e^{-\xi A}\right) \tag{F.3}$$

When n=1, (2) is just an identity.

Proof. Note that,

$$e^{-\xi A} e^{\xi A} = I \tag{F.4}$$

So we can write,

$$e^{\xi A} BBB...Be^{-\xi A} = e^{\xi A} B e^{-\xi A} e^{\xi A} B e^{-\xi A} e^{\xi A} B e^{-\xi A} ... e^{\xi A} B e^{-\xi A} \tag{F.5}$$

$$\left(e^{\xi A} B e^{-\xi A}\right)\left(e^{\xi A} B e^{-\xi A}\right)\left(e^{\xi A} B e^{-\xi A}\right) ... \left(e^{\xi A} B e^{-\xi A}\right) = \left(e^{\xi A} B e^{-\xi A}\right)^n$$

proving Eq. (2). To prove Eq. (3) we use Eq. (2),

$$e^{\xi A}F(B)e^{-\xi A} = \sum_{n=0}^{\infty} c_n e^{\xi A}B^n e^{-\xi A} \tag{F.6}$$

and from Eq. (2) we arrive at:

$$e^{\xi A}F(B)e^{-\xi A} = \sum_{n=0}^{\infty} c_n \left(e^{\xi A}Be^{-\xi A}\right)^n = F\left(e^{\xi A}Be^{-\xi A}\right) \tag{F.7}$$

QED

Theorem 2. *If A and B are two noncommuting operators and if A^{-1} exists, we have,*

$$AB^nA^{-1} = \left(ABA^{-1}\right)^n \tag{F.8}$$

where n is an integer, and

$$AF(B)A^{-1} = F\left(ABA^{-1}\right)^n \tag{F.9}$$

Given that A^{-1} exists.

Proof. Taking that $AA^{-1} = I$, the same proof given in Theorem 1, applies. □

Theorem 3. *If A and B are two fixed noncommuting operators and ξ is a parameter, then,*

$$e^{\xi A}Be^{-\xi A} = B \ + \xi[A,B] \ + \frac{\xi^2}{2!}[A,[A,B]] + \frac{\xi^3}{3!}[A,[A,[A,B]]] + \ldots \tag{F.10}$$

Proof. Proof: We let,

$$f(\xi) = e^{\xi A}Be^{-\xi A} \tag{F.11}$$

$$f(0) = B \tag{F.12}$$

and expand $f(\xi)$ in a Maclaurin series in power of ξ. We then have

$$\begin{aligned} \frac{df}{d\xi} &= [A, f(\xi)] & \frac{df}{d\xi}\Big|_{\xi=0} &= [A, B] \\ \frac{d^2 f}{d\xi^2} &= \left[A, \frac{df}{d\xi}\right] = [A, [A, f(\xi)]] & \frac{d^2 f}{d\xi^2}\Big|_{\xi=0} &= [A, [A, B]] \end{aligned} \tag{F.13}$$

So (10) follows from further terms in the expansion. □

Theorem 4. *If l is an integer, then*

$$\left[a, a^{\dagger l}\right] = l a^{\dagger(l-1)} = \frac{\partial a^{\dagger l}}{\partial a^\dagger}$$

$$\left[a, a^{l}\right] = -l a^{(l-1)} = -\frac{\partial a^{\dagger l}}{\partial a^\dagger}$$

Proof. We start by proving the first equality. Let $P(l)$ be the statement $\left[a, a^{\dagger l}\right] = l a^{\dagger(l-1)}$, and taking the definitions for the commutation relation for a and $a^\dagger$,

$$\left[a, a^\dagger\right] = 1 \tag{F.14}$$

$$[a, a] = \left[a^\dagger a, a^\dagger\right] \; = \; 0 \tag{F.15}$$

we give a proof by induction on l.

$P(0)$ is true, given that it leads to, $[a, 0] = 0$, and also we have $P(1)$ to be true, given that (12) is true.

Induction step:

$P(k)$ is true $\left[a, a^{\dagger k}\right] = k a^{\dagger(k-1)}$.

It follows that we need to show that $P(k+1)$ also hold, we start,

$$\left[a, a^{\dagger k}\right] = k a^{\dagger(k-1)}$$

$$a a^{\dagger k} - a^{\dagger k} a = k a^{\dagger(k-1)}$$

Multiplying bothsides by $a^\dagger$,

$$\begin{aligned} aa^{\dagger k}a^\dagger - a^{\dagger k}aa^\dagger &= ka^{\dagger k} \\ aa^{\dagger(k+1)} - a^{\dagger k}\left(1 + a^\dagger a\right) &= ka^{\dagger k} \\ aa^{\dagger(k+1)} - a^{\dagger k} - a^{\dagger(k+1)}a &= ka^{\dagger k} \\ aa^{\dagger(k+1)} - a^{\dagger(k+1)}a &= ka^{\dagger k} + a^{\dagger k} \\ \left[a, a^{\dagger(k+1)}\right] &= (k+1)a^{\dagger(k+1)-1} \end{aligned}$$

That is, the statement $P(k+1)$ also holds. Since both the base case and the induction steps have been proven as true, by mathematical induction the statement $P(k)$ holds for every natural number k.

For the second equality, it is required of us to define more precisely what we mean by $\partial/\partial a$ and $\partial/\partial a^\dagger$ since a and $a^\dagger$ are operators. We can replace the operator a or $a^\dagger$ by $a + x$ or $a^\dagger + x$, where x is a c-number, and write,

$$\begin{aligned} \lim_{x\to 0}\frac{\partial}{\partial x}\left(a^\dagger + x\right)^k &= \lim_{x\to 0}\frac{\partial}{\partial x}k\left(a^\dagger + x\right)^{k-1} \\ &= ka^{\dagger(k-1)} = \frac{\partial a^{\dagger k}}{\partial a^\dagger} \end{aligned} \tag{F.16}$$

while $\dfrac{\partial a^k}{\partial a} = \lim_{x\to 0}\dfrac{\partial}{\partial x}(a+x)^k$. QED

Theorem 5. *We let x be a c-number and $f\left(a, a^\dagger\right)$ be a function that can be expanded in a power series in a and $a^\dagger$. Then,*

$$e^{xa}f\left(a, a^\dagger\right)e^{-xa} = f\left(a, a^\dagger + x\right) \tag{F.17}$$

$$e^{-xa}f\left(a, a^\dagger\right)e^{xa} = f\left(a + x, a^\dagger\right) \tag{F.18}$$

Proof. Noting that $e^{xa}e^{-xa} = 1$ and that f can be expanded in a power series, we have for the left-hand side of (15),

$$e^{xa}f\left(a, a^\dagger\right)e^{-xa} = f\left(e^{xa}ae^{-xa}, e^{xa}a^\dagger e^{-xa}\right) \tag{F.19}$$

and taking that the operators commute with themselves, and with any function of them,

$$e^{xa} f\left(a, a^{\dagger}\right) e^{-xa} = f\left(a, e^{xa} a^{\dagger} e^{-xa}\right) \tag{F.20}$$

By and Eq. (12) we can see that,

$$e^{xa} a^{\dagger} e^{-xa} = a^{\dagger} + x\left[a, a^{\dagger}\right] = a^{\dagger} + x \tag{F.21}$$

noting that all remaining commutators vanish. Then, subistituting Eq. (19) in Eq. (18), then Eq. (15) follows. A similar proof can be done for Eq. (16). □

Theorem 6. *We let $f\left(a, a^{\dagger}\right)$ be a fucntion of a and $a^{\dagger}$ that may be expanded in a power series in a and $a^{\dagger}$. Then,*

$$\left[a, f\left(a, a^{\dagger}\right)\right] = \frac{\partial f}{\partial a^{\dagger}} \tag{F.22}$$

$$\left[a^{\dagger}, f\left(a, a^{\dagger}\right)\right] = -\frac{\partial f}{\partial a} \tag{F.23}$$

Proof. Using the result from we consider,

$$F(x) = e^{xa} f\left(a, a^{\dagger}\right) e^{-xa} = f\left(a, a^{\dagger} + x\right) \tag{F.24}$$

Then, it follows that $F(0) = f\left(a, a^{\dagger}\right)$.

We can then write,

$$\frac{\partial F}{\partial x} = [a, F(x)] = \frac{\partial}{\partial x} f\left(a, a^{\dagger} + x\right) \tag{F.25}$$

By taking the limit as $x \to 0$ on both sides of Eq. (23), we have,

$$\lim_{x \to 0} \frac{\partial}{\partial x} f\left(a, a^{\dagger} + x\right) = \left[a, f\left(a, a^{\dagger}\right)\right] = \frac{\partial f}{\partial a^{\dagger}} \tag{F.26}$$

Since by (14) the left hand side is just the defintion of the partial derivative of $f\left(a, a^{\dagger}\right)$ with respect to $a^{\dagger}$. A similar proof follows for (21). Note that the order od the factors in important for this proof and must be strictly preserved.

□

Bibliography

[1] Data growth worldwide 2010-2025. https://www.statista.com/statistics/871513/worldwide-data-created/. Accessed: 2024-2-20.

[2] Total installed base of data storage capacity in global datasphere 2020-2025. https://www.statista.com/statistics/1185900/worldwide-datasphere-storage-capacity-installed-base/. Accessed: 2024-2-20.

[3] Vida Rozite, Emi Bertoli, and Brendan Reidenbach. Data centres and networks. https://www.iea.org/energy-system/buildings/data-centres-and-data-transmission-networks. Accessed: 2024-2-20.

[4] Jeffrey Dean and Sanjay Ghemawat. Mapreduce: Simplified data processing on large clusters. *Commun. ACM*, 51(1):107–113, jan 2008.

[5] Apache Software Foundation. Hadoop.

[6] Matei Zaharia, Reynold S. Xin, Patrick Wendell, Tathagata Das, Michael Armbrust, Ankur Dave, Xiangrui Meng, Josh Rosen, Shivaram Venkataraman, Michael J. Franklin, Ali Ghodsi, Joseph Gonzalez, Scott Shenker, and Ion Stoica. Apache spark: a unified engine for big data processing. *Commun. ACM*, 59(11):56–65, oct 2016.

[7] Why cloud solutions could help your business reduce its energy costs. https://www.ebcgroup.co.uk/news-insights/

why-cloud-solutions-could-help-your-business-reduce-its-energy-costs, June 2023. Accessed: 2024-2-20.

[8] B. L. Dokic. A review on energy efficient cmos digital logic. *Engineering, Technology and amp; Applied Science Research*, 3(6):552–561, December 2013.

[9] Abdulqader Mahmoud, Florin Ciubotaru, Frederic Vanderveken, Andrii V. Chumak, Said Hamdioui, Christoph Adelmann, and Sorin Cotofana. Introduction to spin wave computing. *Journal of Applied Physics*, 128(16):161101, 10 2020.

[10] Anjan Barman, Gianluca Gubbiotti, S Ladak, A O Adeyeye, M Krawczyk, J Gräfe, C Adelmann, S Cotofana, A Naeemi, V I Vasyuchka, B Hillebrands, S A Nikitov, H Yu, D Grundler, A V Sadovnikov, A A Grachev, S E Sheshukova, J-Y Duquesne, M Marangolo, G Csaba, W Porod, V E Demidov, S Urazhdin, S O Demokritov, E Albisetti, D Petti, R Bertacco, H Schultheiss, V V Kruglyak, V D Poimanov, S Sahoo, J Sinha, H Yang, M Münzenberg, T Moriyama, S Mizukami, P Landeros, R A Gallardo, G Carlotti, J-V Kim, R L Stamps, R E Camley, B Rana, Y Otani, W Yu, T Yu, G E W Bauer, C Back, G S Uhrig, O V Dobrovolskiy, B Budinska, H Qin, S van Dijken, A V Chumak, A Khitun, D E Nikonov, I A Young, B W Zingsem, and M Winklhofer. The 2021 magnonics roadmap. *Journal of Physics: Condensed Matter*, 33(41):413001, August 2021.

[11] Matthew J. Gilbert. Topological electronics. *Communications Physics*, 4(1), April 2021.

[12] Kevin Bullis. Hard-drive advance wins the nobel prize, Apr 2020.

[13] Atsufumi Hirohata, Keisuke Yamada, Yoshinobu Nakatani, Ioan-Lucian Prejbeanu, Bernard Diény, Philipp Pirro, and Burkard Hillebrands. Review on spintronics: Principles and device applications. *Journal of Magnetism and Magnetic Materials*, 509:166711, 2020.

[14] J.E. Lenz. A review of magnetic sensors. *Proceedings of the IEEE*, 78(6):973–989, 1990.

[15] S. Parkin, Xin Jiang, C. Kaiser, A. Panchula, K. Roche, and M. Samant. Magnetically engineered spintronic sensors and memory. *Proceedings of the IEEE*, 91(5):661–680, 2003.

[16] Pavel Ripka and Michal Janosek. Advances in magnetic field sensors. *IEEE Sensors Journal*, 10(6):1108–1116, 2010.

[17] W. J. Gallagher and S. S. P. Parkin. Development of the magnetic tunnel junction mram at ibm: From first junctions to a 16-mb mram demonstrator chip. *IBM Journal of Research and Development*, 50(1):5–23, 2006.

[18] Claude Chappert, Albert Fert, and Frédéric Nguyen Van Dau. The emergence of spin electronics in data storage. *Nature Materials*, 6(11):813–823, November 2007.

[19] Andrew D. Kent and Daniel C. Worledge. A new spin on magnetic memories. *Nature Nanotechnology*, 10(3):187–191, March 2015.

[20] Sabpreet Bhatti, Rachid Sbiaa, Atsufumi Hirohata, Hideo Ohno, Shunsuke Fukami, and S.N. Piramanayagam. Spintronics based random access memory: a review. *Materials Today*, 20(9):530–548, 2017.

[21] A V Chumak, A A Serga, and B Hillebrands. Magnonic crystals for data processing. *Journal of Physics D: Applied Physics*, 50(24):244001, May 2017.

[22] Wei Han, YoshiChika Otani, and Sadamichi Maekawa. Quantum materials for spin and charge conversion. *npj Quantum Materials*, 3(1), May 2018.

[23] Jorge Puebla, Junyeon Kim, Kouta Kondou, and Yoshichika Otani. Spintronic devices for energy-efficient data storage and energy harvesting. *Communications Materials*, 1(1), May 2020.

[24] Abdulqader Mahmoud, Florin Ciubotaru, Frederic Vanderveken, Andrii V. Chumak, Said Hamdioui, Christoph Adelmann, and Sorin Cotofana. Introduction to spin wave computing. *Journal of Applied Physics*, 128(16), October 2020.

[25] Felix Bloch. Zur theorie des austauschproblems und der remanenzerscheinung der ferromagnetika. pages 295–335, 1932.

[26] V. G. Bar'yakhtar and B. A. Ivanov. The Landau-Lifshitz equation: 80 years of history, advances, and prospects. *Low Temperature Physics*, 41(9):663–669, 09 2015.

[27] T. Holstein and H. Primakoff. Field dependence of the intrinsic domain magnetization of a ferromagnet. *Phys. Rev.*, 58:1098–1113, Dec 1940.

[28] Freeman J. Dyson. General theory of spin-wave interactions. *Phys. Rev.*, 102:1217–1230, Jun 1956.

[29] U. Köbler and A. Hoser. The crossover from atomistic to continuous dynamic symmetry at the magnetic phase transition. *Solid State Communications*, 142(10):600–604, 2007.

[30] Y. Z. Wang, T. Y. Zhang, J. Dong, P. Chen, G. Q. Yu, C. H. Wan, and X. F. Han. Voltage-controlled magnon transistor via tuning interfacial exchange coupling. *Phys. Rev. Lett.*, 132:076701, Feb 2024.

[31] Andrii V. Chumak, Alexander A. Serga, and Burkard Hillebrands. Magnon transistor for all-magnon data processing. *Nature Communications*, 5(1), August 2014.

[32] Alexander Khitun and Kang L. Wang. Non-volatile magnonic logic circuits engineering. *Journal of Applied Physics*, 110(3), August 2011.

[33] M. P. Kostylev, A. A. Serga, T. Schneider, B. Leven, and B. Hillebrands. Spin-wave logical gates. *Applied Physics Letters*, 87(15), October 2005.

[34] K Bennemann. Magnetic nanostructures. *Journal of Physics: Condensed Matter*, 22(24):243201, jun 2010.

[35] S.D. Bader. Magnetism in low dimensionality. *Surface Science*, 500(1):172–188, 2002.

[36] Khalil Zakeri. Terahertz magnonics: Feasibility of using terahertz magnons for information processing. *Physica C: Superconductivity and its Applications*, 549:164–170, 2018.

[37] S.O. Demokritov, B. Hillebrands, and A.N. Slavin. Brillouin light scattering studies of confined spin waves: linear and nonlinear confinement. *Physics Reports*, 348(6):441–489, 2001.

[38] Klaus Baberschke. Why are spin wave excitations all important in nanoscale magnetism? *physica status solidi (b)*, 245(1):174–181, 2008.

[39] B. Lenk, H. Ulrichs, F. Garbs, and M. Münzenberg. The building blocks of magnonics. *Physics Reports*, 507(4):107–136, 2011.

[40] Maciej Krawczyk and D Grundler. Review and prospects of magnonic crystals and devices with reprogrammable band structure. *Journal of physics: Condensed matter*, 26(12):123202, 2014.

[41] Lutong Sheng, Jilei Chen, Hanchen Wang, and Haiming Yu. Magnonics based on thin-film iron garnets. *Journal of the Physical Society of Japan*, 90(8):081005, 2021.

[42] Daniela Petti, Silvia Tacchi, and Edoardo Albisetti. Review on magnonics with engineered spin textures. *Journal of Physics D: Applied Physics*, 55(29):293003, 2022.

[43] XS Wang and XR Wang. Topological magnonics. *Journal of Applied Physics*, 129(15), 2021.

[44] Daniele Fausti, Agung A. Nugroho, Paul H.M. van Loosdrecht, Sergei A. Klimin, Marina N. Popova, and Leonard N. Bezmaternykh. Raman scattering from phonons and magnons in $\mathrm{rfe_3(bo_3)_4}$. *Phys. Rev. B*, 74:024403, Jul 2006.

[45] Arnab Bera, Satyabrata Bera, Sk Kalimuddin, Sirshendu Gayen, Mohan Kundu, Biswajit Das, and Mintu Mondal. Review of recent progress on thz spectroscopy of quantum materials: superconductors, magnetic and topological materials. *The European Physical Journal Special Topics*, 230(23):4113–4139, July 2021.

[46] Beom Hyun Kim and Jeroen van den Brink. Resonant inelastic x-ray scattering on single magnons at oxygen k edges. *Phys. Rev. B*, 92:081105, Aug 2015.

[47] Andrew J. Princep, Russell A. Ewings, Simon Ward, Sandor Tóth, Carsten Dubs, Dharmalingam Prabhakaran, and Andrew T. Boothroyd. The full magnon spectrum of yttrium iron garnet. *npj Quantum Materials*, 2(1), November 2017.

[48] Akio Kotani and Shik Shin. Resonant inelastic x-ray scattering spectra for electrons in solids. *Rev. Mod. Phys.*, 73:203–246, Feb 2001.

[49] L. Braicovich, J. van den Brink, V. Bisogni, M. Moretti Sala, L. J. P. Ament, N. B. Brookes, G. M. De Luca, M. Salluzzo, T. Schmitt, V. N. Strocov, and G. Ghiringhelli. Magnetic excitations and phase separation in the underdoped $\mathrm{la}_{2-x}\mathrm{sr}_x\mathrm{cuo}_4$ superconductor measured by resonant inelastic x-ray scattering. *Phys. Rev. Lett.*, 104:077002, Feb 2010.

[50] Xingxu Yan, Chaitanya A. Gadre, Toshihiro Aoki, and Xiaoqing Pan. Probing molecular vibrations by monochromated electron microscopy. *Trends in Chemistry*, 4(1):76–90, 2022.

[51] Site by Granite. Spatial resolution in raman spectroscopy, Feb 2023.

[52] Rayleigh. Xv.on the theory of optical images, with special reference to the microscope. *The London, Edinburgh, and Dublin Philosophical Magazine and Journal of Science*, 42(255):167–195, August 1896.

[53] Rayleigh. Xxxi. investigations in optics, with special reference to the spectroscope. *The London, Edinburgh, and Dublin Philosophical Magazine and Journal of Science*, 8(49):261–274, October 1879.

[54] C. M. Sparrow. On spectroscopic resolving power. *The Astrophysical Journal*, 44:76, September 1916.

[55] E. Abbe. Beiträge zur theorie des mikroskops und der mikroskopischen wahrnehmung. *Archiv für Mikroskopische Anatomie*, 9(1):413–468, December 1873.

[56] Bertram N. Brockhouse. Slow neutron spectroscopy and the grand atlas of the physical world. *Reviews of Modern Physics*, 67:735–751, 1995.

[57] Alfred Q. R. Baron. Phonons in crystals using inelastic x-ray scattering. 2009.

[58] M. Krisch and F. Sette. Inelastic x-ray scattering with very high resolution at the esrf. *Crystallography Reports*, 62(1):1–12, January 2017.

[59] R. J. Nicholls, F. S. Hage, D. G. McCulloch, Q. M. Ramasse, K. Refson, and J. R. Yates. Theory of momentum-resolved phonon spectroscopy in the electron microscope. *Phys. Rev. B*, 99:094105, Mar 2019.

[60] F. S. Hage, D. M. Kepaptsoglou, Q. M. Ramasse, and L. J. Allen. Phonon spectroscopy at atomic resolution. *Phys. Rev. Lett.*, 122:016103, Jan 2019.

[61] F. S. Hage, G. Radtke, D. M. Kepaptsoglou, M. Lazzeri, and Q. M. Ramasse. Single-atom vibrational spectroscopy in the scanning transmission electron microscope. *Science*, 367(6482):1124–1127, 2020.

[62] Eric R Hoglund, De-Liang Bao, Andrew O'Hara, Sara Makarem, Zachary T Piontkowski, Joseph R Matson, Ajay K Yadav, Ryan C Haislmaier, Roman Engel-Herbert, Jon F Ihlefeld, Jayakanth Ravichandran, Ramamoorthy Ramesh, Joshua D Caldwell, Thomas E Beechem, John A Tomko, Jordan A Hachtel, Sokrates T Pantelides, Patrick E Hopkins, and James M Howe. Emergent interface vibrational structure of oxide superlattices. *Nature*, 601(7894):556–561, 2022.

[63] J. C. Loudon. Antiferromagnetism in nio observed by transmission electron diffraction. *Phys. Rev. Lett.*, 109:267204, Dec 2012.

[64] Keenan Lyon, Anders Bergman, Paul Zeiger, Demie Kepaptsoglou, Quentin M. Ramasse, Juan Carlos Idrobo, and Ján Rusz. Theory of magnon diffuse scattering in scanning transmission electron microscopy. *Phys. Rev. B*, 104:214418, Dec 2021.

[65] Benjamin Plotkin-Swing, George J. Corbin, Sacha De Carlo, Niklas Dellby, Christoph Hoermann, Matthew V. Hoffman, Tracy C. Lovejoy, Chris E. Meyer, Andreas Mittelberger, Radosav Pantelic, Luca Piazza, and Ondrej L. Krivanek. Hybrid pixel direct detector for electron energy loss spectroscopy. *Ultramicroscopy*, 217:113067, 2020.

[66] O.L. Krivanek, N. Dellby, J.A. Hachtel, J.-C. Idrobo, M.T. Hotz, B. Plotkin-Swing, N.J. Bacon, A.L. Bleloch, G.J. Corbin, M.V. Hoffman, C.E. Meyer, and T.C. Lovejoy. Progress in ultrahigh energy resolution eels. *Ultramicroscopy*, 203:60–67, 2019. 75th Birthday of Christian Colliex, 85th Birthday of Archie Howie, and 75th Birthday of Hannes Lichte / PICO 2019 - Fifth Conference on Frontiers of Aberration Corrected Electron Microscopy.

[67] Flaviano Jose Dos Santos. *First principles study of collective spin excitations in noncollinear magnets*. RWTH Aachen University, 2020.

[68] B.G. Mendis. Quantum theory of magnon excitation by high energy electron beams. *Ultramicroscopy*, 239:113548, 2022.

[69] Corina Etz, Lars Bergqvist, Anders Bergman, Andrea Taroni, and Olle Eriksson. Atomistic spin dynamics and surface magnons. *Journal of Physics: Condensed Matter*, 27(24):243202, June 2015.

[70] Michael G. Cottam and David R. Tilley. *Introduction to Surface and Superlattice Excitations*. CRC Press, May 2019.

[71] Khalil Zakeri. Probing of the interfacial heisenberg and dzyaloshinskii–moriya exchange interaction by magnon spectroscopy. *Journal of Physics: Condensed Matter*, 29(1):013001, November 2016.

[72] Seamus Beairsto, Maximilien Cazayous, Randy S. Fishman, and Rogério de Sousa. Confined magnons. *Phys. Rev. B*, 104:134415, Oct 2021.

[73] N. N. Bogoljubov. On a new method in the theory of superconductivity. *Il Nuovo Cimento*, 7(6):794–805, March 1958.

[74] Daniel C Mattis. *The Theory of Magnetism Made Simple*. WORLD SCIENTIFIC, 2006.

[75] N. Bohr. I. on the constitution of atoms and molecules. *The London, Edinburgh, and Dublin Philosophical Magazine and Journal of Science*, 26(151):1–25, July 1913.

[76] G E Uhlenbeck and S Goudsmit. Spinning electrons and the structure of spectra. *Nature*, 117(2938):264–265, February 1926.

[77] P A M Dirac. The quantum theory of the electron. *Proc. R. Soc. Lond. A Math. Phys. Sci.*, 117(778):610–624, February 1928.

[78] Wolfgang Nolting and Anupuru Ramakanth. *Quantum Theory of Magnetism*. Springer Berlin Heidelberg, 2009.

[79] Stephen Blundell and David Thouless. Magnetism in condensed matter. *American Journal of Physics*, 71(1):94–95, December 2002.

[80] B. Lüthi. Crystal field effects in rare earth systems. *Journal of Magnetism and Magnetic Materials*, 15–18:1–8, January 1980.

[81] I. Dzyaloshinsky. A thermodynamic theory of "weak" ferromagnetism of antiferromagnetics. *Journal of Physics and Chemistry of Solids*, 4(4):241–255, 1958.

[82] Tôru Moriya. Anisotropic superexchange interaction and weak ferromagnetism. *Phys. Rev.*, 120:91–98, Oct 1960.

[83] D.D. Stancil and A. Prabhakar. *Spin Waves: Theory and Applications*. Springer US, 2009.

[84] A Brataas, G Bauer, and P Kelly. Non-collinear magnetoelectronics. *Physics Reports*, 427(4):157–255, April 2006.

[85] Hung T. Diep. Quantum spin-wave theory for non-collinear spin structures, a review. *Symmetry*, 14(8):1716, August 2022.

[86] Flaviano José dos Santos, Manuel dos Santos Dias, and Samir Lounis. Modeling spin waves in noncollinear antiferromagnets: Spin-flop states, spin spirals, skyrmions, and antiskyrmions. *Phys. Rev. B*, 102:104436, Sep 2020.

[87] H. Thoma, V. Hutanu, H. Deng, V.E. Dmitrienko, P.J. Brown, A. Gukasov, G. Roth, and M. Angst. Revealing the absolute direction of the dzyaloshinskii-moriya interaction in prototypical weak ferromagnets by polarized neutrons. *Physical Review X*, 11(1), March 2021.

[88] Elliott Lieb and Daniel Mattis. Ordering energy levels of interacting spin systems. *Journal of Mathematical Physics*, 3(4):749–751, July 1962.

[89] Lasha Tkeshelashvili. Boson representation of spin operators. 2016.

[90] W.H. Louisell. *Radiation and Noise in Quantum Electronics*. McGraw-Hill physical and quantum electronics series. McGraw-Hill, 1964.

[91] Léon Van Hove. Correlations in space and time and born approximation scattering in systems of interacting particles. *Phys. Rev.*, 95:249–262, Jul 1954.

[92] Brent Fultz. Inelastic scattering. `http://www.its.caltech.edu/~matsci/btfgrp/Inelastic_Neutron_Book.pdf`. Accessed: 2024-2-20.

[93] S.W. Lovesey. *Theory of Neutron Scattering from Condensed Matter*. Number v. 2 in International series of monographs on physics. Clarendon Press, 1986.

[94] G.L. Squires. *Introduction to the Theory of Thermal Neutron Scattering*. Dover books on physics. Dover Publications, 1996.

[95] K. Sturm. Dynamic structure factor: An introduction. *Zeitschrift für Naturforschung A*, 48(1-2):233–242, 1993.

[96] B.G. Mendis. *Electron Beam-Specimen Interactions and Simulation Methods in Microscopy*. RMS - Royal Microscopical Society. Wiley, 2018.

[97] J Kubler, K H Hock, J Sticht, and A R Williams. Density functional theory of non-collinear magnetism. *Journal of Physics F: Metal Physics*, 18(3):469–483, March 1988.

[98] Randy S Fishman, Jaime A Fernandez-Baca, and Toomas Rõõm. *Spin-Wave Theory and its Applications to Neutron Scattering and THz Spectroscopy*. 2053-2571. Morgan and Claypool Publishers, 2018.

[99] Changyol Lee, David Vanderbilt, Kari Laasonen, R. Car, and M. Parrinello. Ab initio studies on the structural and dynamical properties of ice. *Phys. Rev. B*, 47:4863–4872, Mar 1993.

[100] S. V. Meshkov. Low-frequency dynamics of lennard-jones glasses. *Phys. Rev. B*, 55:12113–12120, May 1997.

[101] S. V. Halilov, H. Eschrig, A. Y. Perlov, and P. M. Oppeneer. Adiabatic spin dynamics from spin-density-functional theory: Application to fe, co, and ni. *Phys. Rev. B*, 58:293–302, Jul 1998.

[102] M. Pajda, J. Kudrnovský, I. Turek, V. Drchal, and P. Bruno. Ab initio calculations of exchange interactions, spin-wave stiffness constants, and curie temperatures of fe, co, and ni. *Phys. Rev. B*, 64:174402, Oct 2001.

[103] Corina Etz, Lars Bergqvist, Anders Bergman, Andrea Taroni, and Olle Eriksson. Atomistic spin dynamics and surface magnons. *Journal of Physics: Condensed Matter*, 27(24):243202, jun 2015.

[104] Frederik L Durhuus, Thorbjørn Skovhus, and Thomas Olsen. Plane wave implementation of the magnetic force theorem for magnetic exchange constants: application to bulk fe, co and ni. *Journal of Physics: Condensed Matter*, 35(10):105802, January 2023.

[105] Charles Kittel. *Introduction to Solid State Physics*. Wiley, 8 edition, 2004.

[106] Mohsen Hafez-Torbati, Frithjof B. Anders, and Götz S. Uhrig. Simplified approach to the magnetic blue shift of mott gaps. *Phys. Rev. B*, 106:205117, Nov 2022.

[107] M. T. Hutchings and E. J. Samuelsen. Measurement of spin-wave dispersion in NiO by inelastic neutron scattering and its relation to magnetic properties. *Physical Review B*, 6(9):3447–3461, November 1972.

[108] N Rinaldi-Montes, P Gorria, D Martínez-Blanco, A B Fuertes, L Fernández Barquín, J Rodríguez Fernández, I de Pedro, M L Fdez-Gubieda, J Alonso, L Olivi, G Aquilanti, I Puente-Orench, and J A Blanco. On the exchange bias effect in nio nanoparticles with a core(antiferromagnetic)/shell (spin glass) morphology. *Journal of Physics: Conference Series*, 663:012001, November 2015.

[109] A A Serga, A V Chumak, and B Hillebrands. YIG magnonics. *Journal of Physics D: Applied Physics*, 43(26):264002, June 2010.

[110] Vladimir Cherepanov, Igor Kolokolov, and Victor L'vov. The saga of yig: Spectra, thermodynamics, interaction and relaxation of magnons in a complex magnet. *Physics Reports*, 229(3):81–144, 1993.

[111] H.L. Glass. Ferrite films for microwave and millimeter-wave devices. *Proceedings of the IEEE*, 76(2):151–158, 1988.

[112] S. Geller and M. A. Gilleo. Structure and ferrimagnetism of yttrium and rare-earth–iron garnets. *Acta Crystallographica*, 10(3):239, Mar 1957.

[113] S Klingler, A V Chumak, T Mewes, B Khodadadi, C Mewes, C Dubs, O Surzhenko, B Hillebrands, and A Conca. Measurements of the exchange stiffness of YIG films using broadband ferromagnetic resonance techniques. *Journal of Physics D: Applied Physics*, 48(1):015001, December 2014.

[114] P. Pirro, T. Brächer, A. V. Chumak, B. Lägel, C. Dubs, O. Surzhenko, P. Görnert, B. Leven, and B. Hillebrands. Spin-wave excitation and propagation in microstructured waveguides of yttrium iron garnet/pt bilayers. *Applied Physics Letters*, 104(1), January 2014.

[115] C. Hahn, V. V. Naletov, G. de Loubens, O. Klein, O. d'Allivy Kelly, A. Anane, R. Bernard, E. Jacquet, P. Bortolotti, V. Cros, J. L. Prieto, and M. Muñoz. Measurement of the intrinsic damping constant in individual nanodisks of y3fe5o12 and y3fe5o12|pt. *Applied Physics Letters*, 104(15), April 2014.

[116] Carsten Dubs, Oleksii Surzhenko, Ralf Linke, Andreas Danilewsky, Uwe Brückner, and Jan Dellith. Sub-micrometer yttrium iron garnet LPE films with low ferromagnetic resonance losses. *Journal of Physics D: Applied Physics*, 50(20):204005, April 2017.

[117] Haiming Yu, O. d'Allivy Kelly, V. Cros, R. Bernard, P. Bortolotti, A. Anane, F. Brandl, R. Huber, I. Stasinopoulos, and D. Grundler. Magnetic thin-film insulator with ultra-low spin wave damping for coherent nanomagnonics. *Scientific Reports*, 4(1), October 2014.

[118] Houchen Chang, Peng Li, Wei Zhang, Tao Liu, Axel Hoffmann, Longjiang Deng, and Mingzhong Wu. Nanometer-thick yttrium iron garnet films with extremely low damping. *IEEE Magnetics Letters*, 5:1–4, 2014.

[119] Kyusup Lee, Dong-Kyu Lee, Dongsheng Yang, Rahul Mishra, Dong-Jun Kim, Sheng Liu, Qihua Xiong, Se Kwon Kim, Kyung-Jin Lee, and Hyunsoo Yang. Superluminal-like magnon propagation in antiferromagnetic NiO at nanoscale distances. *Nature Nanotechnology*, 16(12):1337–1341, October 2021.

[120] Jannes van Poppelen. *Superluminous magnons in Nickel Oxide*. PhD thesis, 2023.

[121] Ankit Rohatgi. Webplotdigitizer: Version 4.6, 2022.

[122] Stephen W. Lovesey. *Theory of Neutron Scattering from Condensed Matter Volume II: Polarization Effects and Magnetic Scattering*. Clarendon Press, 1984.

[123] B.G. Mendis. An inelastic multislice simulation method incorporating plasmon energy losses. *Ultramicroscopy*, 206:112816, 2019.

[124] S Toth and B Lake. Linear spin wave theory for single-q incommensurate magnetic structures. *Journal of Physics: Condensed Matter*, 27(16):166002, March 2015.

[125] Johan Hellsvik, Danny Thonig, Klas Modin, Diana Iuşan, Anders Bergman, Olle Eriksson, Lars Bergqvist, and Anna Delin. General method for atomistic spin-lattice dynamics with first-principles accuracy. *Phys. Rev. B*, 99:104302, Mar 2019.

[126] P.J. Brown. Magnetic form factors. `https://www.ill.eu/sites/ccsl/ffacts/`. Accessed: 2024-2-20.